Optically detected magnetic resonance of organic crystals

Mohamad Hazem Hajjar

Master's Thesis

Institute for Applied Physics
Faculty for Mathematics and Natural sciences
Rheinische Friedrich-Wilhelms-Universität Bonn

September 2025

I hereby declare that I have written this thesis independently and have not used any sources or aids other than those specified, and that all citations have been appropriately indicated.

Bonn, 30.09.2025
Date

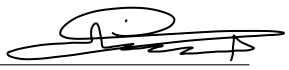
Signature

1. Supervisor: Prof. Dr. Daqing Wang

2. Supervisor: Prof. Dr. Stefan Linden

Acknowledgements

I would like to extend my heartfelt thanks to all those who have supported me throughout this thesis and the research journey.

First, I would like to thank Prof. Daqing Wang for being incredibly nice, helpful, and insightful. I am truly excited for the next 3-4 years of working together and growing under your guidance.

A special thanks to Prof. Stefan Linden for your invaluable assistance with antenna fabrication and for allowing us to use your evaporation machine, which was crucial for this project.

I also want to thank my fiancée Veronica for your unwavering support and for being so understanding about my late hours. Your patience means the world to me.

To my family, thank you for your emotional and sometimes financial support throughout my entire life. Your love and encouragement have shaped who I am today.

I would like to express my deepest gratitude to Babak, my lab partner, for being an amazing coder and debugger. Your insightful discussions have been instrumental, and I apologize for my occasional messiness at the optical table.

I also want to thank Max and Bo, my lab neighbors, for being the best senior lab mates I could ask for. Your advice, ideas, and friendship have been invaluable throughout this process.

To Ricardo, Danny, Nick, and Fang, thank you for your helpful discussions and for being part of this collaborative journey.

Lastly, I want to thank Yumi, Lucas, Delia, and Katherin for being such fun and supportive teammates. Our shared moments and many tea spills made this experience even more enjoyable.

Contents

1 Introduction

The development of quantum technology has inspired physicists to explore its applications in everyday life. In recent years, the field has seen remarkable advancements, including quantum computing [1], quantum sensing [2], quantum simulation [3], and quantum materials and devices [4]. These breakthroughs have served as the spark that ignited a growing passion to push the boundaries of quantum technology even further. There are various platforms for quantum technology, ranging from atoms [5] and ions [6] to superconducting materials [7] and molecules [8]. In this work, molecules will be in the spotlight.

Molecules are increasingly recognized for their potential in quantum technology applications due to their unique electronic, optical, and spin properties. Unlike bulk materials, molecules offer distinct advantages such as the ability to be manipulated at the molecular level, allowing for precise control of their energy levels and interactions. This level of customization allows the creation of highly coherent quantum states, essential for applications like quantum computing, sensing, and communication. Additionally, molecular systems, such as organic molecules or defects in solids, can operate at room temperature, making them more practical for real-world applications. The flexibility and scalability of molecules make them an attractive candidate for the next generation of quantum devices [9].

Optically detected magnetic resonance (ODMR) experiments with molecules have evolved significantly since their inception in the 1960s by Kwiram [10] and Schmidt et al. [11]. Initially, ODMR was primarily applied to solid-state systems like free radicals and defects in crystals, where the interaction between light and spin states was leveraged to probe electronic properties. Over time, the technique extended to molecular systems, particularly organic molecules and molecular dopants, and even to single molecules [12], due to their favorable spin properties and relatively simple energy-level structures. Early studies focused on fundamental understanding of spin–spin interactions and relaxation processes [13], while more recent advancements have demonstrated the potential of molecular ODMR for quantum sensing, communication, and even quantum computing [14], [15]. These developments have been propelled by advances in molecular design, as well as better sensitivity and precision in modern spectroscopic equipment, making molecular ODMR an increasingly important tool in the field of quantum technologies [9].

This work will serve as a base for further research. In the first section, the theory behind guest-host molecular systems, molecules like pentacene and perylene, triplet state and spin dynamics, and continuous wave (CW) ODMR are explained. Then, the preparations required to make the experiment succeed are discussed. Afterward, the experimental setup is introduced. After that, the results of measurements on perylene doped anthracene (PR:AC), pentacene doped p-terphenyl (PC:PTP) and deuterated pentacene doped deuterated p-terphenyl (dPC:dPTP) crystals are discussed. Lastly, the conclusion and outlook are presented.

2 Theory

This section serves as a brief introduction to the theory behind the organic guest-host systems and ODMR. First, the advantages of molecular host-guest systems will be introduced. Then, the photophysics of PAHs, namely pentacene and perylene, will be discussed. After that, the triplet state Hamiltonian and spin dynamics will be presented, only for pentacene, because there are no elaborate studies on perylene at room temperature. Lastly, continuous wave optically detected magnetic resonance will be described, again only for pentacene.

2.1 Molecular host-guest systems

Molecular host–guest systems provide an effective approach for stabilizing and adjusting the photophysical characteristics of organic molecules. In these systems, the guest molecule is placed within a crystalline or amorphous host matrix, forming a host-guest system through van der Waals interactions. The Van der Waals interaction allows the electronic excitations of the guest to remain largely localized within its own molecular orbitals, with only weak perturbation from the host. From a theoretical standpoint, the host–guest wavefunction can be broken down using the Born–Oppenheimer approximation into its electronic, vibrational, and nuclear components. Since host crystals have a large band gap, the guest molecule's lowest electronic excitations stay confined to the guest, experiencing only slight disturbances from the host. Therefore, the overall electronic wavefunction can be approximated as a product of contributions from both the host and the guest:

$$\Phi_{\text{el}} \approx \Phi_{\text{el,guest}}(r_g, s_g; R, I) \cdot \Phi_{\text{el,host}}(r_h, s_h; R, I), \tag{1}$$

where r and s stand for the spatial and spin coordinates of the electrons, (R, I) denote nuclear positions and spins, and the subscript g describes the guest's parameters and h the host's parameters. The vibrational structure of the host–guest system can also be divided into two elements, the guest's internal vibrations (vibrons) and the host's collective lattice vibrations (phonons). While high-frequency vibrons are largely unaffected by the host, low-frequency vibrations can interact strongly with the lattice and blend with the host phonons. This interaction appears as broadened sidebands in the optical spectrum [16]. Notably, vibrational relaxation happens rapidly, so after excitation, the guest molecule quickly returns to the lowest vibrational levels of its electronic states, in line with Kasha's rule [9].

A major result of this energy separation is the zero-phonon line (ZPL), which reflects the purely electronic $S_0 \leftrightarrow S_1$ transition between vibrational ground states. All other optical transitions manifest as sidebands, collectively called the phonon wing. With very low temperatures, high-quality crystalline hosts and low guest concentration, the ZPL linewidth can get close to the natural lifetime limit, making these systems ideal for use as highly coherent quantum emitters. At higher temperatures, stronger phonon interactions cause dephasing, which broadens the ZPL and reduces coherence [14]. In addition to optical traits, guest molecules exhibit spin structures within their lowest triplet states. Zero-field splitting removes the degeneracy of the triplet sublevels, and hyperfine interactions with nuclear spins from both the guest and surrounding host further shape the spin Hamiltonian. These effects allow for microwave-accessible transitions that can be initialized and read out using light [15]. This principle is key to techniques like optically detected magnetic resonance (ODMR), paving the way for using these systems as molecular spin qubits [9].

A key strength of molecular host–guest systems is their ability to combine electronic, vibrational, and spin features within a single molecule. This combination allows one molecule to function simultaneously as an optical interface, a vibrational unit, and a spin qubit. Meanwhile, the host environment determines how strongly the molecule interacts with its surroundings, which ultimately influences its coherence

properties [9]. For precise applications, hosts like p-terphenyl and anthracene are often selected because they reduce non-radiative decay and help sustain long-lived triplet states [13].

2.2 Photophysics of PAHs

Polycyclic aromatic hydrocarbons (PAHs) are a class of organic molecules composed of fused aromatic rings, known for their exceptional photophysical properties. These molecules exhibit strong absorption in the ultraviolet-visible (UV-Vis) range and often show efficient fluorescence, making them central to research in fields such as molecular electronics, organic photovoltaics, and astrophysical spectroscopy [17]. The photophysics of PAHs is governed by their conjugated π-electron systems, which lead to delocalized excited states with characteristic singlet and triplet transitions. Upon excitation, PAHs may undergo a variety of radiative and non-radiative processes depending on their structure and environment, including fluorescence, phosphorescence, intersystem crossing, and internal conversion [18]. Understanding these pathways is crucial for applications ranging from organic light-emitting diodes (OLEDs) to the detection of PAHs in interstellar space. The focus of this thesis will be on pentacene and perylene. They belong to the group of polyacenes like benzene, naphthalene, anthracene and tetracene. Pentacene has a planar structure and consists of five cata-condensed benzene rings. Similarly, perylene has a planar structure and consists of five fused benzene rings arranged in a peri-condensed fashion. A schematic view of pentacene/perylene and the energy level diagram of their lowest excited states are shown in Fig. 2.1. The intersystem crossing is a stochastic non-radiative decay from S_1 to the triplet state manifold that arises from the spin-orbit coupling [8]. When the molecule is in the triplet state, electron spin manipulation is possible by applying microwave radiation with the resonant frequency for pentacene: 1450 MHz for $|T_x\rangle \leftrightarrow |T_z\rangle$, 1344 MHz for $|T_y\rangle \leftrightarrow |T_z\rangle$ and 106.5 MHz for $|T_x\rangle \leftrightarrow |T_y\rangle$ [8]. The decay from the triplet manifold to the singlet ground state takes place as a non-radiative decay in pentacene, unlike other PAHs such as Perylene that undergoe phosphorescence decay [18]. Pentacene is often investigated as

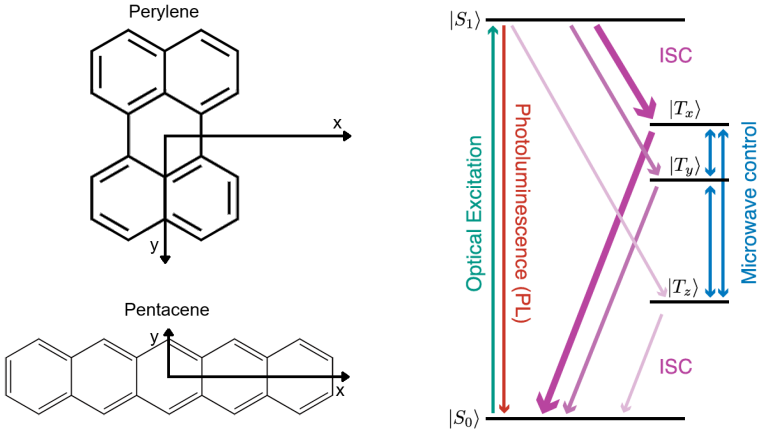

(a) (b)

Figure 2.1: (a) Molecular structure and axes of perylene and Pentacene, adapted from [14], [13]. (b) The energy level diagram of the lowest excited states of pentacene. The excitation transition is shown by the turquoise arrow. The excited singlet S_1 state decays back to the ground state (orange arrow), and undergoes an intersystem Crossing (ISC) into the triplet state manifold. The non-degenerate triplet states decay back to S_0 (purple). The faster ISC and decay rates into the ground state are indicated by the thickness of the arrow. The microwave transitions are shown in blue [14].

a probe molecule incorporated into a solid host. The most prominent host material is the p-terphenyl crystal. The p-terphenyl molecule consists of three benzene rings linearly connected by C-C single bonds and has nearly the same size as pentacene. Due to the competition of the π-electron delocalization and the repulsion of the ortho-hydrogens of adjacent benzene rings, the molecule adopts a non-planar structure, with the central phenyl ring tilted out of the plane of the two outer rings. For the doped crystal, each pentacene guest molecule replaces one p-terphenyl molecule in the lattice. Pentacene is commonly doped into p-terphenyl because it provides a transparent, inert, and crystalline host matrix ideal for optical and spin-based studies. The high triplet energy of p-terphenyl (~3 eV) prevents quenching of pentacene's lower-energy triplet state, allowing long-lived triplet populations crucial for spectroscopy and quantum spin applications. Its optical transparency ensures clean spectral measurements, and its crystalline structure offers a low-phonon, low-disorder environment, preserving pentacene's coherence properties. Additionally, doping at low concentrations avoids aggregation, enabling the study of isolated molecules in a stable, well-defined lattice. This makes p-terphenyl an ideal host for precision studies of pentacene's photophysics and spin dynamics [19].
Perylene is often used as a dopant in anthracene because its triplet states are efficiently populated through intersystem crossing. The anthracene host provides a transparent and inert crystalline matrix. The similar molecular size of perylene and anthracene ensures good lattice substitution without excessive strain, allowing isolated guest molecules to be studied. At the same time, the high triplet energy of anthracene prevents quenching of the perylene triplets, resulting in long-lived spin-polarized states [20]. These properties make the perylene–anthracene system a suitable platform for optically detected magnetic resonance studies, where strong optical signals and stable triplet populations are essential.

2.3 Triplet state Hamiltonian and spin dynamics

Due to the paramagnetic character, the photo-excited pentacene/perylene triplets in T_1 undergo several magnetic interactions which can be described by a general spin Hamiltonian

$$\mathcal{H} = S \cdot D \cdot S + S \cdot A \cdot I + g\beta S \cdot B - g_n \beta_n I \cdot B. \tag{2}$$

The first term describes the anisotropic dipolar interaction between unpaired electrons in the triplet state and is referred to as the zero-field splitting (ZFS) interaction, where S is the electron spin and D is the ZFS tensor. The second term represents the electron-nuclei hyperfine interaction, in which the hyperfine tensor A comprises both isotropic and anisotropic interactions and I is the nuclear spin. The last two terms indicate the effect of an external magnetic field B on electron and nuclear spins, respectively. g (g_n) is an electron (nuclear) g-factor and β (β_n) is the Bohr (nuclear) magneton. With 0 magnetic field strength, the ZFS interaction dominates in T_1, which leads to the removal of the degeneracy and yields the three sublevels, T_x, T_y and T_z, which are associated with the molecular symmetry axes shown in figure 2.1 (a) [8]. The molecular axes align with the principal axes of the dipolar interaction, which diagonalize the ZFS tensor D, and the Hamiltonian of the ZFS interaction can be further expressed as

$$\mathcal{H}_{\text{ZFS}} = S \cdot D \cdot S = -E_x S_x^2 - E_y S_y^2 - E_z S_z^2, \tag{3}$$

with E_x, E_y and E_z the eigenvalues of the ZFS tensor. Because the tensor is traceless, meaning $E_x + E_y + E_z = 0$, the equation 3 can be represented with only 2 variables D and E [17]

$$\mathcal{H}_{\text{ZFS}} = D\left(S_z^2 - \frac{1}{3}S^2\right) + E(S_x^2 - S_y^2) \tag{4}$$

with [8]

$$D = -\frac{3}{2}E_z \quad , \quad E = -\frac{1}{2}(E_x - E_y). \tag{5}$$

By measuring E and D, the energy spacing between the triplet states can be calculated. For pentacene, E = -0.0018 cm^{-1} and D = 0.0465 cm^{-1} the transition frequencies are [8]

$$f(T_x \leftrightarrow T_y) = -2E \approx 106.5\,\text{MHz} \tag{6a}$$
$$f(T_z \leftrightarrow T_y) = D + E \approx 1344\,\text{MHz} \tag{6b}$$
$$f(T_x \leftrightarrow T_z) = D - E \approx 1450\,\text{MHz} \tag{6c}$$

To get into the triplet state, pentacene molecules have to undergo an intersystem crossing (ISC). The ISC yield Φ_{ISC} depends on two rate constants, the spontaneous decay rate constant k_{sp} from S_1 to S_0 and the overall rate constant of the ISC k_{ISC} from S_1 to T, with the following relationship

$$\Phi_{\text{ISC}} = \frac{k_{\text{ISC}}}{k_{\text{ISC}} + k_{\text{sp}}} = 0.625 \tag{7}$$

with $k_{\text{ISC}} = 6.9 \cdot 10^7\ s^{-1}$ and $k_{\text{sp}} = 4.2 \cdot 10^7\ s^{-1}$ at room temperature. This implies that the ISC process is efficient in pentacene doped p-terphenyl at room temperature [8], [15]. Where at cryogenic temperatures, the ISC yield is $\Phi_{\text{ISC}} = 4.75 \cdot 10^{-5}$ with $k_{\text{ISC}} = 2 \cdot 10^4\ s^{-1}$ [13], making it less efficient than at room temperature.

The ISC process has been reported to be anisotropic due to pentacene molecular symmetry, spin-orbit coupling scheme and guest-host interaction [21], resulting in anisotropic population rates of the three triplet sublevels with a ratio of $P_x : P_y : P_z = 0.76 : 0.16 : 0.08$ for a short pump duration. The big difference between the populations leads to high spin polarization P_s which is defined as:

$$P_s = \frac{N_x - N_z}{N_x + N_z}. \tag{8}$$

At Room temperature, $P_s \approx 0.8$, which is quite attractive for different applications such as room-temperature masers [22], the efficient polarization transfer in triplet-DNP [23] and the strong coupling strength between pentacene triplets' spins and microwave photons [24].

The spin-lattice relaxations arise from the energy transfer from the triplet spins to the host lattice whose rate constants w_{ij} (i,j = x, y, z) are highly dependent on temperature and guest-host interactions [13]. The spin-lattice relaxations are nearly 0 in cryogenic conditions, in contrast to in ambient temperature, where the spin-lattice relaxations are $\sim 10^4$ s^{-1}. Now that the building blocks of the rate equation have been introduced, the rate equation can be studied. The rate equations of the population dynamics are [14]

$$\frac{\mathrm{d}S_0}{\mathrm{d}t} = -k_{01}S_0 + K_{10}S_1 + k_xT_x + k_yT_y + k_zT_z \tag{9}$$
$$\frac{\mathrm{d}S_1}{\mathrm{d}t} = k_{01}S_0 - (k_{10} + k_{\text{ISC}}) \cdot S_1 \tag{10}$$
$$\frac{\mathrm{d}T_x}{\mathrm{d}t} = k_{\text{ISC}}P_xS_1 - (k_x + w_{xy} + w_{xz}) \cdot T_x + w_{yx}T_y + w_{zx}T_z \tag{11}$$
$$\frac{\mathrm{d}T_y}{\mathrm{d}t} = k_{\text{ISC}}P_yS_1 - (k_y + w_{yx} + w_{yz}) \cdot T_y + w_{xy}T_x + w_{zy}T_z \tag{12}$$
$$\frac{\mathrm{d}T_z}{\mathrm{d}t} = k_{\text{ISC}}P_zS_1 - (k_z + w_{zx} + w_{zy}) \cdot T_z + w_{xz}T_x + w_{yz}T_y. \tag{13}$$

The values of the rate constants, for pentacene, can be taken from figure 2.2. From the rate equation, it is possible to derive the ratio between the triplet state population to the excited singlet state population

in the steady state condition $\frac{dX}{dt} = 0$ ($X = S_0, S_1, T_x, T_y, T_z$). The resulting system of linear equations for the triplet states can be now written as [25]

$$k_{\mathrm{ISC}} \begin{pmatrix} P_x \\ P_y \\ P_z \end{pmatrix} = \begin{pmatrix} K_x + w_{xy} + W_{xz} & -W_{xy} & -w_{zx} \\ -w_{xy} & K_y + w_{xy} + W_{yz} & -w_{yz} \\ -w_{zx} & -w_{yz} & K_z + w_{xz} + W_{yz} \end{pmatrix} \cdot \begin{pmatrix} T_x \\ T_y \\ T_z \end{pmatrix} \cdot \frac{1}{S_1} \Leftrightarrow x = A \cdot y \tag{14}$$

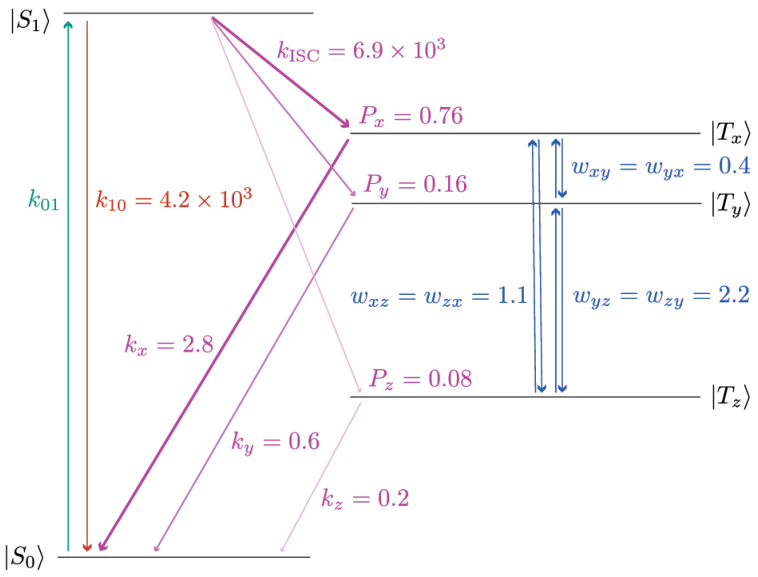

Figure 2.2: The population dynamics and its rate constants [14]. The unit of the rates is 10^4 s^{-1}.

By multiplying by the inverse of the matrix on both sides, the ratio of the populations can be calculated

$$y = A^{-1} \cdot x \tag{15}$$

The total triplet state population in the steady state depends on

$$T_1 = \sum_{i=x,y,z} T_i \propto \sum_{i=x,y,z} \frac{k_{\mathrm{ISC},i}}{k_i}. \tag{16}$$

Calculations show that, in the steady state at room temperature, the triplet state populations nearly equalize, differing by only a fraction of a percent, see in Fig. 2.3. This is the main difference between a measurement in ambient and in cryogenic conditions. In cryogenic temperatures, the spin-lattice relaxation rates are zero and the ISC is 1000 times smaller than at room temperature, leading to completely different dynamics [13], [15].

Perylene's rates have only been calculated theoretically, and there are no well-defined values at room temperature. Initial calculations suggest that the spin transitions are $|T_x\rangle \leftrightarrow |T_y\rangle \approx 1.55$ GHz, $|T_y\rangle \leftrightarrow |T_z\rangle \approx 1.72$ GHz, $|T_x\rangle \leftrightarrow |T_y\rangle \approx 3.20$ GHz.

2.4 Continuous wave ODMR

Optically detected magnetic resonance (ODMR) is the idea of transferring the detection of a microwave absorption or emission to the optical domain and taking advantage of the higher photon energy to improve

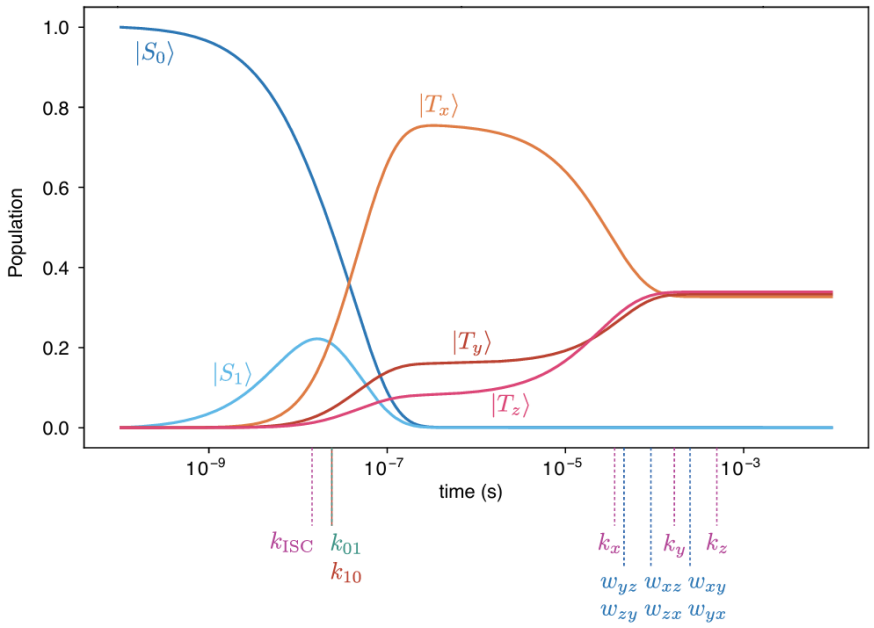

Figure 2.3: A simulation of the population dynamics [14]. The ground state population does not reach zero, it is about 10^{-3}. However, the excited state population can be approximated to be 0.

how sensitive the experiment is. ODMR works like this for pentacene, at first the molecules are pumped with a 532 nm green laser to the excited singlet state $S_0 \leftrightarrow S_1$. After a couple of milliseconds, the triplet states are in steady state due to the ISC process, spin-lattice relaxations and decay to the singlet ground state as in Fig. 2.2. By applying a microwave with a resonant frequency for the $T_x \leftrightarrow T_z$ transition, some population of the short-lived T_x level will be transferred into the long-lived T_z level. The consequence is that more molecules per unit time will be in the triplet state or, equivalently, fewer molecules reappear per unit time in the ground state. If there are fewer molecules available in the ground state, fewer molecules can be excited to the S_1 state, leading to a decrease in the fluorescence intensity [13]. A detailed explanation can be taken from the rate equation in Eq. 9. Applying a microwave field with enough power saturates the $T_x \leftrightarrow T_z$ transition and equalizes the population and decay rates of the two triplet states to first order approximation

$$k'_{\mathrm{ISC},x} = \frac{1}{2}(k_{\mathrm{ISC},x} + k_{\mathrm{ISC},z}), \qquad k'_{\mathrm{ISC},y} = k_{\mathrm{ISC},y}, \qquad k'_{\mathrm{ISC},z} = \frac{1}{2}(k_{\mathrm{ISC},x} + k_{\mathrm{ISC},z}) \tag{17}$$

$$k'_x = \frac{1}{2}(k_x + k_z), \qquad k'_y = k_y, \qquad k'_z = \frac{1}{2}(k_x + k_z) \tag{18}$$

where the primed rates are in the presence of microwaves. For the total triplet population under the influence of the resonant microwave field, one obtains

$$T'_1 \propto \left(\frac{k_{\mathrm{ISC},x} + k_{\mathrm{ISC},z}}{k_x + k_z} + \frac{k_{\mathrm{ISC},y}}{k_y} + \frac{k_{\mathrm{ISC},x} + k_{\mathrm{ISC},z}}{k_x + k_z} \right), \tag{19}$$

with $k_{\mathrm{ISC},i} = P_i \cdot k_{\mathrm{ISC}}$. The change of the number of molecules in the singlet ground state can be deduced from [25]

$$\Delta S_0 = S_0 - S'_0 = -(T_1 - T'_1) = -\Delta T_1 \propto -\frac{k_x - k_z}{k_x + k_z} \cdot \left(\frac{k_{\mathrm{ISC},x}}{k_x} + \frac{k_{\mathrm{ISC},y}}{k_y} \right). \tag{20}$$

As shown in Fig. 2.4, the ODMR contrast is quite low for continuous wave (CW) illumination at room temperature $\sim$ 0.1% – 0.01% [14], in contrast to cryogenic conditions, where the contrast can reach 20% [13]. The observed asymmetry and broadening of the magnetic-resonance lines is caused by the

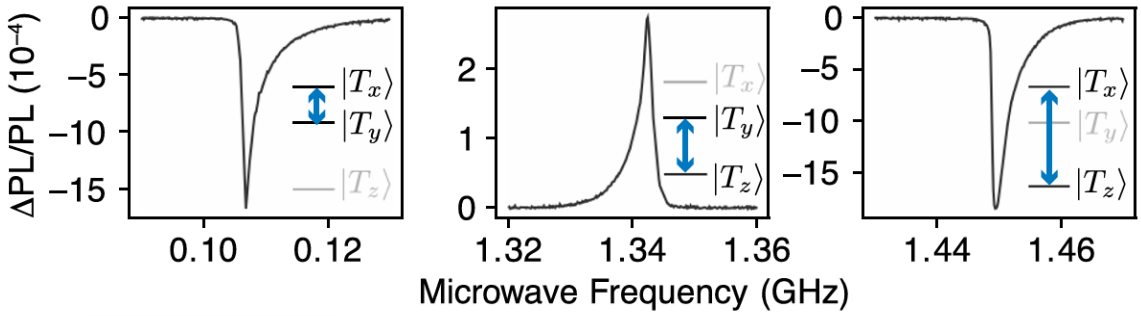

Figure 2.4: Continuous-wave ODMR spectra of a 0.01% doped pentacene doped p-terphenyl single crystal at zero field [14].

hyperfine interaction of the electronic triplet spin with the 14 nuclear proton spins ($I = \frac{1}{2}$) of pentacene. The effect of the hyperfine interaction is approximated by a second-order perturbation formalism, a detailed explanation can be found in reference [26] and [13]. The explanation can be verified by repeating the experiment on pentacene-d_{14}, where all protons are replaced by deuterium. The nuclear magnetic moment of deuterium ($I = 1$) is about 6.5 times smaller than that of the proton, and due to the second-order nature of the interaction, a considerable reduction of the linewidth is observed, see Fig. 2.5 [13].

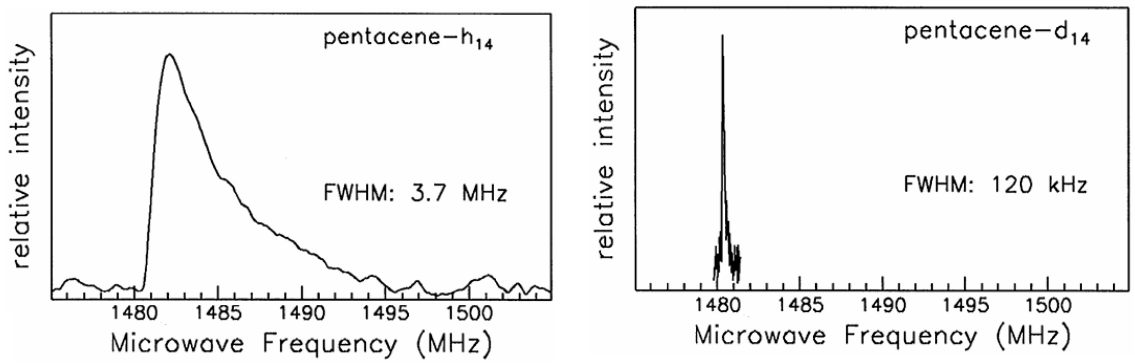

(a) (b)

Figure 2.5: Comparison of the magnetic-resonance lineshape of the $T_x \leftrightarrow T_z$ transition for pentacene-h_{14} in p-terphenyl-h_{14} and pentacene-d_{14} in p-terphenyl-d_{14}. The change in linewidth is visible, the FWHM for each line is presented in the figure [13].

2.5 Pulsed ODMR

While CW ODMR is particularly straightforward to implement, pulsed ODMR outperforms CW ODMR by eliminating optical broadening of the spin resonances, with an order of magnitude improvement in sensitivity observed in early single-NV studies [27]. Pulsed ODMR involves using short microwave

pulses to manipulate the spin states of molecules. These pulses induce coherent oscillations of the spin populations, commonly known as Rabi oscillations [14], where a spin system is first initialized into a known state with a laser pulse of the duration $10 \sim 25\ \mu$s, then subjected to a resonant microwave pulse of variable duration, τ, and finally read out with another laser pulse of the duration $5 \sim 10\ \mu$s. By plotting

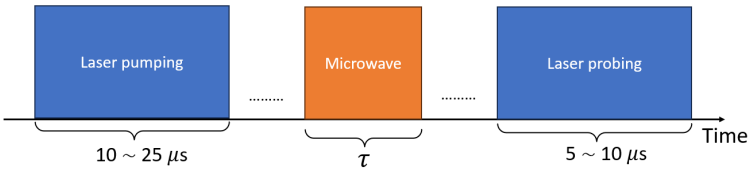

Figure 2.6: The Rabi sequence for an ODMR measurement.

the resulting photoluminescence against the duration τ, sinusoidal Rabi oscillations are observed, which directly visualize the coherent rotation of the spin between two energy levels. This measurement is crucial for calibration. The duration required to achieve the first minimum in the oscillation defines a π-pulse, which fully inverts the triplet state population, while half this duration defines a $\pi/2$-pulse, which creates an equal quantum superposition of the two states. Once calibrated, these pulses serve as fundamental building blocks for more advanced sequences. For example, a π-pulse followed by a variable delay is used to measure the spin-lattice relaxation time (T_1). A Ramsey sequence, consisting of two $\pi/2$-pulses separated by a free evolution period, measures the dephasing time (T_2^*). To probe the true spin coherence time (T_2) by canceling out noise from static magnetic fields, a Hahn echo sequence is employed, which strategically inserts a π-pulse between the two $\pi/2$-pulses to refocus the spin evolution [15]. All of those different sequences and their results are shown in Fig. 2.7.

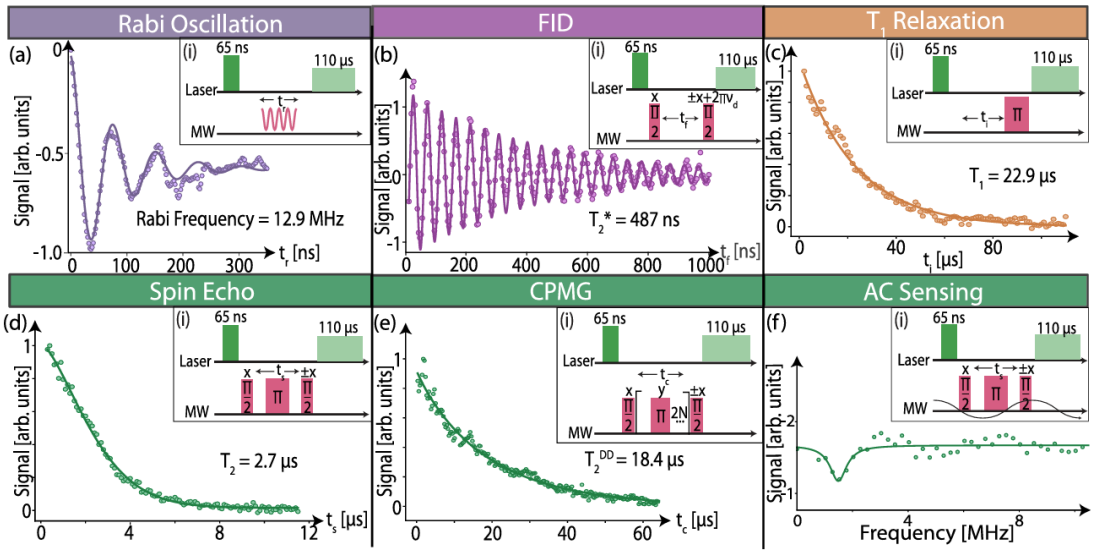

Figure 2.7: Optically detected coherent control of the photoexcited triplet focusing on the pentacene's $|T_x\rangle \leftrightarrow |T_z\rangle$ transition. The different sequences and their results that are measured at room temperature for a pentacene doped p-terphenyl crystal with 0.1% concentration [15].

3 Experimental preparation

In this chapter, the essential components of the experiment, both manufactured and acquired, are introduced and discussed. It is intended to serve as a tutorial for future students working with the setup. First, the antenna fabrication is discussed. Then, the PCB design for the omega shaped antenna is shown. After that, the sample purification method, zone refining, is briefly introduced. Afterward, crystal growth methods for perylene in anthracene, pentacene in p-terphenyl and others are presented. Lastly, the working principle of the lock-in amplifier is explained.

3.1 Antenna Fabrication

Electromagnetic radiation from antennas arises fundamentally from time-varying currents and accelerated charges. When an alternating current flows through a conductor, it produces oscillating electric and magnetic fields, which in turn propagate away from the conductor as an electromagnetic wave. The core principles are explained by Maxwell's equations, specifically Faraday's law and the Ampère–Maxwell law

$$\nabla \times E = -\frac{\partial B}{\partial t}, \quad \nabla \times B = \mu_0 J + \mu_0 \epsilon_0 \frac{\partial B}{\partial t}. \tag{21}$$

These equations indicate that a time-varying electric current (J) produces a magnetic field, and a time-varying magnetic field produces an electric field. This self-sustaining loop forms the basis of electromagnetic wave propagation in space. In antennas, especially at radio and microwave frequencies, the conductor geometry is tailored to resonantly support these oscillating currents, maximizing the radiation efficiency and directing the energy in a preferred pattern [28]. The purpose of the antenna is to generate the microwave field required for driving the spin transitions in the ODMR experiment. During the design of the antenna, it is important to characterize the impedance and match it to 50 Ω for efficient power delivery [29].
During this work, two types of antennas were manufactured: single wire antenna and Omega shaped antenna.

3.1.1 Single wire antenna

This is the first manufactured antenna, see Fig. 3.1 (a). The antenna is made out of an iron wire and shaped like a spiral.
The length and the shape of the wire are tailored carefully to have the resonances at the desired frequencies 1.55 GHz, 1.72 GHz and 3.2 GHz for Perylene in Anthracene (PR:AC). The resonances of the antenna are measured with a vector network analyzer (VNA) from Pico Technology (model PicoVNA 108), see Fig. 3.1 (b). With the PicoVNA, the S11 reflection and S21 transmission spectrum of a circuit of an antenna can be measured, and from this measurement, the radiation can be calculated. However, the S21 can not be measured, since the antenna in Fig. 3.1 is open-ended, meaning that the dips in S11 directly correlate with radiation. An antenna is considered radiating for S11 values below -6 dB, where around 75% of the power is radiated [28]. Different shapes and lengths result in different reflection spectra, see the different configurations made with different wires in the appendix in chapter App. I. The explanation can be simplified with the fact that the resonance frequency of a dipole antenna is

$$f_R = \frac{1}{2\pi\sqrt{LC}}, \tag{22}$$

where L is the effective inductance and C is the effective capacity of an antenna. Thus, by changing the shape, L and C change. The microwave circuit is shown in Fig. 3.2. A Marconi 2042 is used as a signal

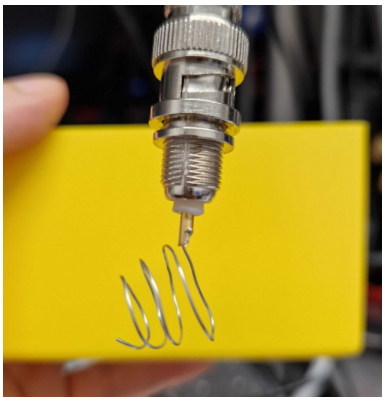

(a) Antenna soldered to a BNC connector.

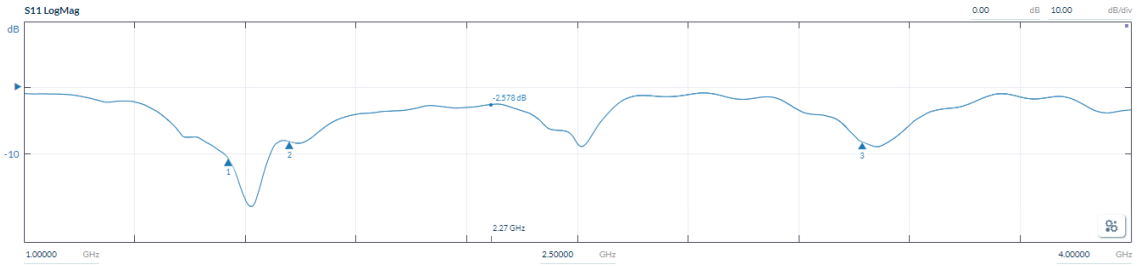

(b) The S11 reflection spectrum of the antenna. The arrows 1, 2 and 3 indicate the positions of the frequencies 1.55 GHz, 1.72 GHz and 3.2 GHz, respectively.

Figure 3.1: The first antenna. The shape is made such that the spin transitions are at resonance. Typically an antenna is considered radiating if the S11 spectrum is below -6 dB.

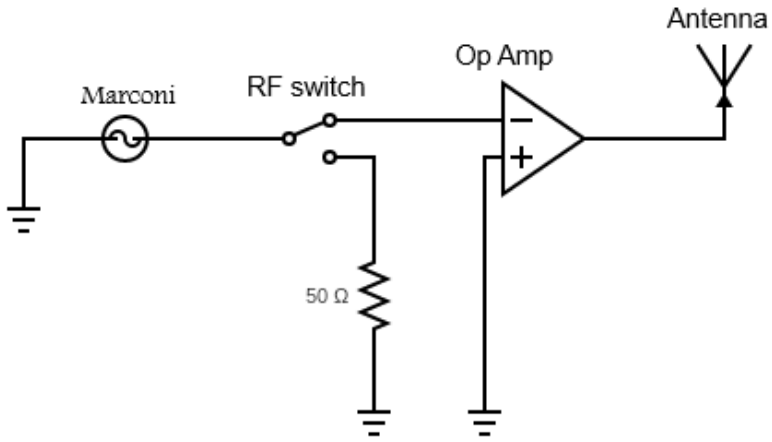

Figure 3.2: The microwave circuit used to generate microwave signal for the ODMR experiment.

generator. The signal generator can generate waves up to a frequency of 5.2 GHz and 13 dBm power. The Marconi is an old device that does not respond to a fast triggering signal, which is why a nanosecond RF switch, Mini-Circuits ZYSW-2-50DR+, is used for pulsing the microwave using a TTL signal from

the MFLI lock-in amplifier (introduced in Chapter 3.5). The RF switch has two outputs, one of which is amplified with a 53 dB operational amplifier, Mini-Circuits ZHL-25W-63+, and the other output is terminated with a 50 Ω terminator. The output of the amplifier is then fed to the antenna and radiated. This antenna has the advantage that it is easy to build, made out of cheap material, and easy to modify the resonant frequency. However, the disadvantages outweigh the advantages. The problem with this antenna is that it radiates the energy in all directions, does not focus the waves of the sample, affects other electronics around it, and is a safety hazard (exposed wire). Thus, after attempting to search for ODMR with this antenna, the omega shaped antenna is introduced to the experiment.

3.1.2 Omega shaped antenna

A more sophisticated antenna is required to achieve a homogeneous field distribution, higher microwave power delivery, broader bandwidth, and improved reliability. Ideally, the antenna is close to the sample such that less microwave power is lost. The omega shaped antenna, shown in Fig. 3.3, fulfills all these requirements. However, the fabrication of this antenna is more challenging than the wire antenna and requires a clean room for the lithography.
The sample is placed in the inner circle of the antenna, where the fields are homogeneous. The method that is used for antenna fabrication is called the liftoff method. The steps of the procedure are shown in Fig. 3.4.

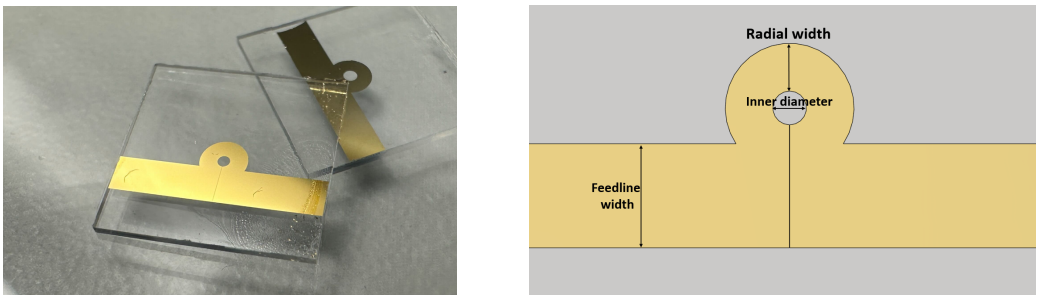

(a) Gold antenna on fused silica substrate. (b) A schematic of the antenna with its parameters.

Figure 3.3: Omega shaped antenna with a 300 μm inner-circle diameter and 7 μm gap width.

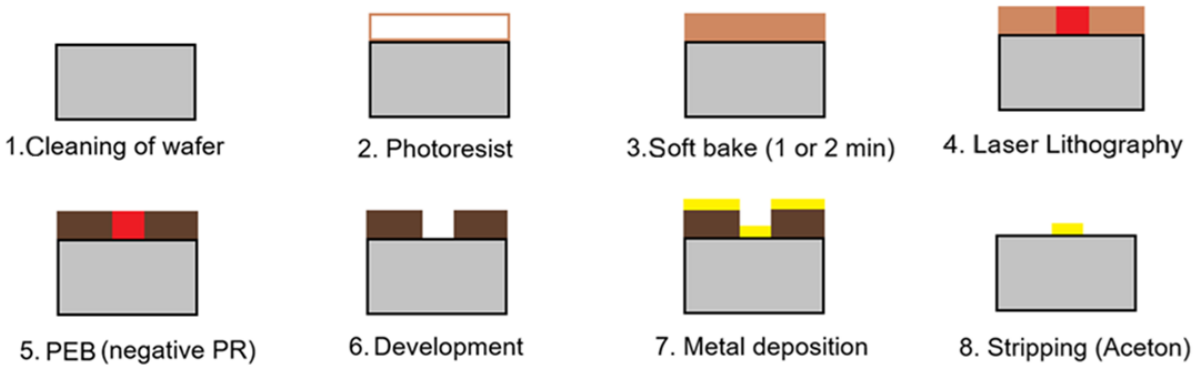

Figure 3.4: The steps of the liftoff method for antenna fabrication in a clean room.

Here is a detailed description of the antenna fabrication process:

1. Design and simulation:
The antenna design is based on the following reference [30]. The dimensions for the antenna are:

$$\text{feedline width} = 1.85\,\text{mm}, \quad \text{radial width} = 1.15\,\text{mm}, \quad \text{gap width} = 7\,\mu\text{m}$$
$$\text{inner diameter} = 300\,\mu\text{m}.$$

A CAD design of the antenna is made, see Fig. 3.3 (b), and is integrated into the setup file, to ensure that the dimension of the antenna matches the sample holder, as shown in Fig. 3.5. The 3D printed sample holder is modified for the 10.3 mm x 10.3 mm antenna substrate to fit in smoothly. Then, a simulation of

Figure 3.5: CAD design of the antenna in the sample holder.

the fields of the antenna is carried out using the software "Ansys Electronics Desktop Student 2024 R2". The simulation results match the results presented in the reference [30], see Fig. 3.6. After verifying

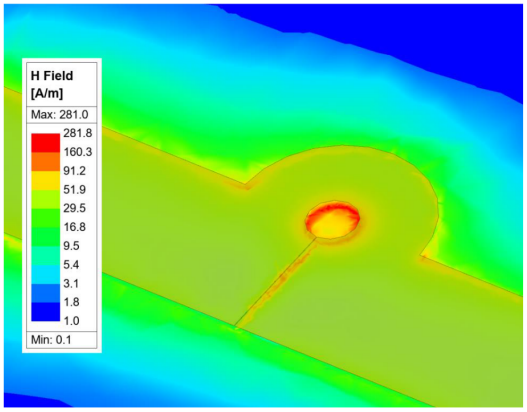

Figure 3.6: Simulation of the H field, induced by the antenna with 1 V. The field is measured 1 μm above the antenna plane.

the design and the simulation of the antenna, the GDS design of the antenna for fabrication in the clean room can be started. The GDS file describes the layers, material, and size of the device. Then, the file is fed into the laser writing machine, which contains the information about which layer and material need to be written. When the antenna is manufactured on a fused silica wafer of 10 cm diameter, 45 antennas are built. The GDS design, shown in Fig. 3.7, shows the gold structure of the antenna (in blue) and the fused silica substrate (in pink). In this design different parameters are used for the inner circle and gap to

study their effects on the resonance frequency, the gap ranges from 7 μm to 17 μm and the inner diameter ranges from 300 μm to 700 μm. The study of the effect of the different gaps and inner diameters is shown in the appendix in Chapter App. II.

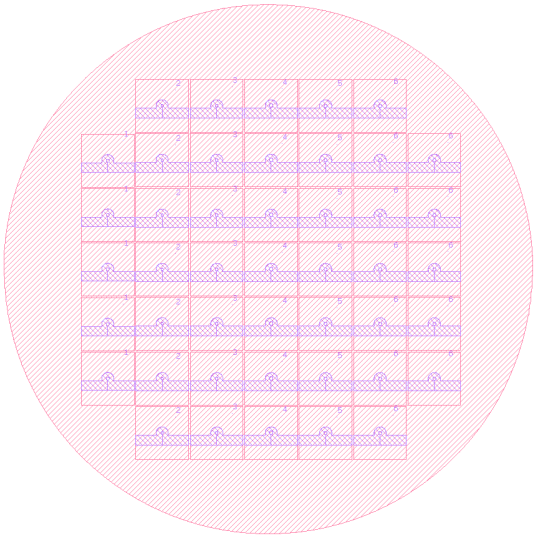

Figure 3.7: The GDS design of the antenna array for the fabrication in the clean room. On the first column (on the left side) are the antennas with (gap, inner diameter) = (10 μm, 300 μm), second column (10 μm, 500 μm), third column (10 μm, 550 μm), fourth column (10 μm, 700 μm), fifth column (17 μm, 300 μm) and sixth and seventh (7 μm, 300 μm).

2. Cleaning:
The newly purchased wafers are immersed in acetone with a gentle wave-like motion for 2 minutes to effectively remove surface dust and contaminants. Following this, the wafers are rinsed in deionized (DI) water for 1 minute and then in Milli-Q water (ultrapure grade) for another minute. The wafer can be dried with dust-free towels or in an oven. After the solvent rinse, the wafers are submerged in fuming nitric acid (HNO_3) for 2 minutes to remove any remaining organic residues. This is followed by the same DI and Milli-Q water rinse sequence used after the acetone step. Before handling HNO_3, appropriate chemical protective clothing must be worn, including acid-resistant gloves, apron, and face shield, as exposure poses significant hazards.
3. Spin coating of photoresist:
In photolithography, photoresist is a light-sensitive material applied to a substrate (such as a silicon wafer) to define patterns. The two main types are positive and negative photoresist, and they behave oppositely when exposed to UV light. In a positive photoresist, the regions that are exposed to light become more soluble in the developer solution. As a result, the exposed areas are washed away, while the unexposed areas remain on the wafer. This means that the pattern on the photomask is a direct copy of the final pattern on the wafer. In contrast, a negative photoresist behaves in the opposite way. When exposed to light, the resist undergoes cross-linking, which makes the exposed areas less soluble in the developer. Therefore, the unexposed areas are removed during development, and the exposed areas remain on the wafer. This means the photomask must have the inverse of the desired pattern [31].
After many trials and errors, the negative photoresist "AZ-nlof 2020 photoresist" is the most suitable for this project, because of its high viscosity and short development time. To coat the wafer surface with photoresist, the wafer is first mounted on the spinner. The photoresist is then poured onto the center of

the wafer, covering approximately 70 – 80% of the surface. The spinner is initially set to 500 rpm for 30 seconds to ensure uniform coverage, followed by 2000 rpm for 90 seconds to thin the photoresist.
The wafer is then transferred to an oven for soft baking at 100 °C for 60 seconds to evaporate the solvents. The thickness of the photoresist can be probed optically using the Filmetrics Mapper by analyzing light reflected from the wafer surface across multiple points using spectroscopic reflectometry. A measurement with the Filmetrics Mapper is shown in Fig. 3.8. Based on experience, on the fused silica wafer, the applied "AZ-nlof 2020" photoresist with the settings mentioned above has a typical thickness of around 3.79(4) μm.

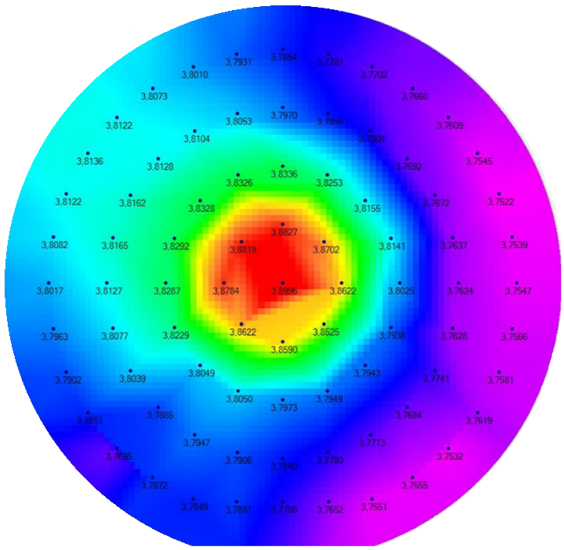

Figure 3.8: A screenshot from the software "FILMETRICS" showing the thickness distribution of the photoresist on the wafer. The non-uniform, smeared appearance is due to the photoresist not being poured perfectly centered on the wafer.

4. Laser lithography:
The wafer is prepared for direct laser writing exposure. For the laser writing, the GDS file done in step **1. Design and simulation** is uploaded to the laser writer machine. However, it is crucial to invert the patterning settings, as a negative photoresist requires that the exposed regions correspond to the areas surrounding the antenna structure, rather than the antenna itself. As previously noted, exposure to UV light causes the negative photoresist to harden, making it insoluble during the development process. The dose for silicon wafers is set to **100 mJ/cm**^{2}, based on prior testing, which demonstrated good results. In contrast, fused silica wafers, being transparent, do not reflect or scatter the laser power significantly. Consequently, higher energy densities are required for effective exposure. For fused silica wafers, doses of **200 mJ/cm**^{2}, **250 mJ/cm**^{2}, and **300 mJ/cm**^{2} are used during processing, all are successful.
After the development, negative photoresist must be baked again, this step is called post exposure bake (PEB). PEB is essential for negative photoresist as it completes the cross-linking reaction initiated by UV exposure, ensuring that the exposed areas become fully insoluble during development. It also improves image contrast, adhesion, and surface smoothness, preventing feature loss and enhancing pattern fidelity [31]. PEB is done at 100 °C for 60 s. Afterwards, the development is performed using "AZ 726 MIF" Developer. Development removes the unexposed, uncross-linked regions of the negative photoresist, revealing the desired pattern while leaving the hardened, exposed areas intact [31]. According to observations, careful monitoring is required after 25 seconds of development, with completion typically

reached around 45 seconds. For example, the wafer exposed at **300 mJ/cm**^{2} is developed for 50 seconds, the resulting pattern is shown in Fig. 3.9. The structure of the remaining photoresist is analyzed using a stylus profilometer or a microscope.

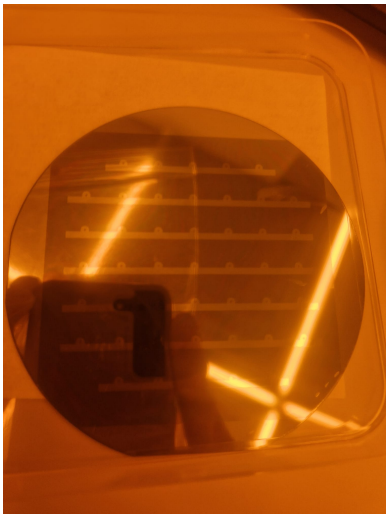

(a) The image is showing the wafer after development. The black area around the antenna is the hardened photoresist.

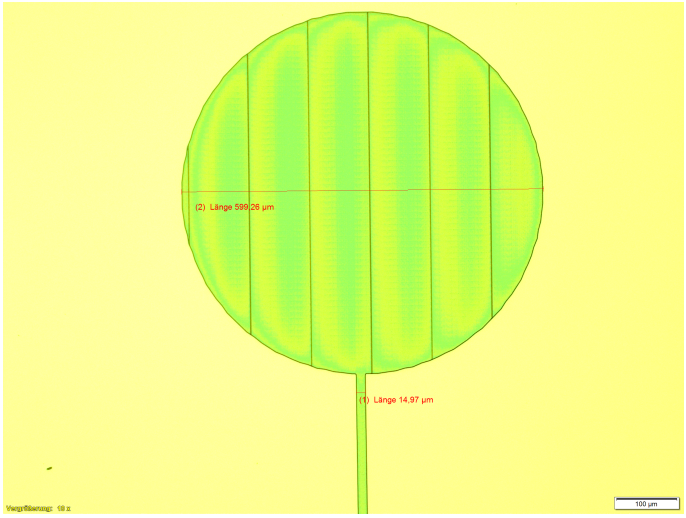

(b) Microscopic image of the photoresist pattern. The striped region corresponds to the photoresist, which appears this way due to UV laser exposure. The surrounding clear area represents the bare substrate.

Figure 3.9: The wafer after development. The quality of the development is checked with the microscope.

5. Metal Evaporation:
The metal evaporation is performed with "UNIVEX250", see Fig. 3.10. The chamber is always in high vacuum even when not operating, to ensure the least amount of contamination. For the operation of the machine, first, the ventilation is turned on to increase the pressure to ambient pressure. Then, the chromium bar is checked to see whether there is enough material on it. Cr is used as an adhesive layer between the substrate and gold. Afterward, gold is filled in its holder, and both of the gold and Cr holders are connected to a high current source to evaporate them under vacuum pressure. The next step is to mount the processed wafer in the wafer holder, shown in Fig. 3.11. The sensor (Quartz crystal) for measuring the evaporation rate should be checked in the control box of the machine. If its remaining lifetime is below 90%, it must be replaced with a new one. Before starting the vacuum pumps, it is important to check if the shutter, which blocks the vapor from going on to the wafer when not needed, is movable and operating as intended. Then the vacuum pumps are started. When the pressure inside the chamber drops below 10^{-6} mbar, the high current controller is turned on, and then on the deposition controller the recipe No.25: Chrom20_Au300 is selected, and the process is initiated by pressing Start, and the procedure runs automatically. The high current controller activates OUTPUT1, heating the chromium stick until it glows upon reaching the required temperature. At that point, the lower shutter is automatically moved aside. The evaporation rate is measured by the sensor, with the current value displayed under "Rate SP". When the rate reaches the preset threshold, the upper shutter opens, enabling Cr to be deposited onto the wafer. After the Cr layer is completed, the same sequence is repeated for gold evaporation. The high current controller automatically switches to OUTPUT2 for this purpose. Once the evaporation is complete, the system should be vented as previously described. The chamber is then opened, the upper shutter moved aside, and the wafer is carefully removed. The wafer after the evaporation process is shown in Fig. 3.12

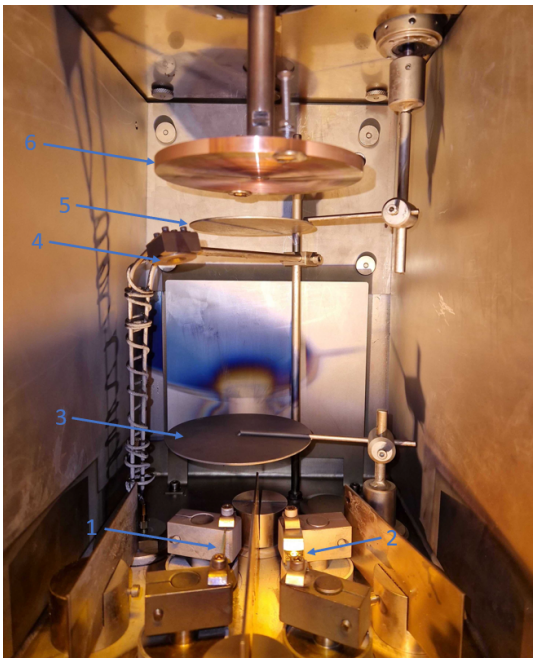

Figure 3.10: Inside of the evaporation chamber of UNIVEX250. The different components are, 1: Chromium stick for the Cr evaporation, 2: Gold cup for the Au evaporation, 3: first shutter to block the Au and Cr sources, 4: Quartz crystal that oscillates with a well known frequency, this frequency changes depending on the thickness of the evaporated metal and hence the evaporated thickness can be measured accurately, 5: shutter in front of the wafer holder and 6: the home-made wafer holder.

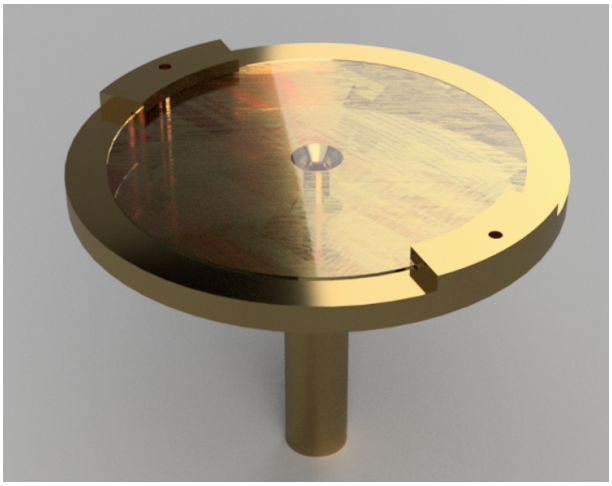

Figure 3.11: The wafer holder. The 10 cm diameter wafer is placed in the middle and screwed firmly with metal pieces to the holder.

(a). The chamber window must be cleaned with soap, dried using tissue paper and compressed air, and then returned to its proper position. If the system is not required immediately, the chamber should be closed and the pump restarted to restore the vacuum. To remove excess metal, the wafer is immersed in acetone and cleaned using a supersonic bath. It must then be rinsed with fresh acetone and DI water and

thoroughly dried, the result is presented in Fig. 3.12 (b).

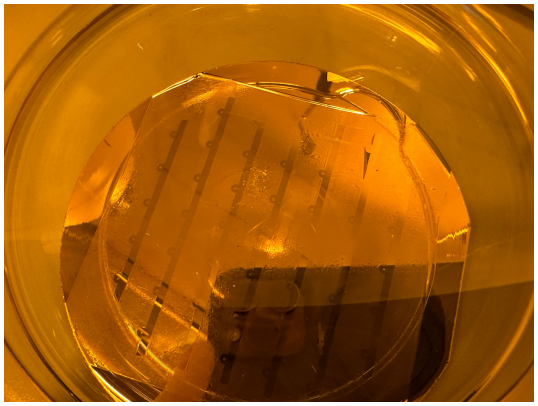

(a) Wafer in beaker filled with Acetone after gold evaporation.

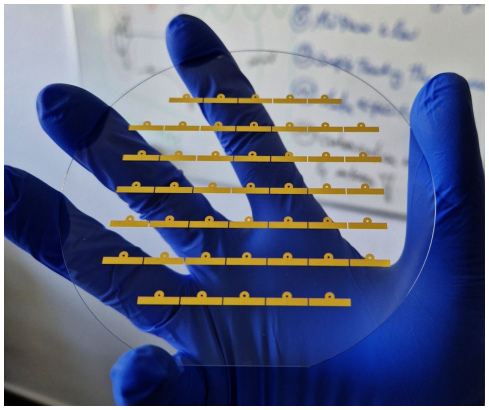

(b) The wafer after the stripping process.

Figure 3.12: The processed wafer after the evaporation process.

6. Dicing:
The Dicing is performed with the Machine "DISCO DAD 3660". To begin, the wafer is placed on the holder and secured with tape. The sample holder is placed in the machine, and then the vacuum pump is turned on. Afterwards, the design-specific data is fed into the machine, such as how many dicing lines for each direction, in which orientation the wafer should be, the separation between the dicing lines, which blade to use (two blades available), the height of the blade (should be larger than 0.1 cm), etc. After that, the alignment of the wafer is started. In the menu, "semi-automatic dicing" is selected, and after making sure the settings are correct, the dicing is started. When the process is done, the vacuum pump is turned off, and the wafer holder is taken out. The diced wafer remains intact because the blade is set 0.2 cm above the bottom surface. Individual antennas are then separated by applying pressure to the backside of the wafer. Wearing proper protective glasses is essential when cracking the wafer to protect the operator's eyes. After the fabrication, there are 45 antennas to be used. The antennas are then examined under the microscope for any errors during the fabrication, and important features, such as the gap width and inner diameter, are well studied with the stylus profiler. The result of the stylus profiler is shown in Fig. 3.13 (b) for the inner circle and in Fig. 3.13 (c) for the gap width. Around the edges of the antenna more metal accumulates. This happens because, during directional metal evaporation, incoming atoms accumulate at the vertical edge between the taller photoresist and lower silicon due to shadowing and sidewall deposition, forming a thicker metal ridge. This ridge occurs because atoms hitting the resist edge scatter and pile up at the base, increasing local metal thickness [32].

3.2 PCB for omega antenna

There are a couple of methods to connect the Omega antenna to the power source, which are: soldering an SMC or SMPM connector directly on top of the antenna, wire-bonding a gold wire from the antenna to a PCB, or soldering a finger contact on the PCB that touches the antenna. All of the methods mentioned above would work, but with disadvantages. Soldering an SMC or SMPM connector directly onto the antenna may seem simple, but it adds several problems. A significant part of the radiation is emitted at the connector and solder joint, and placing a connector directly on top requires high mechanical stability to withstand the torque exerted by attached cables. On the other hand, wire-bonding a gold wire from

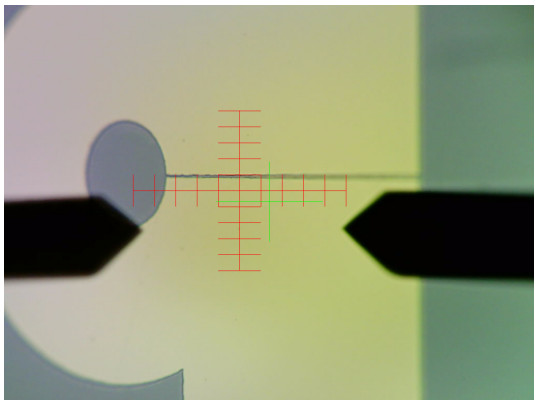

(a) Antenna in the stylus profiler machine. The tip of the stylus is the one on the left, and the other one is a reflection.

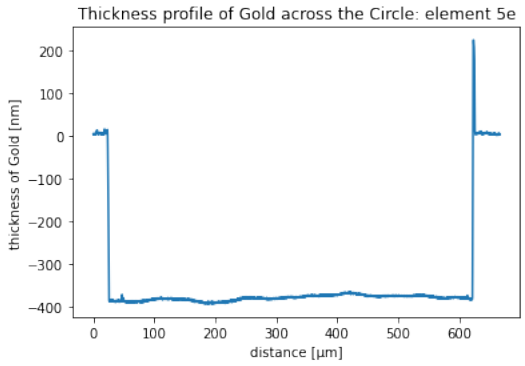

(b) The inner circle diameter of the element in the 5th row and 5th column on the wafer.

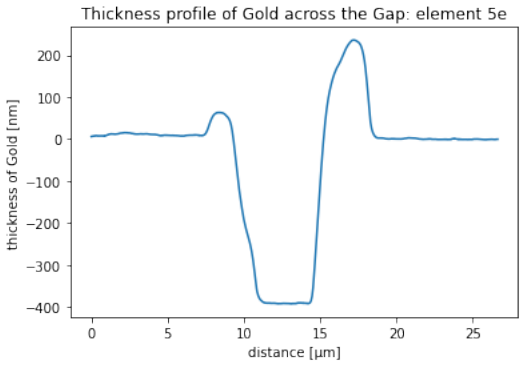

(c) The gap of the element in the 5th row and 5th column on the wafer.

Figure 3.13: The measurement of the relevant features of the antenna with the stylus profiler.

the antenna to a PCB is more complex and carries a drawback: the impedance is difficult to match due to the gold wire. Furthermore, if the antenna requires cleaning, the wire bond is permanent, preventing the use of an acetone bath for cleaning. The finger contact method presents the fewest disadvantages, and issues such as impedance mismatch can be mitigated through careful design. This approach is also more durable than any other method. The PCB and sample holder have been specifically designed to implement the finger contact connection with the antenna.

The design is made with the software "Fusion 360". The design is shown in Fig. 3.14. The red areas represent the top copper layer, while the blue indicates the underlying substrate. The small holes along the feed-line are vias. The green holes on the PCB's edge are for the 90° SMA connector. The white circular holes are for mounting the PCB to the sample holder, and the central opening allows the laser to illuminate the crystal. The gold-coated finger contacts, shown in Fig. 3.15, are soldered to the square pad in the middle of the PCB. The software provides the feature, circuit analyzer. This feature measures the impedance of the connection (either signal 1 or signal 2). The length of the signal 1 and signal 2 feed lines must be adjusted so that the impedance of the circuit is 50 Ω. The main factors affecting the impedance are feed-line width, feed-line length, spacing to ground plane, and the substrate material and layer thickness. These values are chosen carefully to keep the impedance at 50 Ω. The feed-line is angled

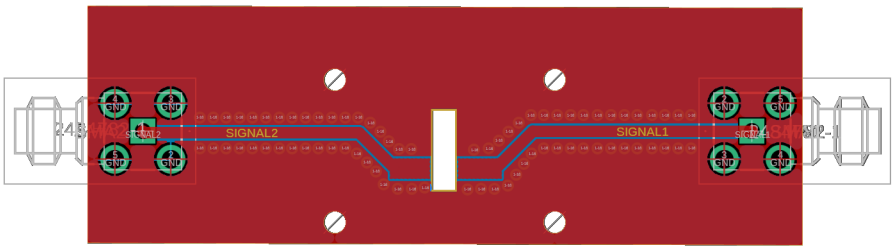

Figure 3.14: Top view of the 2D electrical layout on the PCB that delivers power to the antenna. The copper around the feed-line and the bottom copper layer are ground.

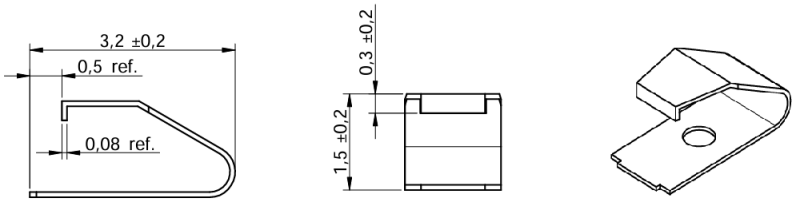

Figure 3.15: The gold-coated finger contacts ordered from Würth with the part number 331031321515.

at 45° instead of 90°, as a larger angle increases the reflection and thus impedance. To maintain signal integrity, wires pass through the vias and are soldered to both the top and bottom ground copper layers. The connection between the antenna and the PCB is realized with the 3D printed sample holder. The screw holes are accurately placed to position the finger contacts against the antenna's outer edges, thereby establishing the electrical connection, see Fig. 3.16.

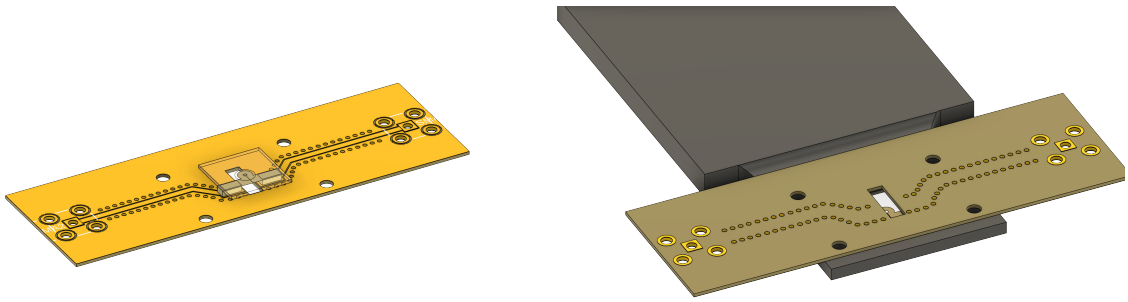

(a) Bottom view, without the sample holder.

(b) Top view.

Figure 3.16: The sample holder, PCB and antenna CAD construction.

3.3 Zone refiner

High-purity crystals are essential for molecular experiments, as even trace amounts of chemical or structural impurities can drastically affect electron dynamics, charge transport, and optical properties.

Commercially available substances often contain residual contaminants and structural defects that act as quenching centers or trap states, leading to broadened spectral features and reduced coherence times. A zone refiner is therefore employed to achieve ultra-high purity by exploiting the segregation of impurities during repeated partial melting and recrystallization. A zone refiner works on all substances that melt without decomposition by slowly moving a narrow molten zone along a solid rod of material. Most impurities have a segregation coefficient different from that of p-terphenyl or anthracene, causing them to remain in the melt rather than the solid phase. By repeatedly passing the molten zone through the material, these impurities are swept toward both ends of the tube, yielding a highly purified crystal in the middle suitable for sensitive molecular experiments. A concentration gradient of the impurities is shown in Fig. 3.17. Zone-refining enables the preparation of bulk p-terphenyl crystals with impurity concentrations

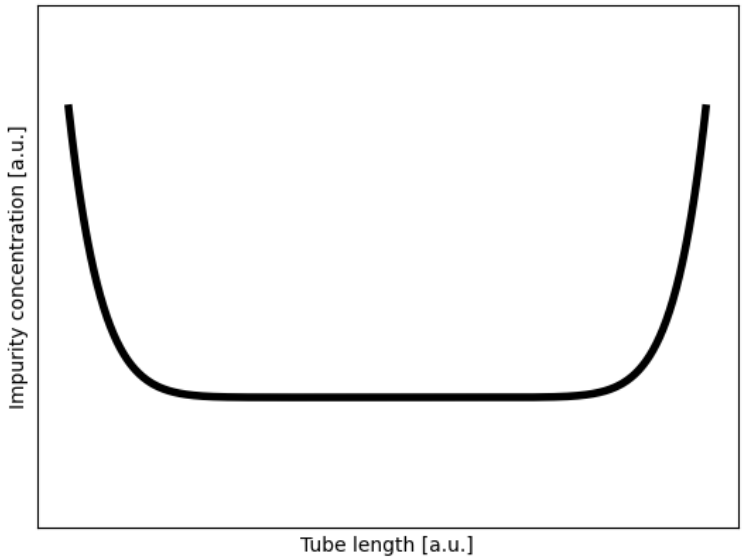

Figure 3.17: A schematic representation of the distribution of impurities in a zone-refining tube. The impurities can be collected at either end, depending on their solubility.

low enough to allow reproducible, high-resolution measurements of pentacene's photophysical and spin properties [17].
All credit for building the zone refiner goes to my colleague Kathrin Schumacher. The home-built zone refiner is shown in Fig. 3.18. The zone refiner consists of an outer glass tube with an inner diameter of 9 mm and an outer diameter of 11 mm, around which the heating coils are wound. These coils are made of 80/20 Ni–Cr alloy and are connected to a voltage supply, where they function as resistive heaters. The regions between the heating coils serve as cooling zones, maintained at room temperature, where the substance crystallizes. A thinner 8 mm glass tube is inserted inside the outer tube, holding the copper rod. The rod is mounted on a motorized translation stage with a 2.5 cm travel range, which drives the inner tube through the heating zones. The current setup allows for a minimum translation speed of 2 mm/h, which is sufficient for this application.
To zone-refine, for example, p-terphenyl, the substance is loaded into the inner tube. If a large quantity is to be purified, during the loading of the powder-like p-terphenyl, it is recommended to melt it with low heat to lower its volume. The glass tube is installed in the setup shown in Fig. 3.20 to be evacuated and placed in an inert atmosphere for zone refining. First, the tube is evacuated to 3 mbar. It is crucial to note that filling the tube to the brim should be avoided, because the substance may be drawn out of

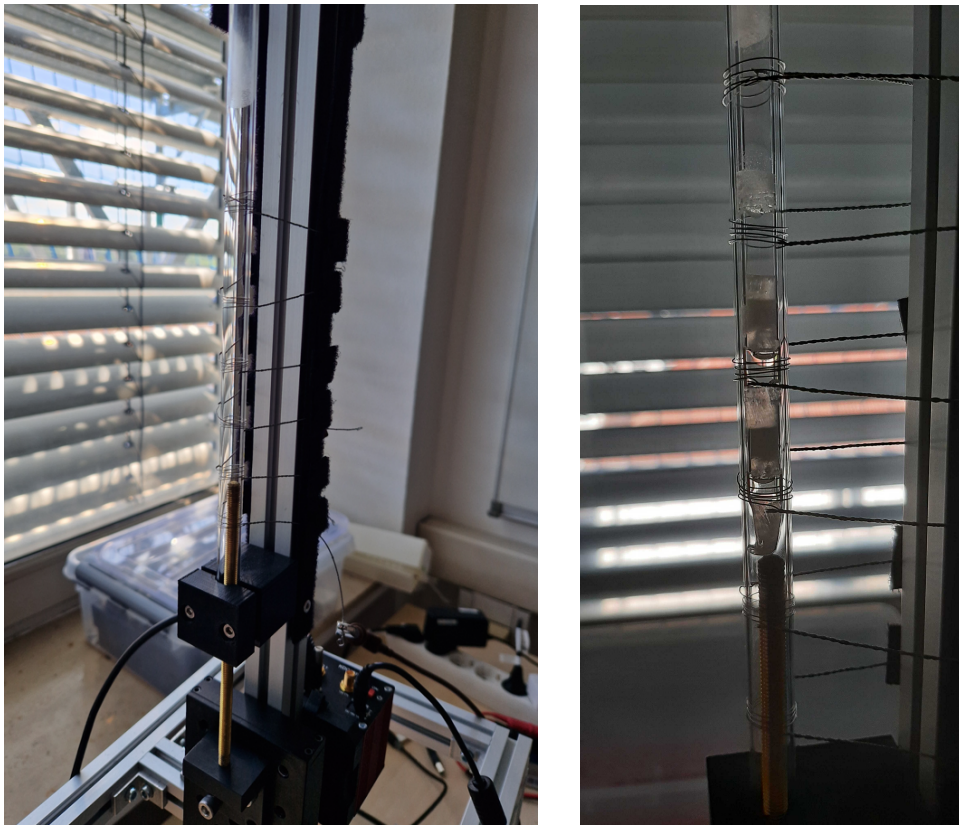

(a) The zone refiner. (b) zone-refining p-terphenyl.

Figure 3.18: The zone refiner built in our research group. The molten zones can be seen next to the heating coils. At the cold zones, the molecules are solidified. The copper rod is connected to motorized translation stage that pushes the inner glass with the substances through the zones.

the tube if it is too close to the opening. When the target pressure is achieved, the tube is filled with nitrogen until the pressure reaches 1 bar, then the vacuum is pulled again. This process is to be repeated at least three times. In the final run, the nitrogen pressure inside the tube should be around 850 mbar to avoid oxidation when purifying. Afterward, the tube is sealed with a blow torch. The glass tube is then transported carefully to the zone refiner, and the process begins. The voltage supply is turned on, then the voltage is raised very slowly, and the substance is carefully monitored. The melting temperature of p-terphenyl is 213 °C [33]. When the melting temperature is achieved, raise the voltage slightly higher to ensure that the melting happens everywhere. In Fig. 3.18, p-terphenyl is being zone refined. The heating and the cooling zones are visible.

To test if the zone refiner works as intended, the purity of the sample can be tested by probing the triplet excitons T_1. All foreign molecules that form energy levels below the exciton transport bands lead to trapping of the excitation energy and hence to localization of the excited quasi-particles. Triplet exciton lifetimes τ can be measured by delayed fluorescence under low triplet excitation density, where, after a pulse excitation, the decay rate

$$\frac{dT_1}{dt} = \frac{1}{\tau} \cdot T_1 + \gamma \cdot T_1^2 \tag{23}$$

is dominated by the linear term, whereas the contamination is monitored by the second term, leading to delayed fluorescence via the process $T_1 + T_1 \rightarrow S_1^*$. The lifetime τ is a sensitive function of crystal purity [34], see Fig. 3.19 taken from the reference [17]. This step is still under development. Other known

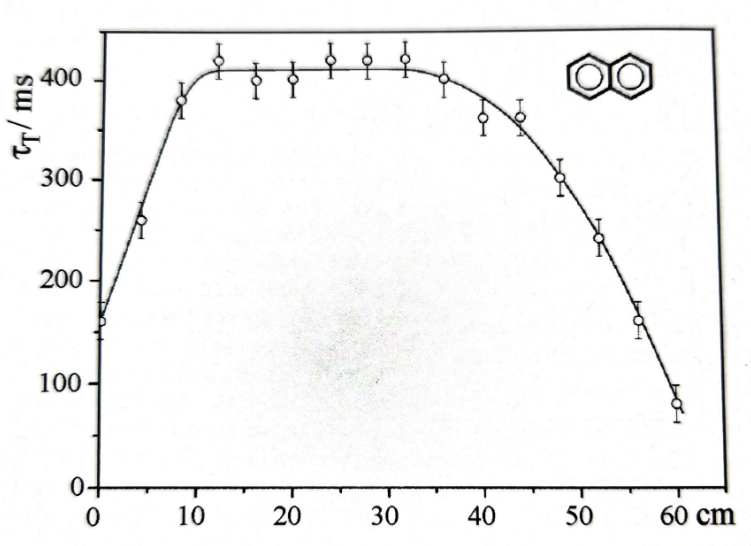

Figure 3.19: In a tube filled with zone-refined naphthalene, in the central region, where the purity is the highest, a triplet exciton lifetime is the highest as well. This value can be compared with literature to benchmark the purity [17].

methods to characterize the purity are Gas Chromatography and mass spectrometry.

3.4 Crystal growth

Two methods of crystal growth are used for the experiment, co-sublimation and the Bridgman method. The crystals created are perylene doped anthracene (PR:AC), PTCDA doped anthracene (PTCDA:AC), pentacene doped p-terphenyl (PC:PTP), and deuterated pentacene doped deuterated p-terphenyl (dPC:dPTP). All of the molecules are bought from the seller "Sigma-Aldrich" with a purity around 95%.

3.4.1 Co-sublimation method

Co-sublimation is a solvent-free crystal growth method in which two or more components are simultaneously sublimated and subsequently condensed to form a multicomponent crystalline phase. Unlike conventional solution crystallization, which depends on solvent compatibility and may suffer from solvent inclusions or contamination, co-sublimation avoids such issues by directly utilizing the solid–vapor–solid pathway. In this process, the solid substances are heated until they sublimate, and the resulting vapor mixture migrates under a controlled temperature gradient to a cooler region where condensation occurs. Furthermore, because it avoids solvents altogether, the resulting crystals are often of higher purity and less prone to defect formation [34]. The setup is shown in Fig. 3.20.
For the crystal growth, the molecules are weighed and added to the flask. It is recommended to use less than 1 g of host molecule (anthracene, p-terphenyl) so that not many crystals are grown. The guest molecules (perylene, PTCDA, or pentacene) are added depending on the desired concentration. Then the flask is placed in a vacuum, and afterwards the heat gun is set to 300 °C and aimed at the bottom of the

Figure 3.20: The sublimation setup used for PR:AC and PTCDA:AC crystals. The components numerated are, 1: N_2 Gas line from source to the setup, 2: N_2 Gas line that flows into to the flask, 3: Vacuum line connecting the vacuum pump with the flask, 4: flask, 5: pressure gauge at the flask, 6: venting opening, 7: pressure gauge for the N_2 Gas line at the component number 2. and 8: heat gun [35].

flask. After a couple of seconds, the crystals can be seen raining down in the flask. At that moment, the heat gun is turned off. After venting, the crystals, which can be seen in Fig. 3.21, are picked up with the appropriate tool. The resulting crystals are on the order of 10^{-6} m in thickness and exhibit a relatively large surface area. It is possible that many crystals stack on top of each other, leading to a chaotic sample, see Fig. 3.22. To obtain a good crystal, it is recommended to collect them from the upper part of the flask, where fewer crystals form, thus avoiding stacking. Anthracene forms thin, hexagon-like crystals, while its lattice is not hexagonal. This pseudo-hexagon arises from anthracene crystals growing along the (001) plane, where equivalent edge planes intersect at about 60° This stabilizes faceted growth and producing a hexagonal shaped crystals. In contrast, p-terphenyl grows as circular or disk-like crystals. Here, the lateral growth rates are more isotropic due to the way the linear p-terphenyl molecules pack, so distinct facets do not stabilize. The edges smooth out during sublimation, and radial growth enhances the circular appearance. Thus, the difference in shapes reflects how anisotropy in surface energies leads to faceted anthracene crystals, while isotropy in growth produces rounded p-terphenyl crystals [17].

3.4.2 Bridgman method

In contrast, the Bridgman method is one of the oldest and most widely used melt growth techniques for producing large single crystals. The method relies on the principle of directional solidification. A material is placed in a glass tube under an inert atmosphere and heated above its melting point in a high-temperature furnace, the same furnace used for zone refining in Fig. 3.18. The tube is then slowly translated through a well-controlled temperature gradient from a hot zone into a cooler zone. Solidification begins at the cooler end, and if a seed crystal is placed at the bottom, epitaxial growth occurs. This leads to the formation of a large single crystal that inherits the orientation of the seed crystal.

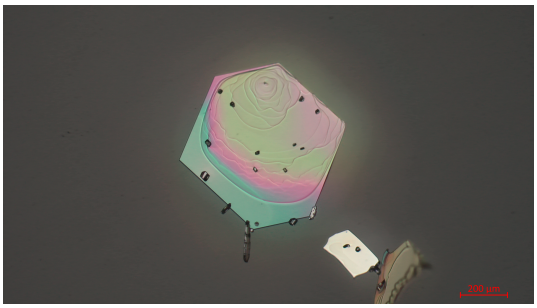

(a) PTCDA:AC crystal with 0.01% concentration

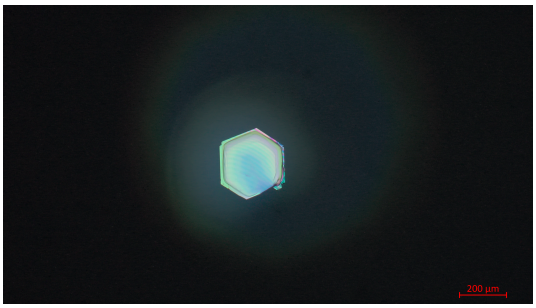

(b) PR:AC crystals with 0.1% concentration

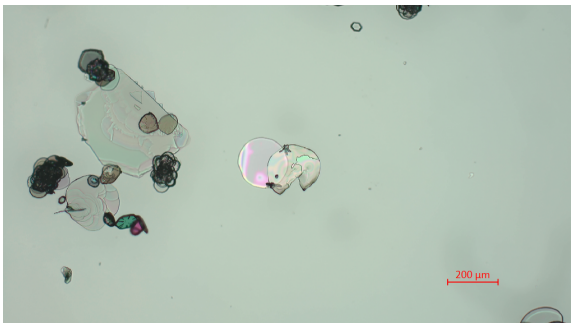

(c) PC:PTP crystals with 0.1% concentration

Figure 3.21: The Crystals that are used in the experiment [35].

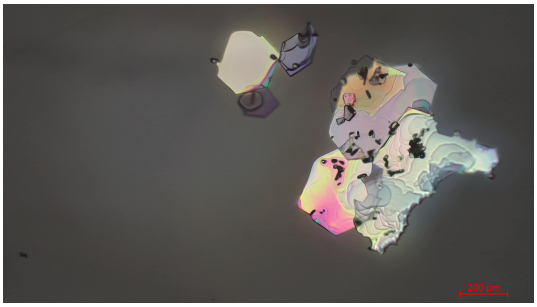

(a) many stacked crystals.

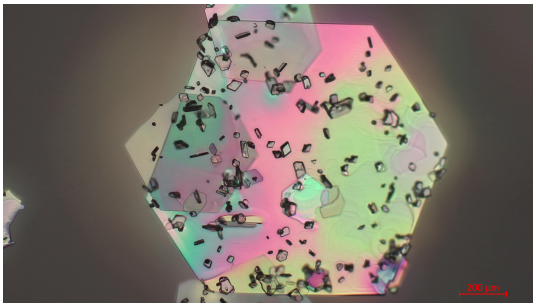

(b) many small crystals on a much bigger crystal.

Figure 3.22: Some of the resulting crystals that did not go well. many small crystals are stacked on top of them [35].

Careful regulation of the solidification front is crucial, as uncontrolled thermal gradients or cooling rates can cause dislocations, cracks, or compositional inhomogeneities. The resulting pentacene in p-terphenyl crystal (PC:PTP) with ~0.03% dopant concentration and deuterated pentacene in deuterated p-terphenyl (dPC:dPTP) with ~0.07% dopant concentration. The crystals are shown in Fig. 3.23. In the PC:PTP sample in 3.23 (a), the oxidation layer on the surface forms due to a small amount of oxygen leaking in. In the dPC:dPTP sample, the temperature was set to 370 °C instead of 270 °C which caused most of the material to disintegrate, leaving a small amount of crystallized material. This small portion can be integrated into the setup.

(a) PC:PTP crystal grown at 270 °C. The inhomogeneity can be observed due to insufficient mixing of the substances before placing them in the furnace.

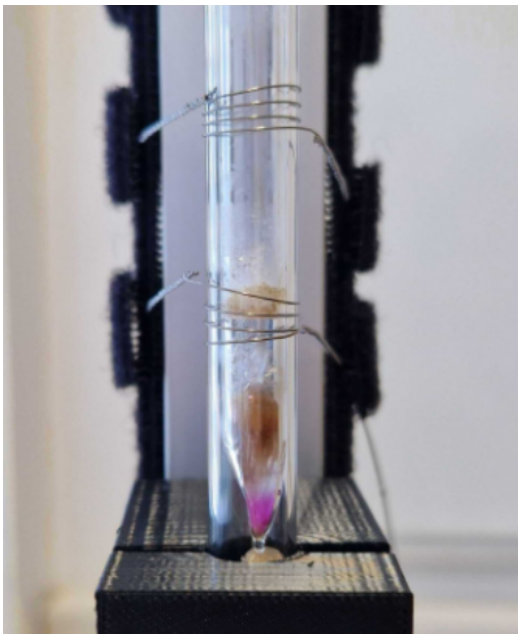

(b) dPC:dPTP crystal grown at 370 °C by mistake. Most of the material disintegrated due to high temperature.

Figure 3.23: Bridgman crystals used in the experiment.

Figure 3.24: Microscope image of the pentacene doped p-terphenyl Bridgman grown crystal.

3.5 Lock-in amplifier

In continuous-wave optically detected magnetic resonance (CW-ODMR) experiments, the measurable contrast is typically very small, often in the range of 0.1% down to 0.01% [14], [15]. Detecting such small changes in fluorescence against a large background signal is extremely challenging without advanced signal recovery techniques. For this reason, the lock-in amplifier serves as the heart of the experiment. By enabling phase-sensitive detection referenced to the applied microwave modulation, the lock-in amplifier effectively extracts the weak ODMR signal from the noise floor, making quantitative

measurements possible.
The central idea of lock-in detection is to extract the amplitude A_s and phase θ of a weak periodic signal from a noisy background. A schematic of the working principle of the lock-in amplifier is presented in Fig. 3.25.

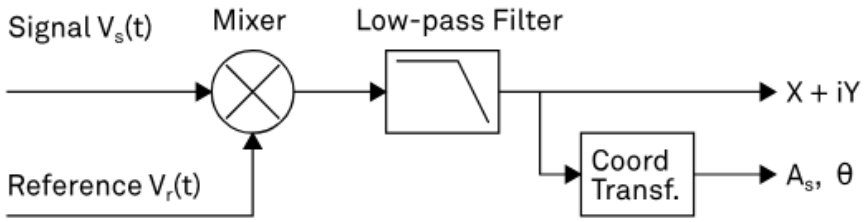

Figure 3.25: Mixing of the signal and reference and low-pass filtering performed by the lock-in amplifier [36].

Imagine an input signal of interest is of the form

$$V_s(t) = A_s \cos(\omega_s t + \theta), \tag{24}$$

with angular frequency ω_s. In practice, this signal is often followed by broadband noise that may be orders of magnitude larger than A_s. The lock-in amplifier addresses this challenge by multiplying the input with a reference signal of the form

$$V_r(t) = \sqrt{2} e^{-i\omega_r t}, \tag{25}$$

where $\omega_r = 2\pi f_r$ is the demodulation frequency. After multiplication, the result

$$V_s(t) \cdot V_r(t) = \frac{A_s}{\sqrt{2}} \cdot \left(e^{i((\omega_s - \omega_r)\cdot t + \theta)} + e^{-i((\omega_s + \omega_r)\cdot t + \theta)} \right) \tag{26}$$

contains two components: a slowly varying term at the frequency difference $\omega_s - \omega_r$ and a rapidly oscillating term at $\omega_s + \omega_r$. A low-pass filter then removes the high-frequency component, leaving only the slow component. When the signal frequency is matched to the reference frequency by modulating the microwave radiation with the reference frequency, the output becomes a DC signal proportional to the amplitude A_s, with a phase shift directly related to θ. The result after the low-pass filter is the demodulated signal

$$X + iY = \langle V_s(t) \cdot V_r(t) \rangle \approx F(\omega_s - \omega_r) \frac{A_s}{\sqrt{2}} \cdot e^{i((\omega_s - \omega_r)\cdot t + \theta)}, \tag{27}$$

where $F(\omega_s - \omega_r)$ is the frequency response of the filter at $\omega_s - \omega_r$. X and Y are called in-phase and quadrature components. The transformation of X and Y into the amplitude $R = \frac{A_s}{\sqrt{2}}$ and phase $\theta = \arctan\left(\frac{Y}{X}\right)$ information of $V_s(t)$ can be performed with trigonometric operations. This approach is the foundation of lock-in amplifiers and explains how extremely weak signals can be reliably detected [36]. The signal bandwidth is quantified by the cut-off frequency. It is the frequency at which the transfer function of a system shows 3 dB attenuation relative to DC that means, the signal power at f_{Bw} is half the power at DC. The performance of a lock-in amplifier is strongly determined by its filter design. The

low-pass filter suppresses the unwanted high-frequency components and defines the effective bandwidth of the measurement. In the digital MFLI, these filters are implemented as discrete-time infinite impulse response (IIR) filters, often modeled after RC low-pass circuits. The bandwidth parameter (cut-off frequency) is directly linked to the filter's time constant via this equation

$$\tau_n = \frac{\mathrm{FS}_n}{2\pi f_{\mathrm{BW}}}, \tag{28}$$

where FS_n is a factor that depends on the filter slope and its order. This means that a shorter time constant provides faster response but less noise rejection, while a longer one offers stronger averaging at the cost of slower dynamics. The low-pass filters after the demodulator cause a delay to measured signals depending on the filter order and time constant τ_n. After a change in the signal, it takes some time before the lock-in output reaches the correct measurement value. This is depicted in Fig. 3.26 where the response of cascaded filters to a step input signal is shown [36]. Thus, bandwidth and measurement stability must be carefully balanced according to the measurement.

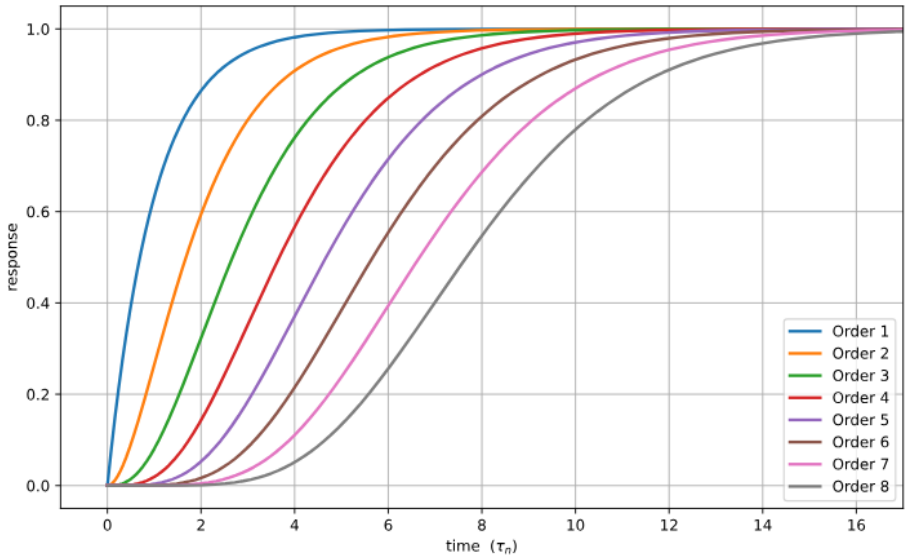

Figure 3.26: Time-domain step response of the demodulator low-pass filter for orders from 1 to 8 [36].

The settings for the bandwidth and filter order are variable for different crystals. But, the measuring time is kept constant at 0.15 s per frequency step, averaging 8000 data points into one for the ODMR spectrum.

4 Experimental setup

In this chapter, the experimental setup is introduced. It is shown in Fig. 4.1. The setup was mainly used for confocal microscopy and laser-evaporated crystals. Several modifications have accrued during this work. In this section, the optical setup, the detection box, and the microwave setup are introduced. Afterward, the step-by-step experimental procedure with the wire antenna and with the omega antenna is presented.

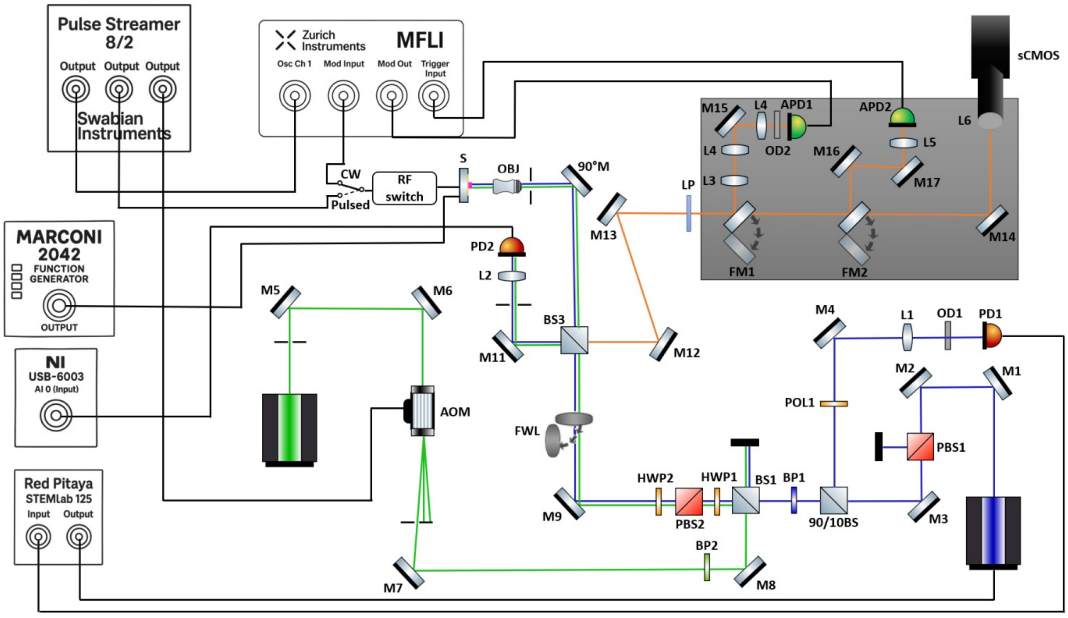

Figure 4.1: A schematic of the ODMR experiment.

There are two lasers in the setup: Omicron LuxX+ 425 nm laser with 120 mW maximum optical power and Edmund 532 nm Fiber-Coupled Laser with 200 mW maximum optical power. The blue 425 nm laser is intended to be used for PR:AC and PTCDA:AC crystals, and the green 532 nm laser for PC:PTP. The beam height on the table is 10 cm. The optical components need to be dust-free, scratch-free, and cleaned when dust is sighted.

On the blue laser branch, the mirror M1 (Thorlabs BB1-E02), after the laser, reflects the light to M2. The mirror mounts have 2 degrees of freedom, shown in Fig. 4.2, to rotate the mirror horizontally and vertically. After M2, a polarizing beamsplitter PBS1 is placed to only let vertically polarized light in the setup. The beam is then aligned with the help of the mirrors M2 and M3 by “beam walking”. Beam walking is a technique that uses two mirrors and a beam height ruler (Thorlabs BHM3 - 6") to align the beam on a straight line. The technique is presented and explained in Fig. 4.3.

To stabilize the laser intensity, a digital PID loop using the Red Pitaya STEMlab 125-14 is implemented. For this reason, the laser power needs to be read out. That is why a 90/10 beam sampler, 90/10BS, is placed in the beam path transmitting 90% and reflecting 10% of the light. The reflected beam goes through polarizer POL1 that acts as a set level for the PID loop. After that, the beam is reflected with M4 on an optical Density filter (OD = 1.5) to decrease the optical power measured on the photodiode. In front of the photodiode, there is a lens with $f = 50\,\text{mm}$ to increase the collection efficiency at the photodiode. The signal of the photodiode is fed into the Red Pitaya input. The laser intensity locking is discussed in section 4.1.1.

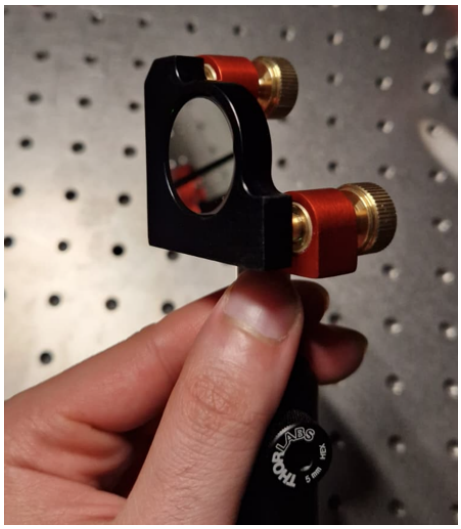

Figure 4.2: The mirror mount from Radiant Dyes MDI-2-3030z with 2 knobs to adjust horizontal and vertical tilt of the mirror.

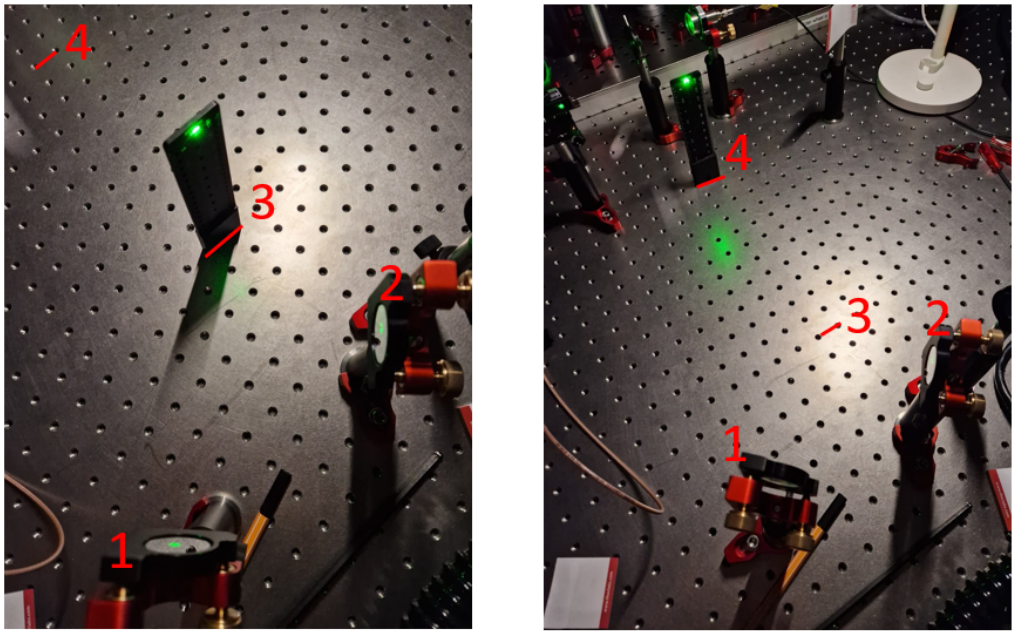

(a) (b)

Figure 4.3: Beam walking to align the beam consists of 2 repeated steps. First one is when the beam height ruler is placed on position 3 (a) and mirror number 1 is adjusted such that the beam crosses the middle hole at the correct height of 10 cm. The second step is when beam height ruler is placed on position 4 (b) and mirror number 2 is adjusted. These steps are repeated until the beam converges to a straight line, which does not require any further adjustment.

The transmitted part of the beam sampler gets filtered with the band-pass filter 425-20 nm to be sure that correct excitation is occurring. At the 50/50 beamsplitter, the reflected filtered beam is blocked, and the

optical power and polarization of transmitted beam is then adjusted with a $\lambda/2$-plate, PBS, $\lambda/2$-plate. A $\lambda/2$-plate rotates the polarization of the beam. A combination of $\lambda/2$-plate and PBS works as a tunable power attenuator, $\lambda/2$-plate afterward is to rotate the polarization after the attenuation to maximize the fluorescence. After that, the beam is reflected at M9 onto a wide-field lens $f = 150$ mm on a flip mount. The purpose of this lens is to provide a larger illuminated field of view at the sample. Then the beam is split again at BS3. While the reflected part is focused by a lens with focal length $f = 50$ mm onto a sensitive photodiode with tunable gain to monitor the incident power on the sample, the transmitted part is redirected by a 45° tilted mirror, making it perpendicular to the optical table. This perpendicular beam passes through a pinhole and then enters a 10x Olympus Plan Achromat Objective with a working distance of 10.6 mm. The objective focuses the beam onto the sample, thereby inducing fluorescence. The sample is mounted on a x- and y-axis translation stage to move the sample to a desired position. The 10x objective is mounted on a z-axis translation to move the focus plane. The emitted fluorescence propagates back along the same optical path as the excitation beam until it is reflected at BS3 towards mirror M12. Mirrors M12 and M13 then steer the signal into a long pass filter, and then into the detection box. The long pass filter allows only waves to pass through that are larger than the threshold wavelength of the filter (460 for PR:AC, 550 for PC:PTP). The fluorescence is originating from a point source, resulting in a slowly diverging beam. That is why M12 and M13 have a 2 inch diameter to collect as much light as possible.

The detection box is made out of aluminum posts holding black hardboard (Thorlabs TB4). A hole is cut for the image. In the detection box, there are two flip mirrors. After the first mirror, the beam goes through a convex lens $f = 200$ mm and a concave lens $f = -100$ mm, shrinking it by a factor of 2. The shrunk beam is focused with a $f = 50$ mm lens onto an avalanche photodiode (Thorlabs APD410A2/M). APDs are very sensitive, for that reason, an OD= 1 filter is placed before the APD. After the second flip mirror, the beam is steered with M16 and M17 onto a $f = 50$ mm lens and another APD (FEMTO PWPR-2K-SI). The main difference between APD1 and APD2 lies in their bandwidth and sensitivity. APD1 has a bandwidth of 10 MHz, making it significantly faster, whereas the Femto APD offers a bandwidth of only 2 kHz, resulting in higher sensitivity but substantially slower response. The Femto APD is utilized for the search of CW ODMR, and the Thorlabs APD will be used for pulsed ODMR. When flip mirrors FM1 and FM2 are flipped down, the fluorescence is directed to the scientific complementary metal-oxide-semiconductor (sCMOS) camera, which displays the image on the PC.

The green laser branch does not differ much from the blue side. However, the beam width is too big, thus an iris is placed in the laser path. To pulse the budget Edmund laser, an acousto-optical modulator (G&H Photonics AOM 3080-125) is employed. The AOM works by sending an acoustic wave through a Tellurdioxid crystal, creating a periodic change in the refractive index (a moving diffraction grating). When a laser beam passes through, it gets diffracted, and the angle and intensity of the diffracted light depend on the frequency and power of the acoustic wave. By changing the radio-frequency (RF) drive signal, the AOM can rapidly control the beam's intensity and diffraction angle. The first order diffraction is aligned to the setup after filtering the laser beam with a 532-10 nm band-pass filter. At BS1, the beam is reflected to $\lambda/2$-plate, PBS, $\lambda/2$-plate, and then to the sample as in the blue laser light, and the transmitted light is blocked.

The signal read out from the photodiodes is processed with various devices. As mentioned above, PD1 is connected to the Red Pitaya to stabilize the intensity of the 425 nm laser. The Red Pitaya STEMlab 125-14 is a compact FPGA- and ARM-based measurement platform that provides fast analog I/O, digital I/O, and open-source software for lab instrumentation. It can be programmed to implement a digital PID controller by reading sensor signals through its ADCs, computing the control law in real time on the FPGA/CPU, and driving actuators via its DAC outputs [37]. PD2 is connected to a Data acquisition

system, NIDAQ USB 6003. The NI USB-6003 can read a photodiode by measuring the voltage across a transimpedance amplifier (or load resistor) connected to the diode with its 16-bit and 100 kS/s analog input channels [38]. The sampled signal is digitized and streamed to the PC via USB, where a software written in Python processes the intensity data in real time. The 2048 data points are averaged into one every 0.1 s and then plotted next to the ODMR spectrum to see if the laser fluctuations induced the observed signal. The MFLI 500 kHz Lock-in Amplifier from Zurich Instrument, introduced in section 3.5, is used to measure the faint ODMR signal with APD2 in cw mode. The APD1, with the larger bandwidth, is used in pulsed ODMR and is connected to the MFLI and operated in oscilloscope mode. The Scientific Complementary Metal-Oxide-Semiconductor (SCMOS) camera uses a pixelated CMOS sensor with parallel readout electronics, allowing for high frame rates, low noise, and wide dynamic range. Each pixel has its own amplifier, which reduces readout noise and enables sensitive imaging even under low-light conditions [39]. The Pulse Streamer 8/2 from Swabian Instruments is a versatile digital pulse generator designed to create precise, user-defined pulse sequences. It features 8 digital and 2 analog output channels, with nanosecond timing resolution and low jitter for accurate synchronization in experiments. The device works by streaming preprogrammed sequences from its memory or control software. It is used to trigger the AOM to generate the green laser pulses, to trigger the microwave switch for pulsed ODMR measurement, and to trigger the MFLI for readout. Later, it is also used to gate a digital APD.

4.1 Experimental procedure

In this section, a step-by-step guide is introduced for running the ODMR experiment for perylene doped anthracene (PR:AC) and PTCDA doped anthracene (PTCDA:AC) crystals and pentacene doped p-terphenyl (PC:PTP) crystals. The excitation of the PR:AC and PTCDA:AC crystals occurs at 425 nm, and for the PC:PTP crystals at 532 nm. The Sample is first purified and grown, and then it is mounted in the setup. Afterward, the beam alignment is checked before starting the experiment. The microwave generator and amplifier are turned on, and then the microwave signal before the antenna is connected to an oscilloscope to verify if the generated waves are as expected, see Fig. 4.4. Depending on the

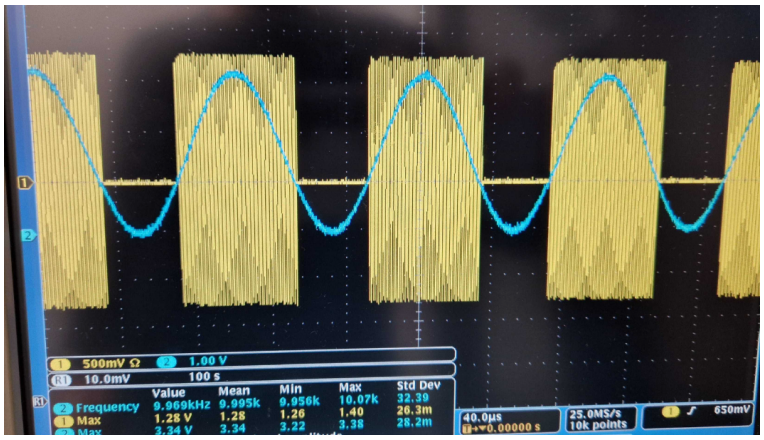

Figure 4.4: An oscilloscope image of the microwave signal after the antenna before termination. Yellow is the microwave signal with a frequency of 100 MHz and blue is the trigger of the switch with a frequency of 117 Hz coming from the lock-in amplifier.

sample, the 532 nm laser or the 425 nm laser is brought to lase. Afterwards, the sCMOS camera is turned on to check the laser focus on the sample. If adjustments to the focus are needed, the objective is

moved via the z-axis translation stage. The sample is mounted on a 2-axis linear translation stage, thus it is moved along the x and y axis to find the brightest spot on the sample. After that, the frequency sweep is prepared. There are two methods to run the sweep. The first is to use the frequency sweep functionality in the microwave generator. A full spectrum can be swept in 10 seconds with 1000 steps and 10 ms waiting time per frequency step. But, the lock-in amplifier requires 150 ms for each frequency step. Thus, the second method is used, where the frequency is sent via serial communication between the computer and microwave generator. The sweep is then a *for*-loop of the desired frequency array. The serial communication is of the order of 10 ms which does not slow down the sweeping process by much.

4.1.1 PR:AC and PTCDA:AC crystals

The blue 425 nm Omicron LuxX+ laser is used for the PR:AC crystals PTCDA:AC. The laser has a fast modulation frequency, which allows for modulating the optical intensity efficiently. Thus, the photodiode PD1 in Fig. 4.1 is connected to the Red Pitaya, where the PID loop software is initialized. The intensity locking software is called Linien. The Program sweeps the modulation voltage to find the zero crossing. After that, the P-, I-, and D-values are set, and at the end the zero crossing is selected to lock. However, it is not that simple. The program often failed to find the zero crossing, and even after that, the smallest change in the environment caused the lock to fail and the lock quality to be poor. The quality of the intensity locking is characterized by the ratio between the standard deviation (std) to the mean of the distribution of the averaged photodiode signal. The distribution is assumed to be Gaussian, see Fig. 4.5. Fine-tuning the PID parameters increases the quality, however, the quality with lock never exceeds

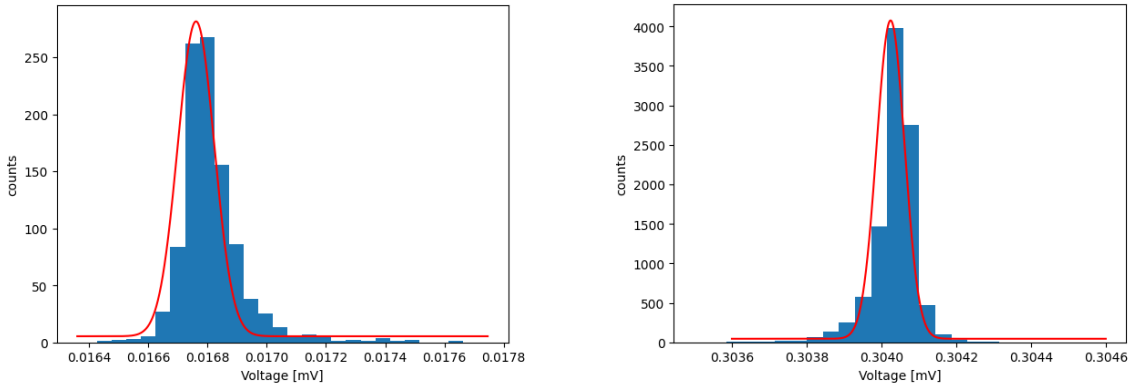

(a) std/mean = 0.67% with lock parameters: $P = 5000$, $I = 100$, $D = 0$.

(b) std/mean = 0.02% Without lock

Figure 4.5: A histogram of the distribution of the averaged laser intensity with the monitoring photodiode PD2 collected by the NIDAQ. The measurement took 30 minutes.

the one without. Thus for this work, the Red Pitaya will be discarded. The other way to determine the goodness of the lock is by applying a fast Fourier transformation (FFT) to the signal to transform it into the frequency domain. There, the noise spectrum can be analyzed. But, this method is not applied in this setup because the sampling rate after the averaging is 10 samples/s, leading to a limited range up to 10 Hz in the frequency domain. The fact that the laser intensity cannot be locked with the Red Pitaya is not limiting the experiment, because the MFLI lock-in amplifier cancels out all of the noise induced by the laser.

For PR:AC crystals the resonant frequencies are estimated to be 1.56 GHz, 1.72 GHz and 3.2 GHz. The

first signal at 1.56 GHz is calculated to be the largest. Thus, the sweep is around this frequency.
For PTCDA:AC crystals the resonant frequencies are $f(T_x \leftrightarrow T_y) = 0.25\,\text{GHz}$, $f(T_y \leftrightarrow T_z) = 1.25\,\text{GHz}$ and $f(T_x \leftrightarrow T_z) = 1.5\,\text{GHz}$ [40]. The strongest signal observed in other experiment is at the $f(T_y \leftrightarrow T_z)$ frequency.

4.1.2 Pentacene doped p-terphenyl crystals

The green 532 nm laser is switched on. The AOM, triggered by the pulse streamer, is turned on. As mentioned above, the first order diffraction is aligned to the experiment. The diffraction efficiency is adjusted by rotating the AOM holder around the z-axis and the x-axis while measuring the optical power of only the first order diffraction. The maximum diffraction efficiency achieved is 40% for the first order. The transition frequencies of PC:PTP are found in Eq. 6. The largest signal is expected to be at the transition $f(T_x \leftrightarrow T_z) = 1.45\,\text{GHz}$.

5 Results and discussion

In this section, the experimental results are presented. The results are discussed and analyzed. The structure of this section follows the temporal order of the measurement. In the beginning, perylene doped anthracene (PR:AC) crystals are studied. After that, the measurements on pentacene doped p-terphenyl (PC:PTP) and deuterated pentacene doped deuterated p-terphenyl (dPC:dPTP) are presented.
The ODMR contrast for measurements with the lock-in amplifier is defined as the

$$\text{contrast} = \frac{\text{demodulated signal} \cdot \sqrt{2}}{\text{PD signal}} \cdot 100\%. \tag{29}$$

The $\sqrt{2}$ in Eq. 29 originates from the lock-in amplifier demodulated signal's amplitude. see Eq. 27. For the measurement with only APD, the contrast is defined as

$$\text{contrast} = \frac{\text{signal off resonance - signal on resonance}}{\text{signal off resonance}} \cdot 100\%. \tag{30}$$

5.1 PR:AC

The measurement begins with an emission spectrum to verify that the sample examined is perylene. The spectrum, shown in Fig. 5.1, is taken with the spectrometer. The emission spectrum at cryogenic

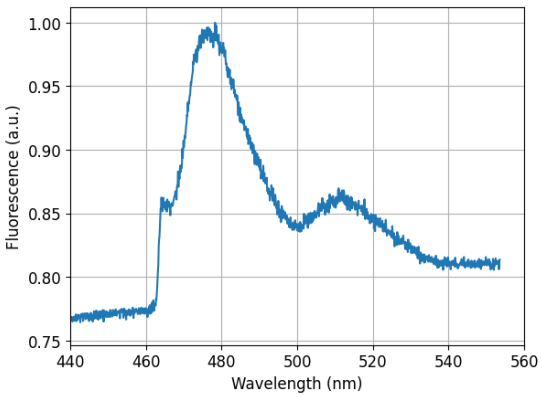

(a) The emission spectrum of PR:AC with 0.1% concentration at room temperature with 460 nm LP filter.

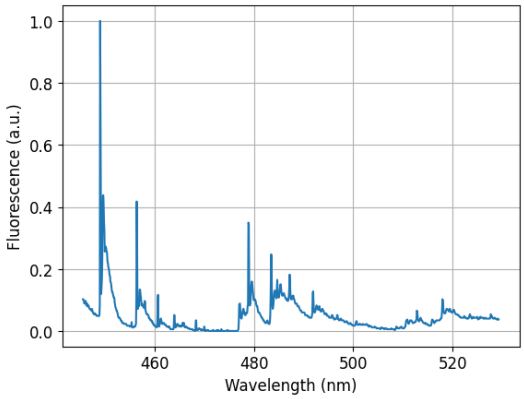

(b) The emission spectrum of PR:AC with 0.01% concentration in 4 K [20].

Figure 5.1: The perylene emission spectrum taken with the spectrometer at room temperature and in 4 K cryogenic temperature.

temperatures shows more details than the measurement at room temperature. At room temperature, many vibrational and rotational states are populated, and collisions along with Doppler effects broaden the spectral lines, making fine details difficult to resolve. In a cryostat, molecules mostly occupy their ground state, reducing the number of possible transitions. With less motion and fewer phonon interactions, the spectrum shows sharper lines and more detailed structure [41]. The highest line in the spectrum is the 0-0 Zero-Phonon-line (ZPL). The phonon wing next to the ZPL is observed as well. Additional lines such as 0-1, 0-2, etc. with their phonon wing can be observed as well, further information on this topic can be found in the reference [20]. All of those lines are enveloped at room temperature.
Then, the ODMR measurement is prepared. The microwave radiation is delivered via wire antenna or an omega antenna.

5.1.1 Wire antenna without lock-in amplifier

The integration of the wire antenna is done by tying the BNC cable and the wire antenna to a 50 mm Thorlabs post (TR50/M). The Thorlabs post is then connected to another 50 mm Thorlabs post via a 90° post clamp (RA90). The holding post is then screwed to a z-axis translation stage, as shown in Fig. 5.2. The advantage of this construction is that the position of the antenna is adjustable by rotating the posts and by moving the translation stage.
After turning on the microwave to -8 dBm, the microwave frequency is swept while recording the

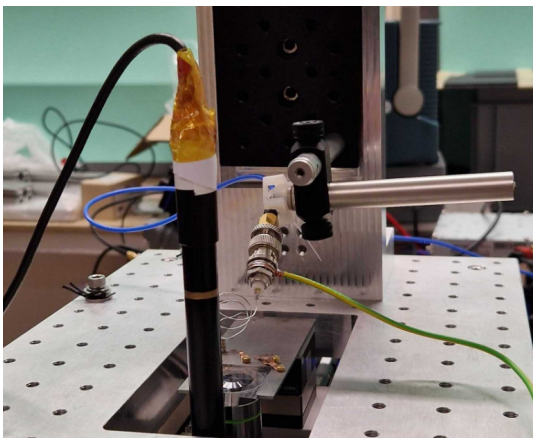

Figure 5.2: The wire antenna is held by the post-clamp-post structure. The antenna is grounded separately to a radiator (earth ground). The sample is directly beneath the wire antenna. The black tube is the motor for the z-axis translation stage that moves the 10x objective to adjust the focus.

fluorescence intensity with the Thorlabs APD that is connected to an oscilloscope. On the first run where the frequency is swept continuously between 1.4 GHz and 1.6 GHz, a periodical signal is observed, as shown in Fig. 5.3. The contrast is 80%, which is much higher than expected for a room temperature ODMR experiment under continuous wave conditions. This hints that the signal is not originating from the microwave transition in the triplet state. The measurement is taken again. However, the laser power and the microwave power are increased to magnify the effect. The microwave frequency sweep is between 1400 MHz and 1800 MHz. The result is shown in Fig. 5.4. Now, the contrast is 87.5% and even larger than before. However, this effect is visible with the eye and camera, see in Fig. 5.5. Yet, a contrast of 87.5% is non-physical for such a system, meaning there is a different origin for this phenomenon. To make sure that this behavior is not coming from the laser, a Thorlabs digital power meter (PM100D) is used to read out the optical power via a photodiode. The photodiode is placed on the optical path near the sample. The power meter is connected to the PC, and the data is saved in a txt-file and plotted in Fig. 5.6. There is an obvious correlation between the laser power and the frequency. The laser head and driver are very close to the antenna that is radiating at

$$-8\,\text{dBm (setting on Marconi)} + 52\,\text{dB (ampilifer)} = 44\,\text{dBm} \equiv 16\,\text{W}. \tag{31}$$

Due to the geometry of the antenna, the radiation is not entirely focused on the sample, but rather radiated elliptically in space. The radiation could have interfered with the laser driver and caused this effect. To counteract the problem, the laser is brought far away from the antenna to a different room, and is fiber coupled to the setup. Thus, the antenna can not interact with the laser's electronics. The ODMR measurement is redone with a larger continuous frequency sweep starting from 1300 MHz to 1800 MHz

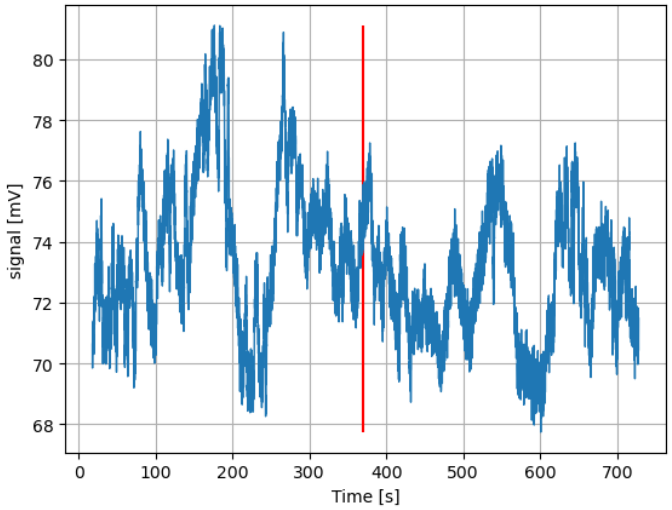

Figure 5.3: ODMR attempt with a continuous frequency sweep starting at 1.4 GHz and ends at 1.6 GHz. The plot is extracted from the oscilloscope. The red line marks the repetition of the frequency sweep.

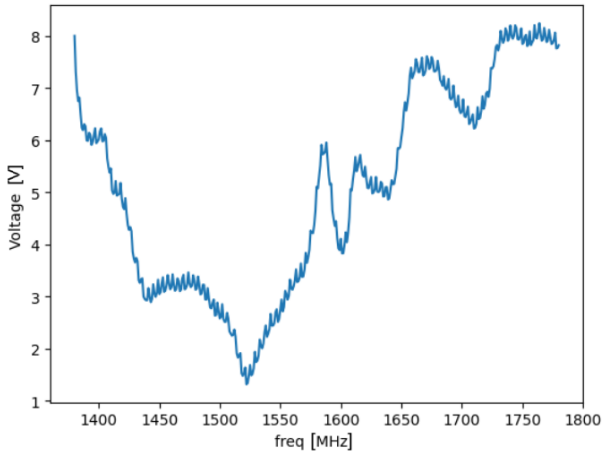

Figure 5.4: ODMR attempt with frequency scan between 1400 MHz and 1800 MHz.

and with the fiber-coupled beam. The data is presented in Fig. 5.7. Even after using a faraway laser, the periodic signal still occurred. This means that the antenna is interfering with other electronic devices at specific frequencies. After further examination, the source of the problem is located. The radiated microwave is cross-talking with the translation stage controller, causing an error on display "high voltage", which leads to a tiny movement of the translation stage in all directions. These small changes in the excitation spots results in a big contrast in the fluorescence. When the microwave is turned off and the controller is restarted, the error is fixed and does not take place again until the microwave is turned on again. Thus, the translation stage is turned off during the measurement to ensure that the sample stays still. When the experiment is repeated, with the controller off, the data extracted does not show any periodicity anymore, and yet still a high contrast, see in Fig. 5.8. This is because a high microwave field is radiated out of the antenna, and inside of the translation stages, there is a motor with coils. The microwave field induces small currents that move the translation stage, leading to a bigger contrast.

This is the main setback of the wire antenna. It radiates in all direction without effectively focusing the

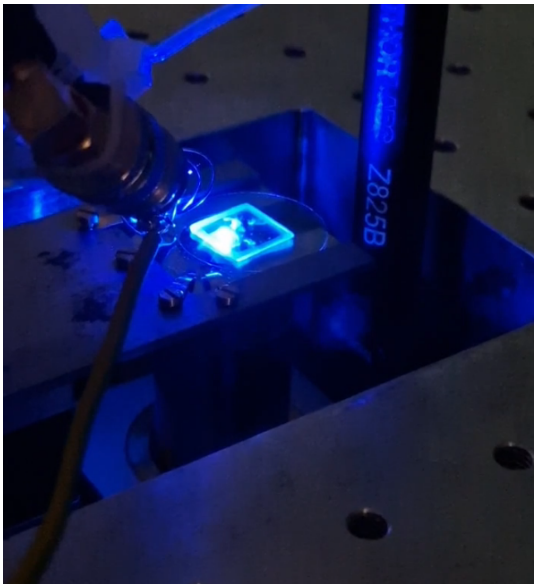

(a) Off resonance at 1700 MHz (brighter).

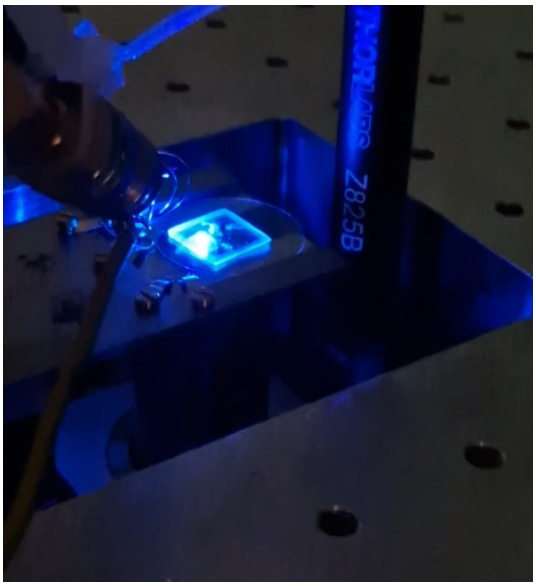

(b) On resonance at 1525 MHz (darker).

Figure 5.5: Images of the intensity of the fluorescence changing depending on the microwave frequency

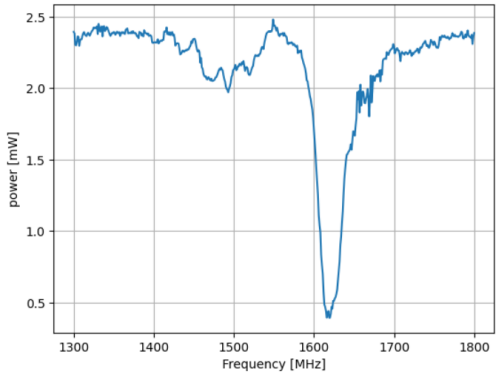

(a) With low optical power

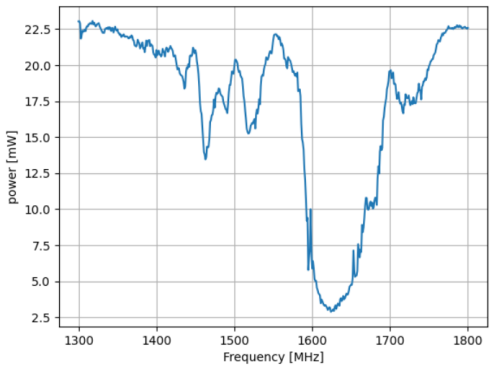

(b) With high optical power.

Figure 5.6: The measurement of the laser power change depending on the microwave frequency.

microwave on the sample. Thus, a new approach is needed. The wire antenna is replaced with an Omega shaped antenna.

5.1.2 Omega antenna and Lock-in amplifier

The omega antenna improves the microwave power delivery and offers a very broad bandwidth to scan for resonances. The system of perylene doped anthracene is not studied at room temperature and is more complicated than others as Pentacene doped p-Terphenyl because the triplet state energy level of anthracene lies between the S_0 and S_1 of perylene and higher than the triplet state energy level of perylene. The theory suggests that when exciting the perylene molecules, an intermolecular ISC occurs from perylene's S_1 to anthracene's T_1, and then anthracene's T_1 decays to perylene's T_1. This results

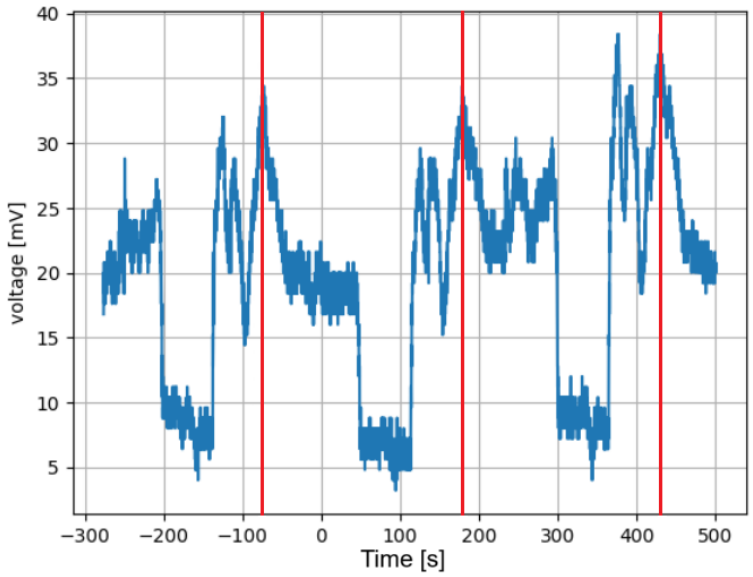

Figure 5.7: ODMR attempt with a fiber-coupled beam with a frequency scan between 1300 MHz and 1800 MHz. The red lines mark the beginning of each frequency sweep.

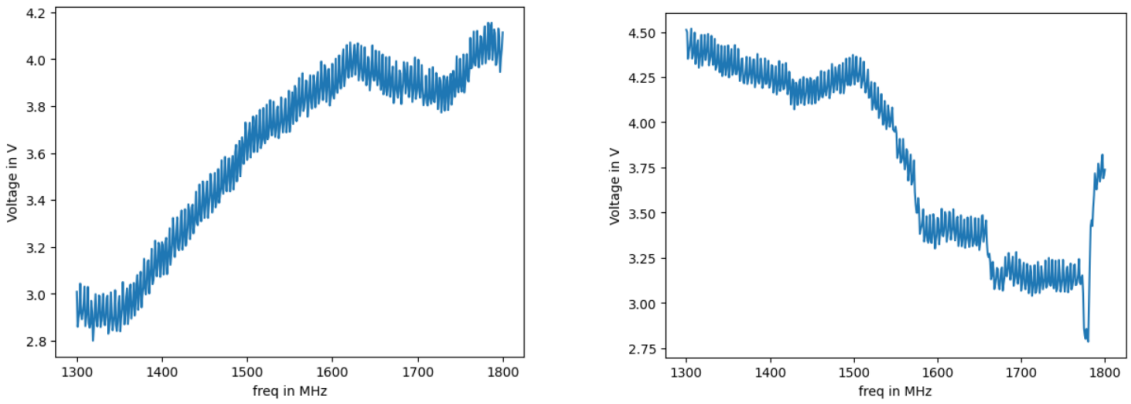

(a) Run 1.

(b) Run 2.

Figure 5.8: ODMR measurement with fiber-coupled beam and switched-off controller.

in much more complex dynamic of the system. The theory can be proven by measuring more than 3 resonances, accounting for the anthracene's and perylene's triplet states. When scanning over the whole spectrum for a PR:AC 1:10000 sample, a couple of reproducible peaks are observed. The data is shown in Fig. 5.9. The resonances are found at 885 MHz, 894.2 MHz, 1133.2 MHz, 1150.3 MHz, 1183.2 MHz, and 1221.6 MHz. All of the resonances change in the vicinity of a magnetic field. However, near the magnetic field, the transition frequency must be shifted due to Zeeman effect [13]. The effect observed is a decrease in intensity only, not a shift.

This is far more complex than anticipated, a further study on this sample will be done after benchmarking the whole setup with a known crystal: Pentacene doped p-Terphenyl (PC:PTP).

With this sample, temperature sensitive fluorescence device has been made by coincidence. Further

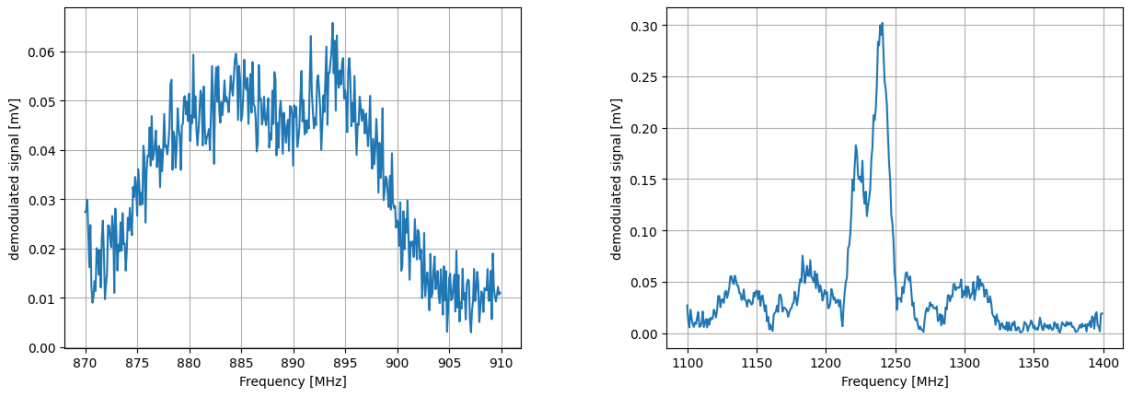

(a) (b)

Figure 5.9: The peaks observed for PR:AC (1:10000 dopant concentration) sample.

information can be found in Chapter App. III.

5.2 Pentacene doped p-terphenyl (PC:PTP) Bridgman Crystal

ODMR with PC:PTP has been demonstrated by 2 independent groups [14], [15]. They demonstrated CW and pulsed ODMR in ambient conditions. Their approach is repeated to benchmark and adjust the experiment to measure ODMR.
After placing the sample in the setup, setting the microwave power to -10 dBm (1 W after amplification) and optical power on the laser to 360 μW, the first signals are observed. The data is shown in Fig. 5.10. It is repeatable and reproducible. The peak is found at 1449.4 MHz. However, the data is very noise.

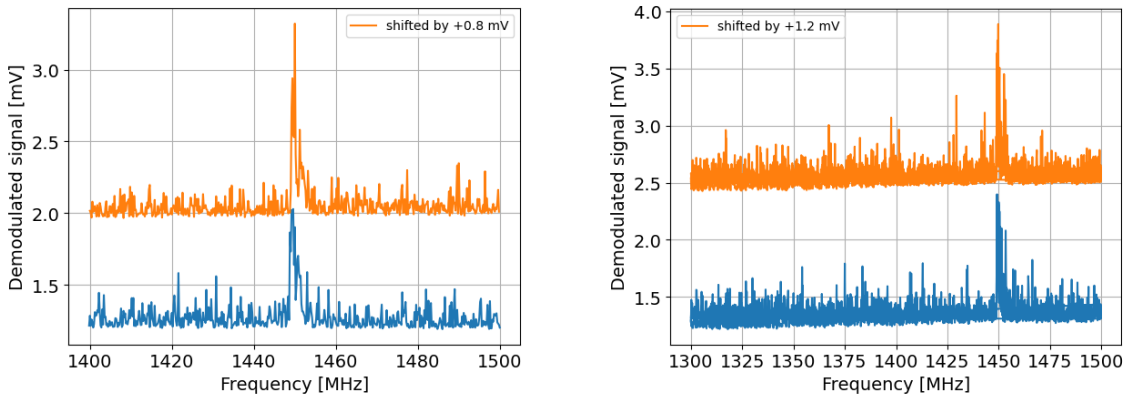

(a) The first 2 runs yielding a peak at 1450 MHz.

(b) 3rd and 4th run, scanning the frequency in a wider range to see the 1343 and 1450 MHz resonance.

Figure 5.10: The first time measuring with the PC:PTP crystal yields ODMR spectrum. The 1343 MHz is not visible yet.

The MFLI lock-in amplifier settings

$$\text{modulation frequency: } f_{\text{mod}} = 117\,\text{Hz}, \quad \text{frequency bandwidth: } f_{\text{3dB}} = 5\,\text{Hz} \tag{32}$$

are now adjusted to maximize the signal-to-noise ratio (SNR). The changes to the lock-in amplifier are applied to the frequency bandwidth and filter order. The filter order is increased from 3 to 4 to empower the noise damping. The frequency bandwidth is chosen to be 1 Hz to balance between measurement speed and noise. The result of the new setting is shown in Fig. 5.11. The ODMR contrast is measured to be 0.01%. The measured Full Width at Half Maximum (FWHM) is 2 MHz. To verify that the peak is

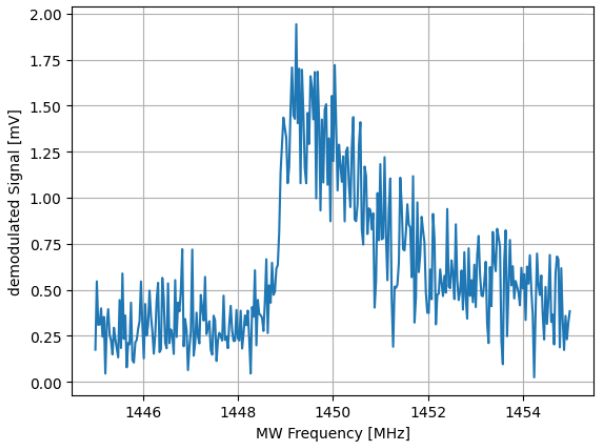

Figure 5.11: The $|T_x\rangle \leftrightarrow |T_z\rangle$ resonance of the PC:PTP crystal. The ODMR contrast is 0.01%.

a result of the magnetic resonance, a magnet is moved near the sample while the microwave frequency is on resonance. When recording the demodulated signal, it is observed that when the magnet is close to the sample, the resonance shifts and the signal goes to zero. While moving the magnet away, the signal gains in amplitude again. This shows that the linear Zeeman effect is taking place, resulting in the shift of the resonance. The last step to verify that the signal is real is to measure other resonances, for example, at 1344 MHz and 106.5 MHz. The $|T_x\rangle \leftrightarrow \left|T_y\right\rangle$ transition is not possible to address in the current setup because the microwave amplifier only works for frequencies larger than 700 MHz. By decreasing the frequency bandwidth to 0.1 Hz, the noise can be reduced even further to resolve the weakest transition $\left(\left|T_y\right\rangle \leftrightarrow |T_z\rangle\right)$. At the same time, the time constant increases $\tau_4 = 0.69$ s. This means that for each frequency step requires 4.5 s to measure 90% of the signal, as indicated by the Fig. 3.26. When scanning around 1343 MHz, the weak resonance is found, see Fig. 5.12. The measured FWHM is 1.5 MHz. This is more than enough evidence to prove that ODMR for pentacene doped p-terphenyl is found.

The microwave saturation profile is examined by setting the microwave frequency on resonance with the $|T_x\rangle \leftrightarrow |T_z\rangle$ transition at 1449.4 MHz and then by sweeping the microwave power. This would result in driving the transition faster and the population to equalize, and then no further increase is expected. The data is shown in Fig. 5.13. The data is fitted to the function

$$C(x) = C_{\max}\frac{P/P_S}{1+P/P_S} \equiv \frac{a\cdot x}{1+b\cdot x}, \tag{33}$$

where C_max is the maximum contrast and P_S is the saturation power. This function is derived from the rate equations when looking at the saturation behavior [42]. The fit parameters are

$$a = \frac{C_{\max}}{P_S} = 0.065(1)\,\mathrm{W}^{-1}, \quad b = \frac{1}{P_S} = 0.699(24)\,\mathrm{W}^{-1} \Rightarrow P_S = 1.43(5)\,\mathrm{W}, \quad C_{\max} = 0.093(4)\%. \tag{34}$$

The error of the maximum contrast $C_{\max}$ and of the saturation power P_S are calculated with Gaussian

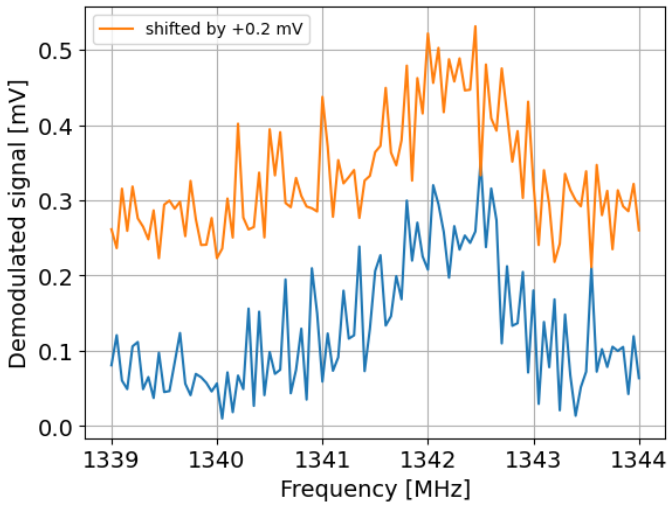

Figure 5.12: The measurement of $|T_y\rangle \leftrightarrow |T_z\rangle$ resonance done twice. The peak position is at 1342.5 MHz, matching the data from the references [14] and [15].

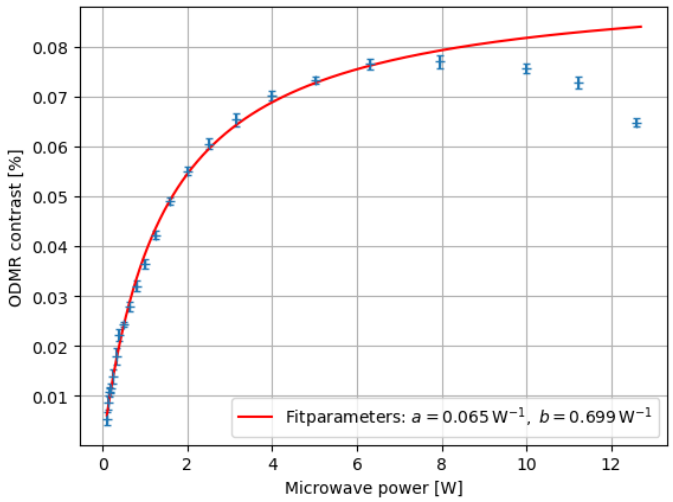

Figure 5.13: Microwave power saturation curve.

error propagation [43]

$$\Delta f(x_1, x_2, \ldots, x_N) = \sqrt{\sum_{i=1}^{N} \left(\frac{\partial f}{\partial x_i} \cdot \Delta x_i \right)^2}. \tag{35}$$

The quality of the fit is determined with χ^2/ndf and R^2-score. The R^2-score is 0.98, which means that 98% of the variance in the data is explained by the fit. The data follows the trend of the fit when the value of the R^2-score is higher than 95%. However, even visually it is observed that the fit does not describe the last 3 data points well. This is reflected in the $\chi^2/\mathrm{ndf} = 9$. The fit is considered good if $\chi^2/\mathrm{ndf} \approx 1$, and in this case it is not. The reason is that the saturation formula accounts only for saturation, while the sample is simultaneously affected by other phenomena. nothing conclusive can be drawn from the data because only 3 data points are not enough evidence. At a microwave power of 3 W, the antenna's

temperature begins to rise noticeably. Thus, heat could be one of the causes.
Other groups have worked intensively on this organic crystal. In this work, something new should be produced. previous works show the effect of deuteration on the PC:PTP sample in cryogenic temperature [13], but not at room temperature. Thus the next organic crystal examined is deuterated pentacene in deuterated p-terphenyl (dPC:dPTP).

5.3 Deuterated pentacene doped deuterated p-terphenyl (dPC:dPTP) Bridgman Crystal

This sample shows the best results, thus, more work is invested in this crystal. Not only CW ODMR but also pulsed ODMR is planned to be done.
After placing the parts that survived the furnace, a resonance is detected during a frequency scan from 1440 MHz to 1460 MHz, see Fig. 5.14. The measured FWHM is 1.3 MHz, which is about 2 time as

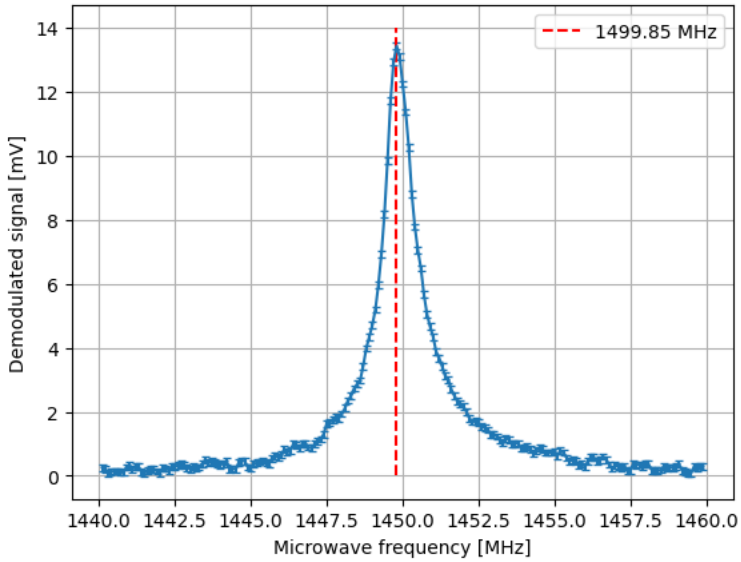

Figure 5.14: The $|T_x\rangle \leftrightarrow |T_z\rangle$ resonance is measured with 1 W microwave power and the MFLI lock-in amplifier settings: $f_{\mathrm{mod}} = 117\,\mathrm{Hz}$, $f_{3\mathrm{dB}} = 1\,\mathrm{Hz}$.

thin as the resonance for the non-deuterated sample in Fig. 5.11. The ODMR contrast is 0.25%. When scanning for the $|T_y\rangle \leftrightarrow |T_z\rangle$ resonance between 1340 MHz and 1344 MHz with the same setting in Fig. 5.14, the peak is also directly found. The data is shown in Fig 5.15.The FWHM of the $|T_y\rangle \leftrightarrow |T_z\rangle$ resonance is 400 KHz and the ODMR contrast is 0.10%. In Fig. 5.16, a comparison of the results from the deuterated and non-deuterated sample is presented. The peak height is drastically higher for the deuterated sample, not only because of the different dopant concentration and of the deuteration, but also because of the deuteration itself. The dopant concentration of PC:PTP is about 0.03%, while dPC:dPTP has 0.07%. The more dopant there is in the sample, the more light gets absorbed and emitted, leading to higher fluorescence and ODMR contrast. The deuteration of PC:PTP introduces a deuteron (^{2}H) with a proton and a neutron. Its nuclear spin has a much smaller magnetic moment (about 6.5 times smaller than a proton's). By replacing hydrogen atoms with deuterium, the strength of the hyperfine interactions is drastically reduced. The local magnetic noise from the nuclei is effectively quieted. The electron spins in the sample now experience a much more uniform magnetic environment. This leads to a significantly narrower resonance line [13]. The characteristic asymmetric wing of ODMR in a non-deuterated is lifted by deuteration. This asymmetry is caused by the hyperfine interaction, and when the deuterated sample

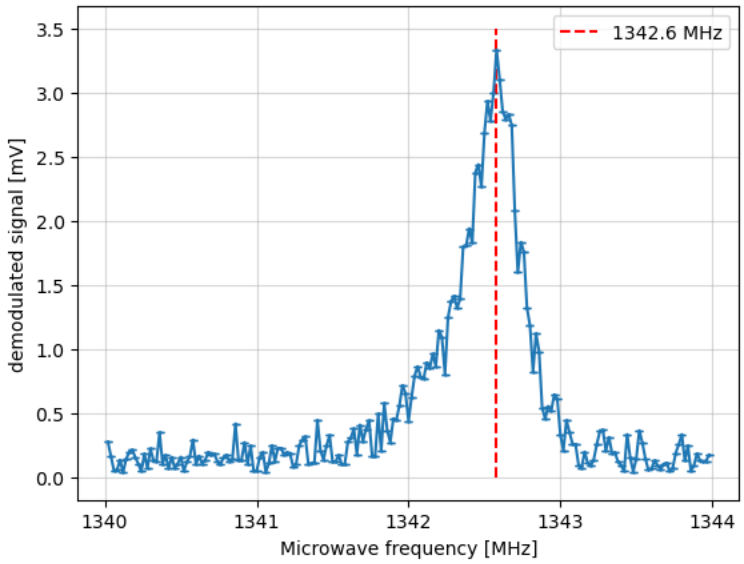

Figure 5.15: The $|T_y\rangle \leftrightarrow |T_z\rangle$ resonance is found with 1 W of microwave power and the MFLI lock-in amplifier settings: $f_{\text{mod}} = 117\,\text{Hz}$, $f_{3\text{dB}} = 1\,\text{Hz}$.

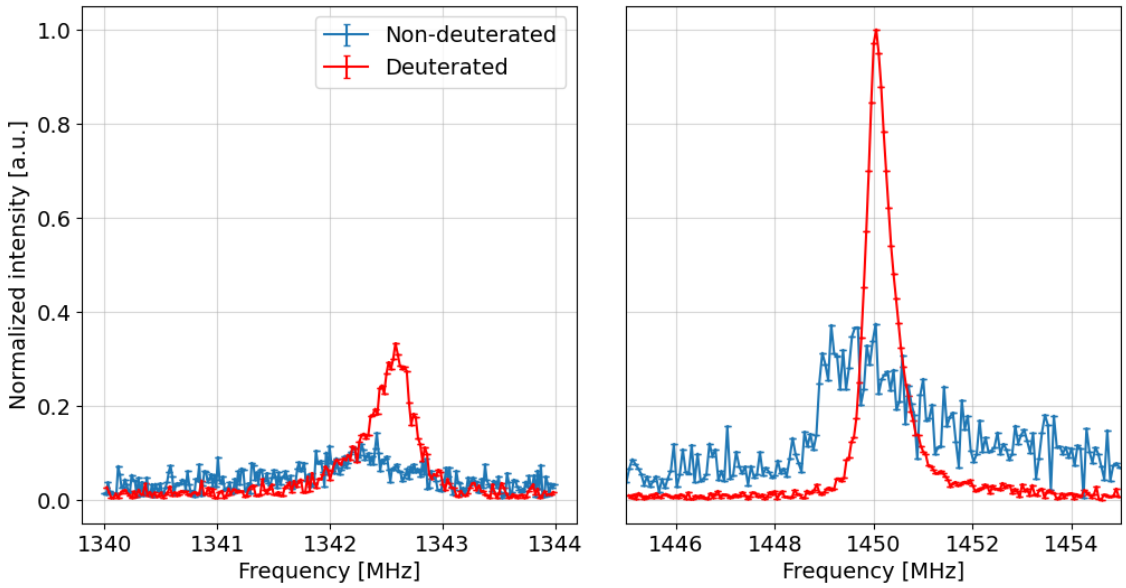

Figure 5.16: A comparison between the deuterated and non-deuterated PC:PTP samples. on the left is the $|T_y\rangle \leftrightarrow |T_z\rangle$ transition and on the right is the $|T_x\rangle \leftrightarrow |T_z\rangle$ transition. The intensity of the plots is normalized to the $|T_x\rangle \leftrightarrow |T_z\rangle$ peak of the deuterated sample.

is used, the hyperfine interaction is 6.5 times weaker, which makes the line sharper [13].
To study the effects of different parameters of the lock-in amplifier, the peak at 1449.85 MHz is examined at different reference frequency and cutoff frequency, as shown in Fig. 5.17. For lower cutoff frequency, the SNR improves. This is realistic because of the decreased bandwidth that results in a better resolution. $f_{3\text{dB}} = 1\,\text{Hz}$ is then used for further experiment, since it has a great resolution and does not effect the

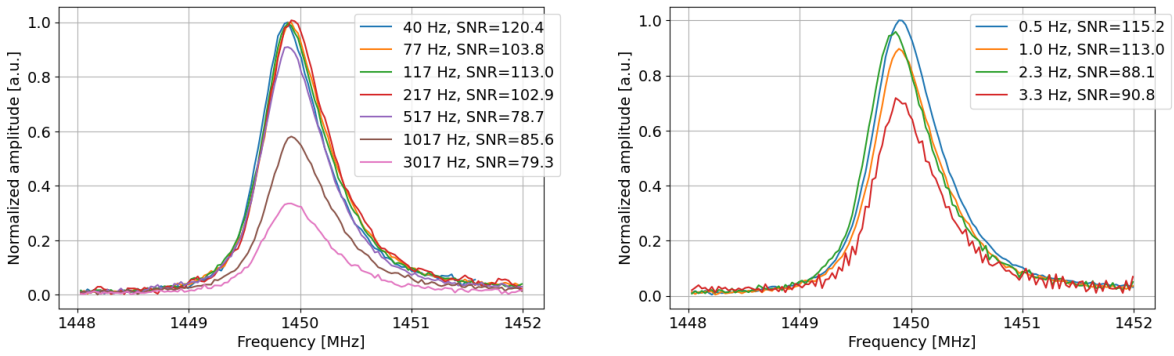

(a) $f_{3\mathrm{dB}} = 1\,\mathrm{Hz}$ and different reference frequency.

(b) $f_{\mathrm{mod}} = 117\,\mathrm{Hz}$ and different cutoff frequency.

Figure 5.17: The effect of different lock-in amplifier settings on the $|T_x\rangle \leftrightarrow |T_z\rangle$ transition peak and SNR.

speed of the measurement. For an increasing reference frequency, the SNR decreases. The noise level is decreasing, with higher reference frequency. But, the peak height is reduced. This happens mainly because of the lifetime of the triplet state T_z is 0.5 ms, and when the reference frequency is close to $(0.5\,\mathrm{ms}^{-1})^{-1} = 2000\,\mathrm{kHz}$, the spin response declines, leading to a lower ODMR contrast. $f_{\mathrm{mod}} = 117\,\mathrm{Hz}$ is chosen, however, in future experiments a lower modulation frequency can be taken.

Unlike the other samples, dPC:dPTP is not studied well enough in ambient conditions, thus, an elaborate analysis of different phenomena is done. Numerical calculations have shown that the steady state population of the triplet state depends on the optical pumping transition $|S_0\rangle \leftrightarrow |S_1\rangle$. The dependency is logical, if the optical pumping is weak, fewer pentacene molecules are pumped into the excited state, leading to fewer molecules going through the inter-system crossing into the triplet states. Thus lowering the population and their difference, resulting in lower ODMR contrast [15]. This theoretical calculation is put to the test by measuring the ODMR contrast while varying the optical intensity on the laser, see data plotted in Fig. 5.18. The data to fit a saturation curve

$$C(P) = C_{\mathrm{max}} \frac{P/P_S}{1 + P/P_S}, \tag{36}$$

yielding a maximum contrast $C_{\mathrm{max}} = 0.37(1)\,\%$ and saturation power $P_S = 3.7(1)\,\mathrm{mW}$. The behavior is exactly as expected from the theoretical calculation, showing that the steady state population of the triplet states changes with optical power until saturation.

Next, the ODMR line broadening caused by high microwave power is probed. To do this measurement, the $|T_x\rangle \leftrightarrow |T_z\rangle$ transition is studied for different microwave powers. The result is shown in Fig. 5.19. This measurement is very important, since it shows many physical effects. With rising microwave power, the power broadening is observed. There is a linear increase of amplitude for powers between -60 dBm up to -19 dBm, then the transition saturates, see in Fig. 5.20. But when the microwave power is further increased, the amplitudes start to decrease. What is even more confusing is that starting from -19 dBm, the resonance frequency starts to shift to a lower frequency. A peak splitting is also observed starting at -9 dBm. The peak splitting could be because of two different insertion sites of the p-terphenyl single crystal [15]. For a better analysis of the data, the frequency shift, FWHM, and the ODMR contrast change against the microwave power are illustrated in Fig. 5.20. From the rate equation, the saturation profile and power broadening are modeled. For the FWHM broadening, the function [42]

$$\mathrm{FWHM} = \Gamma \cdot \sqrt{\frac{P_{\mathrm{in}}}{P_{\mathrm{S}}} + 1} \tag{37}$$

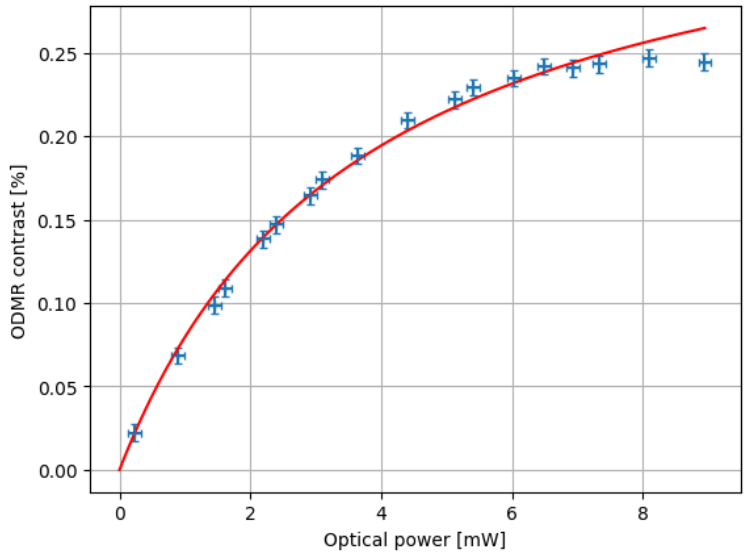

Figure 5.18: The ODMR contrast change as a function of the optical power measured directly before the 10x objective.

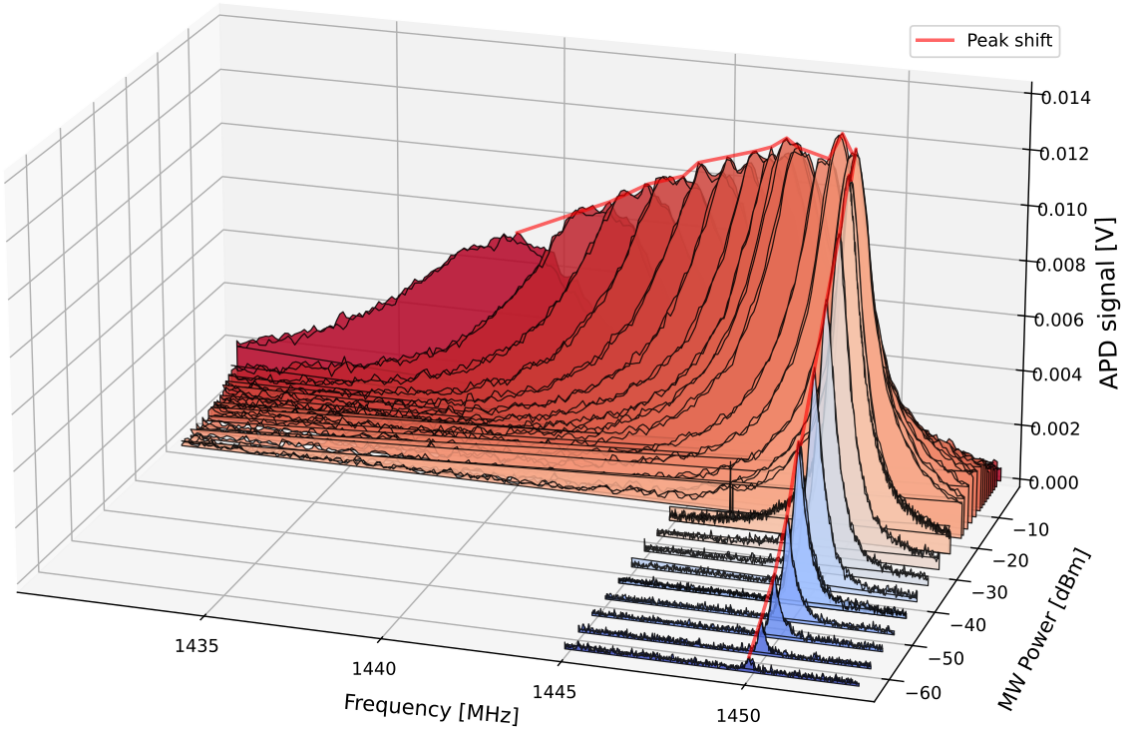

Figure 5.19: Line broadening observed on the deuterated sample spectra for different microwave powers before the 52 dB amplification. For high microwave power, the peak gets broader, weaker, and shifted.

is used. The fit is shown in Fig. 5.20. The fit parameter are $\Gamma = 0.53(10)$ MHz and $P_S = 0.12(4)$ W. The quality of the fit is quite bad. The data are not described by the fit at all. There is a strong curvature in the low power regime that the square root function can not describe. The smallest FWHM measured is

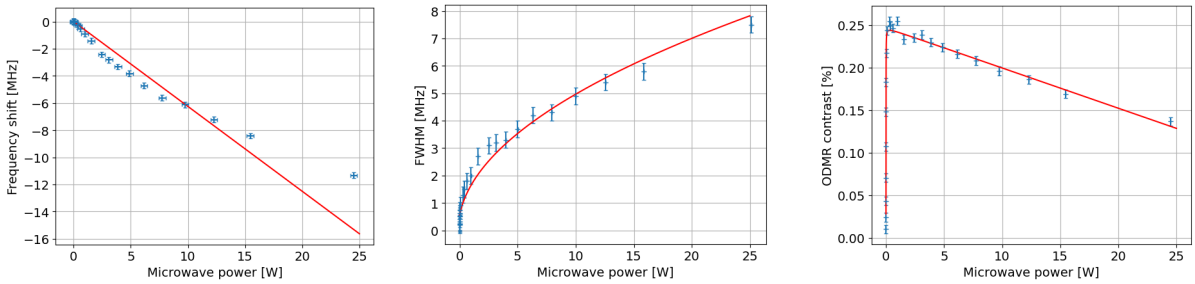

(a) frequency shift as a function of the microwave power with a linear fit (χ^2/ndf = 7.1).

(b) FWHM as a function of the microwave power. The fit (χ^2/ndf = 8.1) is a square root function.

(c) The ODMR contrast in dependence of the microwave power. The fit function (χ^2/ndf = 1.3) is a saturation curve with a linear term for the damping.

Figure 5.20: A deeper analysis of the data presented in Fig. 5.19, where the frequency shift, FWHM, and the ODMR contrast dependence on microwave power are studied.

at 0.2 MHz, which is outside 3σ-range, meaning that the fit does not depict the behavior measured. For the saturation curve the function [42]

$$C(P) = C_{\max} \frac{P/P_S}{1 + P/P_S} + \alpha \cdot P \tag{38}$$

is used, where the first term is the same term used to model the saturation profile for ODMR contrast of PC:PTP in Eq. 33. The linear describes the behavior at high power. The fit parameters are

$$C_{\max} = 0.22(1), \quad P_S = 2.4(4)\,\text{mW}, \quad \alpha = -4.7(4)\,\text{mW}^{-1}. \tag{39}$$

The quality of the fit χ^2/ndf= 1.3 is good, this fit function matches the data well. Both of the equations 38 and 39 originate from the rate equations, thus the P_S should be the same. But, the analysis shows that there is a disagreement with the results, hinting that the rate equations alone do not describe the system at hand.

There are two explanations for this observation. The first one is the **heat**. By increasing the microwave power, the temperature of the antenna increases. The increased temperature causes a change in the population distribution in the triplet state, because the spin-lattice relaxation rates are dependent on the temperature [17]. This would lead to a decrease of the amplitude. The reason for the frequency shift could be as follows: As temperature increases, the amplitude of molecular vibrations (phonons) increases. These vibrations can modulate the distances and angles between the interacting electron spins. Since ZFS parameters, D and E, are highly sensitive to geometry, these thermal vibrations cause fluctuations in the ZFS values, causing a frequency shift. The damping of the ODMR spectrum is caused by the change of the spin-lattice relaxation rates, which are temperature sensitive. The change in the spin-lattice relaxation rates causes a redistribution of the population in the triplet state [17], [13]. The broadening happens because of the known power broadening and increased phonon interaction.

The second possible reason for the observation is the **AC Zeeman effect**. The oscillating microwave field magnetically couples the triplet sublevels. The interaction between the magnetic dipole moment of the system and the time-dependent field gives rise to shifts of the energy levels. Depending on the frequency and polarization of the driving field, these shifts can modify transition frequencies, induce effective couplings between spin states, and generate additional forces in cold-atom [44]. This effect could explain the shift, broadening, damping, and splitting. The broadening and damping happen because of

the coupling to the hyperfine structure. The peak splitting occurs because of different insertion sites of pentacene, each site responds differently to the magnetic field (also observed in the DC Zeeman effect). The AC Zeeman energy shift is given by the so-called Bloch-Siegert shift. Within the rotating-wave approximation (RWA), one retains only the near-resonant co-rotating (slow) term of the drive, which leads to coherent Rabi oscillations and an effective coupling between spin sublevels. However, the oscillatory drive also contains a counter-rotating (fast) component, which is neglected in the RWA. When this counter-rotating term is included perturbatively, it gives rise to an additional energy shift known as the Bloch–Siegert shift. The shift in second-order perturbation theory is given by

$$\delta\omega_{\mathrm{BS}} \approx \frac{\Omega_R^2}{4\omega_0} \propto B_{\mathrm{AC}}^2 \propto P_{\mathrm{in}}, \tag{40}$$

where Ω_R is the Rabi frequency and ω_0 is the resonant frequency of the ODMR transition [45]. The BS-shift is expected to be linear in power. The data of the frequency shift in Fig. 5.20, shows a decreasing trend, however not a linear one. The data is fitted to a linear function with a slope of $m = -0.63(7)\,\mathrm{MHz/W}$. Even with overestimation of the error on the frequency shift, the quality of the fit is still terrible. This suggests that the reason for the shift is not directly the Bloch-Siegert effect.
Both of these effects are very plausible and have the same fingerprint on the ODMR spectrum. To figure out which effect is taking place, the time response of the system is probed. The crystal and the antenna take time to heat up to induce the shift, while the BS shift occurs instantaneously. To measure this, the microwave power is set to a high value of 20 W, and after a long waiting time of 2 minutes, the microwave power is set to 0.2 W, and the amplitude of the ODMR peak is recorded with time. If the peak increases instantly, this would hint at BS-shift, and if the increase is slow in time, then it is thermal. The result of this quick test shows a gradual change of the ODMR peak, meaning the shift and the other observations are originating from the heat coming from the antenna.
Next, the DC Zeeman effect is examined. To achieve that, a commercial magnetic cube is glued to the bottom of a post. The post is attached to the z-axis translation stage as in Fig. 5.2 for holding the wire antenna. The magnet's height is calibrated against field strength so it can be swept in software. The magnetic field strength is measured with Infineon TLE493D-W2B6 MS2GO, a DC magnetic field sensor with an integrated circuit and software to visualize the measured data. The calibration curve is presented in Fig. 5.21, with the calibration function

$$B(\mathrm{z}) = \frac{1.13(15)\,\mathrm{T}\cdot\mathrm{mm}^2}{(\mathrm{z} - 4.4(4)\,\mathrm{mm})^2} - 1.6(4)\,\mathrm{mT}. \tag{41}$$

The fit matches the data well because the χ^2/ndf is close to 1, indicating a good fit result. Then, the magnet with the translation stage is placed above the sample, and for each height, a spectrum with the $|T_x\rangle \leftrightarrow |T_z\rangle$ at 1449.9 MHZ and $|T_y\rangle \leftrightarrow |T_z\rangle$ at 1342.6 MHz transitions is taken. The DC Zeeman effect is observed, and the data are presented in Fig. 5.22. The magnetic field strength in this work is the absolute value of the magnetic field vector. The magnetic field sensor can measure different components of the magnetic field, however, the orientation of the crystal is unknown. This makes it hard to figure out which component is aligned with the molecular axes. For simplicity, the absolute value is taken. The error of the magnetic field strength is estimated to be $\Delta B = 0.2$ mT. As the magnetic field increases, the peaks shift toward higher frequencies with their amplitudes decreasing and broadening, evident from the increase in FWHM, Fig. 5.24. The magnetic field results in population mixing and a diminishing ODMR signal, which nearly vanishes at higher B. The splitting of the resonance occurs because of the lattice sites of p-terphenyl molecules in the ambient conditions [15]. To compute the exact position and FWHM

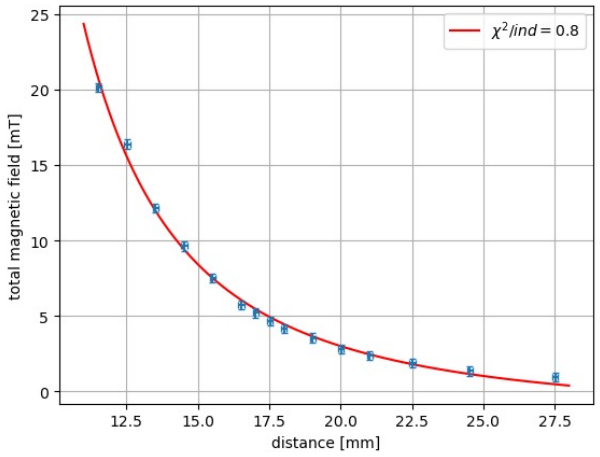

Figure 5.21: The calibration curve of the magnetic field strength as a function of the distance from the sensor.

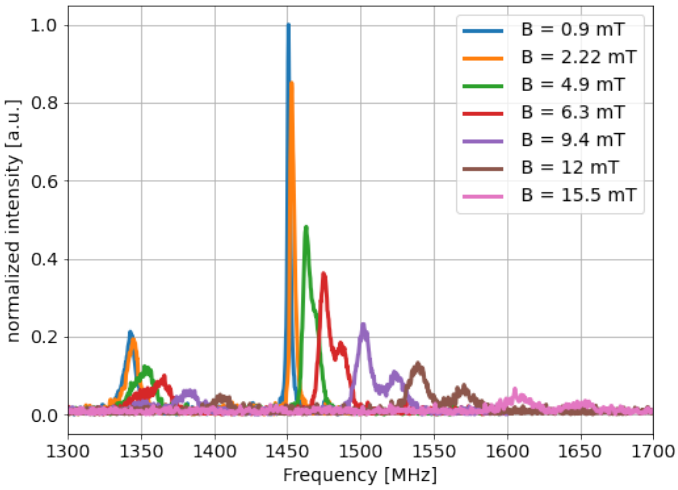

Figure 5.22: The change of the ODMR spectrum depending on the magnetic field strength. There is more data recorded, but for the sake of visibility, they are not included in this figure.

of the peaks, a Lorentzian fit is applied with the function

$$S(f) = A_0 \cdot \frac{(\Gamma_0)^2}{(f - f_0)^2 + (\Gamma_0)^2} + A_1 \cdot \frac{(\Gamma_1)^2}{(f - f_1)^2 + (\Gamma_1)^2} + S_0, \tag{42}$$

Where A is the amplitude, Γ is the FWHM, f_0 is the resonance frequency, and S_0 is the constant noise background. The fits of each peak are shown in the appendix in Chapter IV. The fits start with a great quality (χ^2/ndf = 1.05), but with bigger B fields the quality gets worse (χ^2/ndf = 3.2) as less data points are available in the peaks. The fit parameters can be found in Tab. 1 and Tab. 2 in the appendix.
Now the frequency shift is plotted against the magnetic field strength in Fig. 5.23. The fit function used

for the shift is

$$\Delta f(B) = \alpha \cdot B^2 + \beta \cdot B, \tag{43}$$

This fit function is taken, because for weak fields the shift is described with the second order perturbation

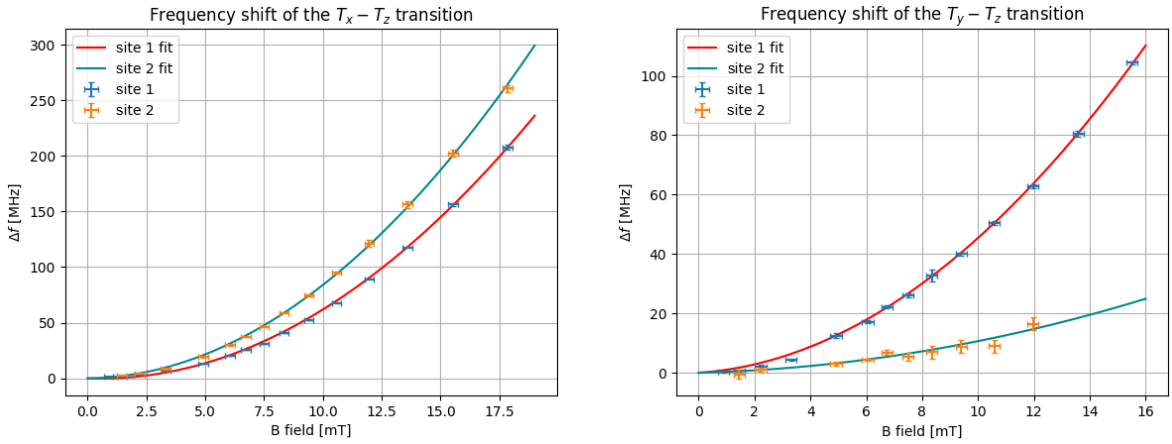

(a) The two sites of the $|T_x\rangle \leftrightarrow |T_z\rangle$ transition.

(b) The two sites of the $|T_y\rangle \leftrightarrow |T_z\rangle$ transition.

Figure 5.23: The Shift and the splitting of the resonances of the dPC:dPTP sample.

theory [15]. The fit parameter are

$$|T_x\rangle \leftrightarrow |T_z\rangle : \quad \text{site 1} : \alpha = 0.693(6)\,\frac{\text{MHz}}{\text{mT}^2}, \quad \beta = -0.73(10)\,\frac{\text{MHz}}{\text{mT}} \tag{44}$$

$$\text{site 2} : \alpha = 0.816(9)\,\frac{\text{MHz}}{\text{mT}^2}, \quad \beta = 0.23(16)\,\frac{\text{MHz}}{\text{mT}} \tag{45}$$

$$|T_y\rangle \leftrightarrow |T_z\rangle : \quad \text{site 1} : \alpha = 0.391(5)\,\frac{\text{MHz}}{\text{mT}^2}, \quad \beta = 0.63(10)\,\frac{\text{MHz}}{\text{mT}} \tag{46}$$

$$\text{site 2} : \alpha = 0.082(9)\,\frac{\text{MHz}}{\text{mT}^2}, \quad \beta = 0.25(11)\,\frac{\text{MHz}}{\text{mT}} \tag{47}$$

All of the fits are very good. This measurement is crucial for computing the DC magnetic field sensitivity of the setup. The FWHM should increase linearly in the weak field regime ($\sim$ 5 mT) [15]. However, the measured FWHM does not always follow a linear trend, see Fig. 5.24. Only site 1 of the $|T_x\rangle \leftrightarrow |T_z\rangle$ transition increases linearly with increasing magnetic field strength. The others behave either chaotically or totally not linear, as for the sites for $|T_y\rangle \leftrightarrow |T_z\rangle$ transition. This observation explains that the magnetic field aligns to the $|T_x\rangle \leftrightarrow |T_z\rangle$. This leads to a linear dependence on the magnetic field. Where for the transition $|T_y\rangle \leftrightarrow |T_z\rangle$, other effects can play a role, because the contribution of the field is weak [46].
A great application of this experiment is a nano-scale magnetic field sensor. This would be implemented in biology, chemistry, and medicine [14]. The equation, to describe the sensitivity of the crystal toward DC magnetic fields using CW ODMR, is

$$\eta_{\text{DC}} = \frac{\sigma\sqrt{\tau}}{\frac{\text{d}S}{\text{d}F} \cdot \gamma_{\text{xz}}}, \tag{48}$$

with the noise floor evaluated far-off resonance σ, the integration time τ, the maximal spectral slope $\frac{\text{d}S}{\text{d}F}$ and the effective gyromagnetic ratio γ_{xz} for the $|T_x\rangle \leftrightarrow |T_z\rangle$ transition [15]. σ is measured by computing

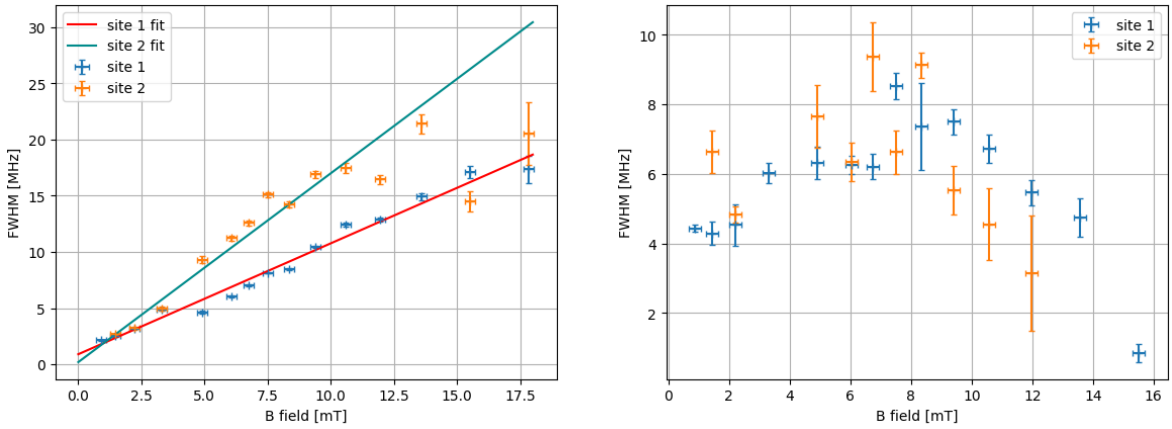

(a) $|T_x\rangle \leftrightarrow |T_z\rangle$ transition.

(b) $|T_y\rangle \leftrightarrow |T_z\rangle$ transition.

Figure 5.24: The FWHM of the resonances as a function of the magnetic field. The FWHM does not look linear for the $|T_y\rangle \leftrightarrow |T_z\rangle$.

the standard deviation for the floor far-off resonance, resulting in $\sigma = 20\,\mu$V. The integration time is set to be 0.15 s on the lock-in amplifier. The data with $B = 1.45$ mT is chosen to calculate the maximal spectral slope and the effective gyromagnetic ratio. The maximal spectral slope $\frac{\mathrm{d}S}{\mathrm{d}F}$ is calculated by computing the first discrete derivative of the spectrum and finding its maximum. The first discrete derivative is

$$S_i'(f) = \frac{S(f_{i+1}) - S(f_i)}{f_{i+1} - f_i}, \tag{49}$$

where $S_i(f)$ is the i-th element of the demodulated signal. The computed maximal spectral slope is $\frac{\mathrm{d}S}{\mathrm{d}F} = 0.0105(1)\,\frac{\mathrm{V}}{\mathrm{MHz}}$. The effective gyromagnetic ratio is defined as

$$\gamma_{\mathrm{xz}} = \frac{\mathrm{d}(\Delta f)}{\mathrm{d}B} \underset{\text{Eq. (43)}}{=} 2 \cdot \alpha \cdot B + \beta \underset{\text{Eq. (44)}}{=} 1.27(29)\,\frac{\mathrm{GHz}}{\mathrm{T}}. \tag{50}$$

The errors are calculated with Gaussian error propagation, see Eq. 35. With these results, the DC sensitivity is

$$\eta_{\mathrm{DC}} = 580(10)\,\frac{\mathrm{nT}}{\sqrt{\mathrm{Hz}}}. \tag{51}$$

This value means, after 1 s averaging (1 Hz bandwidth) the root mean square value of the magnetic field is 580 nT with SNR = 1. For a better SNR, the averaging time can be increased, such that after waiting 100 s, an SNR = 10 is achieved [47].

5.3.1 dPC:dPTP Sublimation Crystal

There are doubts that the ODMR measurement is successful because the crystal is Bridgman grown. To examine this hypothesis, a dPC:dPTP sublimation crystal is placed in the setup, and an ODMR measurement is started. After scanning around the $|T_x\rangle \leftrightarrow |T_z\rangle$ transition, the peak is directly found. The data is presented in Fig. 5.25. The peak, in comparison with the Bridgman crystal, is thinner. The measured linewidth is FWHM = 0.49(1) MHz, whereas for the Bridgman crystal, the linewidth is FWHM = 1.50(5) MHz. This broadening of the linewidth for the Bridgman crystal is credited to the thickness of

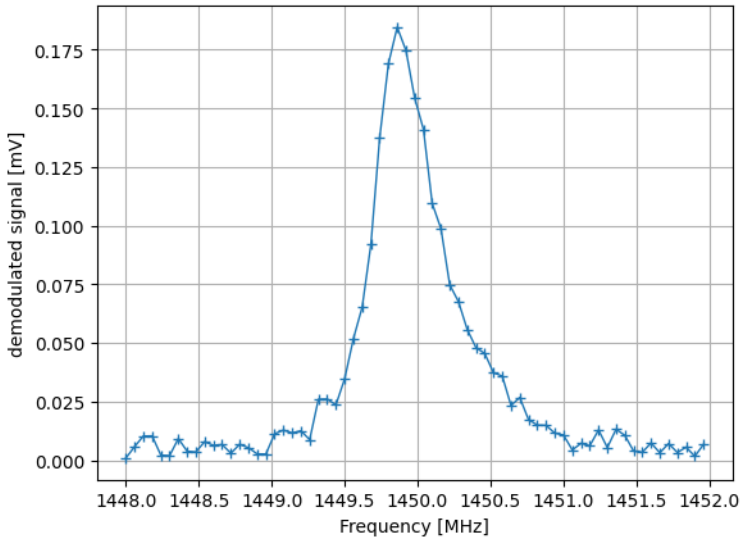

Figure 5.25: The ODMR measurement of the $|T_x\rangle \leftrightarrow |T_z\rangle$ transition with 1 W microwave power.

the sample, which can be approximated to be around 5 mm. The sublimation sample is around 1000 times thinner [35], leading to fewer pentacene molecules being addressed and less inhomogeneous broadening. This sample is only used to cross-check if ODMR is possible with different growth methods. Thus, after confirming ODMR, no further experiments are done on it.

5.3.2 Pulsed ODMR

Now that the resonances have been identified with CW ODMR, pulsed ODMR is expected to work under the similar conditions. However, the implementation of Rabi oscillations has proven to be more technically challenging than anticipated. The lock-in amplifier is no longer part of the setup, and instead, the microwave switch is triggered by the pulse streamer. This means the laser stability is important to ensure consistent measurements, which the current setup lacks. Laser fluctuations of approximately 5% are observed, and another limitation of the current laser configuration is its extinction ratio after the AOM, which is about 1:1000. This means a small amount of light leak through the AOM even when it is off, which is not enough for an accurate measurement of Rabi oscillations.
However, multiple measurements are performed, but no conclusive results are obtained yet. Moving forward, a more stable laser with a higher extinction ratio will be acquired to improve the reliability of the measurements. With this upgrade, the goal is to achieve more consistent and precise results in pulsed ODMR experiments, and further attempts will be made to fully explore the potential of the spin coherence in this system.

6 Conclusion

In this thesis, the preparation of the omega shaped antenna and the optimization of the sample preparation process are carried out to ensure the necessary conditions for accurate measurements. The integration of the lock-in amplifier into the experimental setup is very critical for improving the signal-to-noise ratio, which allowed for the precise detection of the ODMR signal from the sample. The ODMR measurements are successfully performed on both PC:PTP and dPC:dPTP, providing a deeper understanding of the spin properties and behavior of these molecular systems under various experimental conditions.

The saturation behavior of the $|T_x\rangle \leftrightarrow |T_z\rangle$ transition in PC:PTP and dPC:PTP crystals, with increasing optical power, aligns well with theoretical predictions for a two-level transition. However, as the microwave power increases, the theory no longer accurately fits the data, likely due to the effects of heat, which become significant at higher microwave power levels. It is observed that an increase in temperature has a significant influence on spin dynamics and resonance conditions, leading to broader linewidths and reduced coherence. This observation is crucial for understanding the limitations of the system under different experimental conditions, especially in the context of maintaining long-lived quantum states. Additionally, DC sensitivity of $580(10)\ \mathrm{nT}\sqrt{\mathrm{Hz}}^{-1}$ is calculated after measuring the DC Zeeman effect, confirming the system's high sensitivity and stability in detecting changes in spin populations, further validating the robustness of the experimental setup.

The perylene sample presents more complexity than initially anticipated. Difficulties in achieving consistent resonance and reliable ODMR signals are encountered, suggesting that further work is required to optimize the sample and improve its performance. The challenges, faced with the perylene sample, highlight the need for additional investigation into the material's properties, including potential refinements in sample preparation techniques, different host matrix combinations, and deeper understanding of its spin properties. Similarly, pulsed ODMR experiments remain an area for significant development, with further refinements needed in both the experimental techniques and the setup.

In conclusion, while the work presented in this thesis provides a strong foundation for the use of molecular systems in quantum technologies, particularly for quantum sensing and spin-based applications. It has become evident that additional research and development are required. The optimization of both molecular samples, such as perylene, and experimental techniques, such as pulsed ODMR, will be crucial in realizing the full potential of these systems.

Appendix

I Different wire antenna configurations

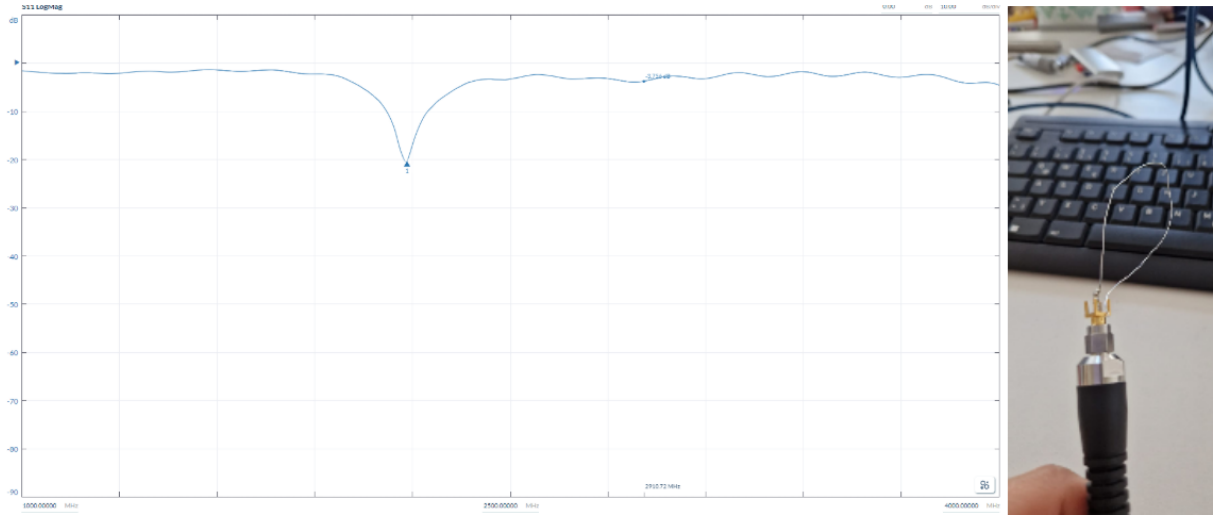

Figure 6.1: One Loop connecting to ground.

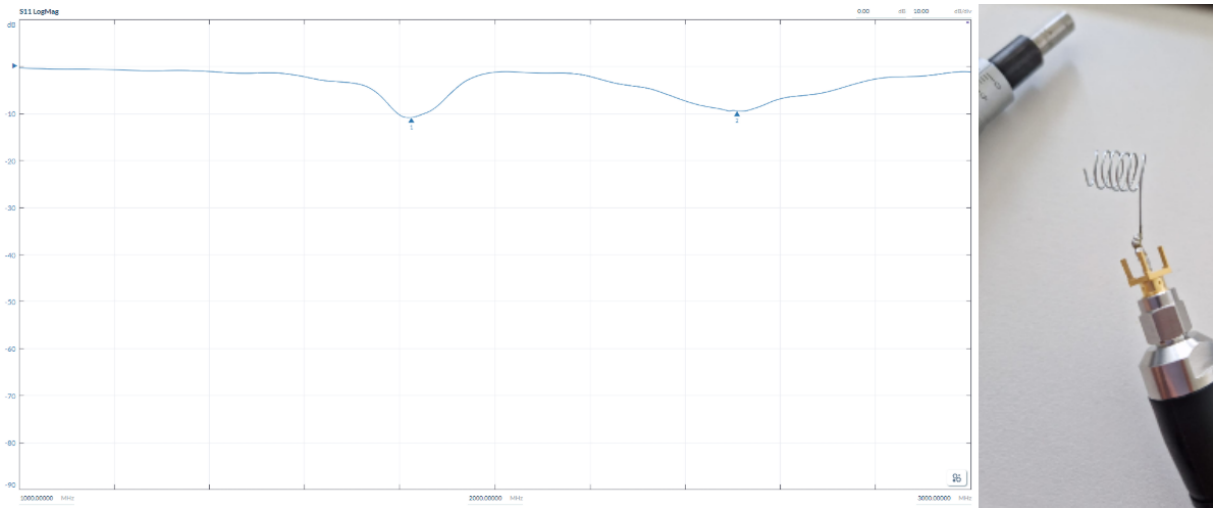

Figure 6.2: Several open Loops.

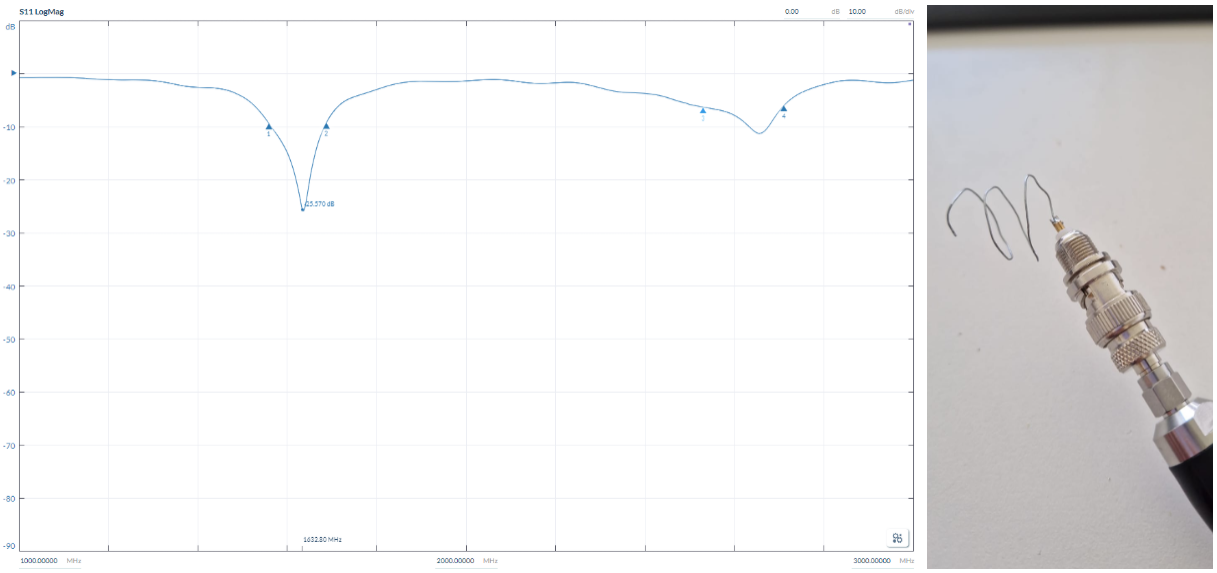

Figure 6.3: Two big Loops.

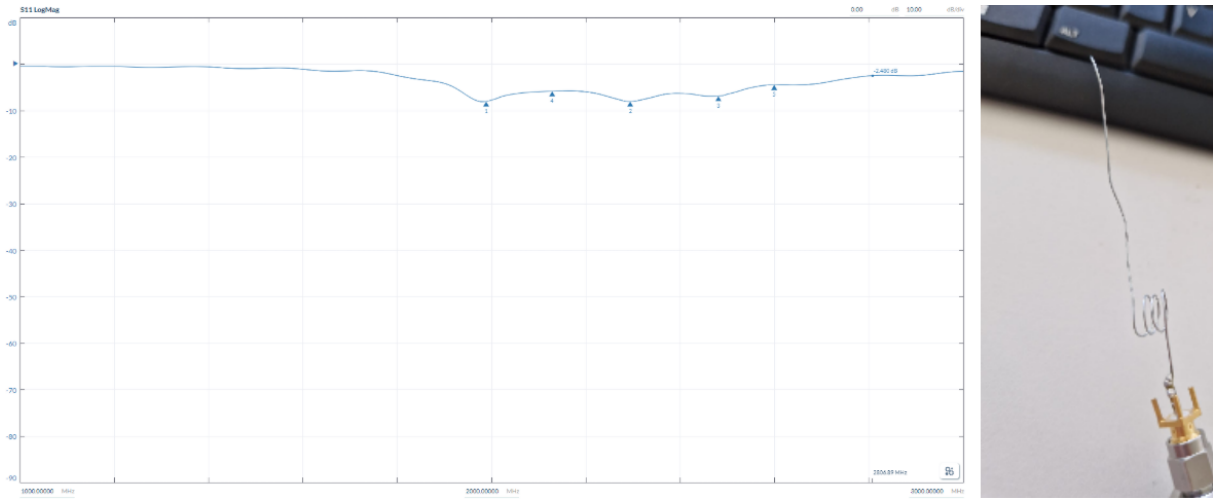

Figure 6.4: Three small Loops and a dipole part at the end.

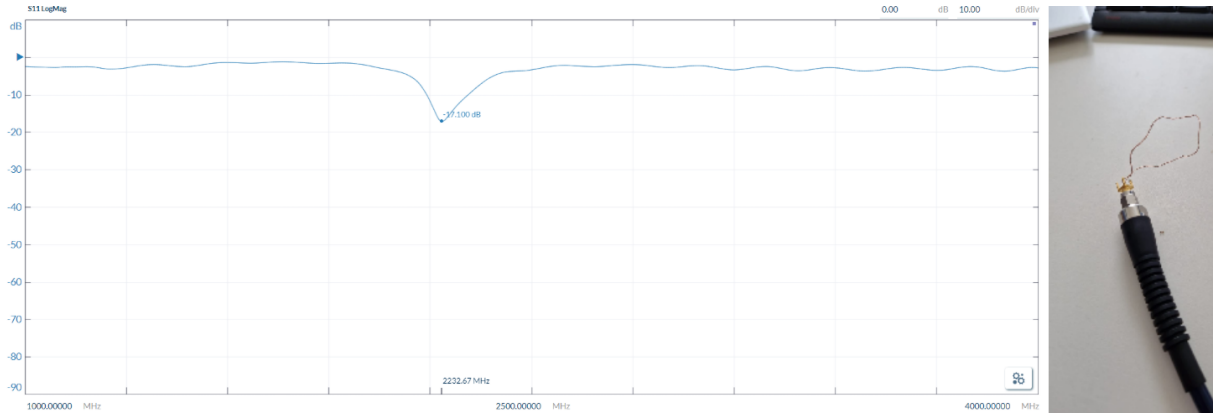

Figure 6.5: One loop connected to the ground with a copper wire of length l_1.

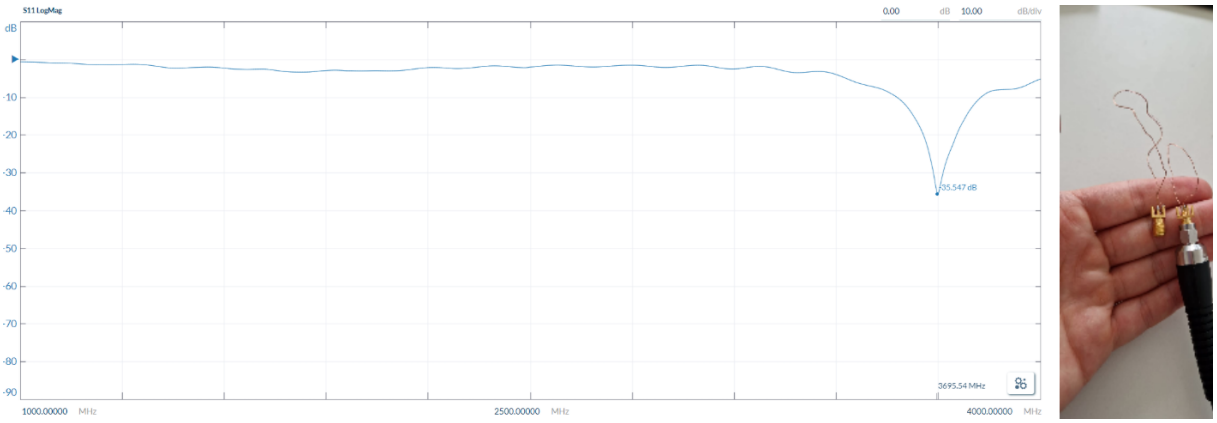

Figure 6.6: One loop connected to the ground with a copper wire of length l_2, where $l_1 > l_2$.

II Different antenna parameters

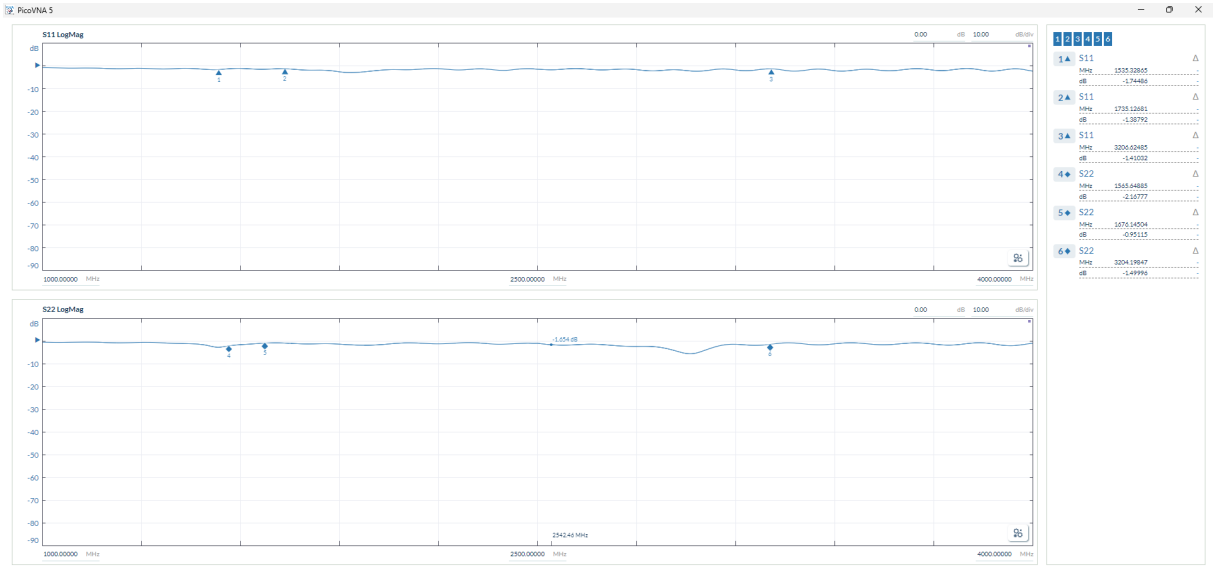

Figure 6.7: The PCB without antenna connected.

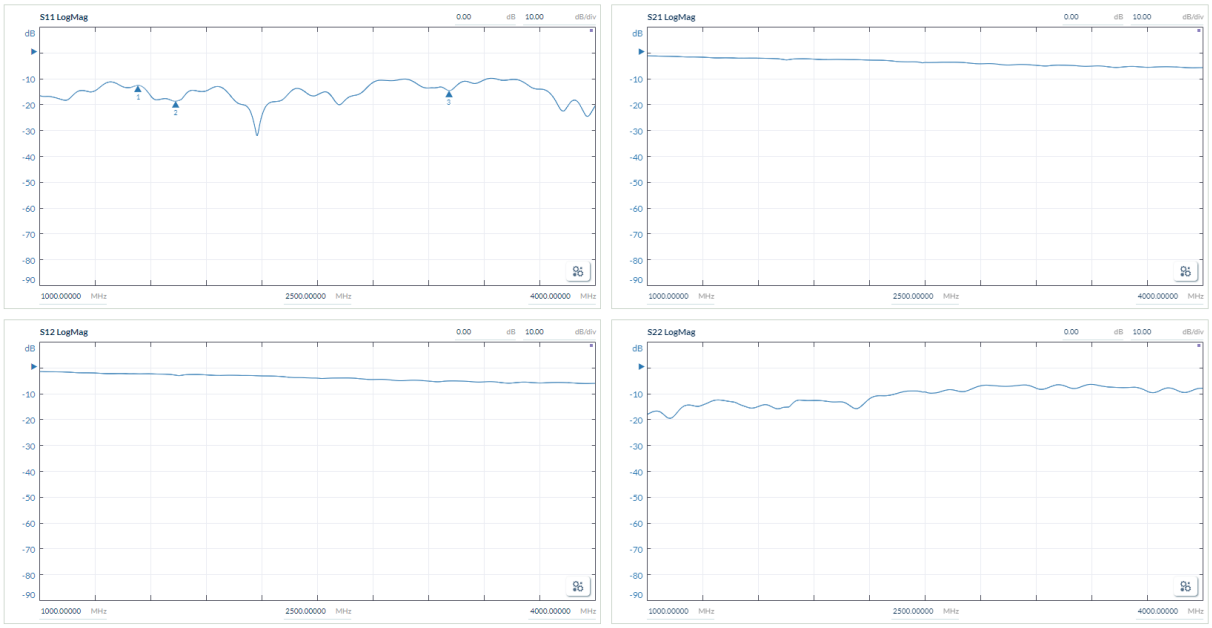

Figure 6.8: For 7 μm gap width and 300 μm inner diameter.

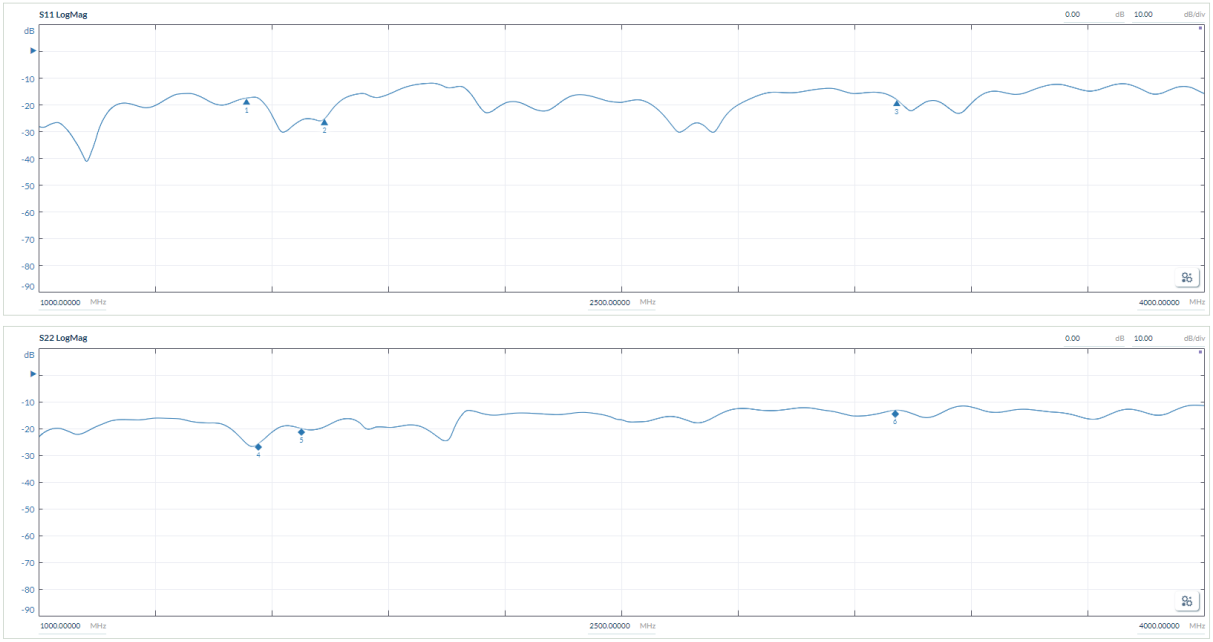

Figure 6.9: For 17 μm gap width and 300 μm inner diameter.

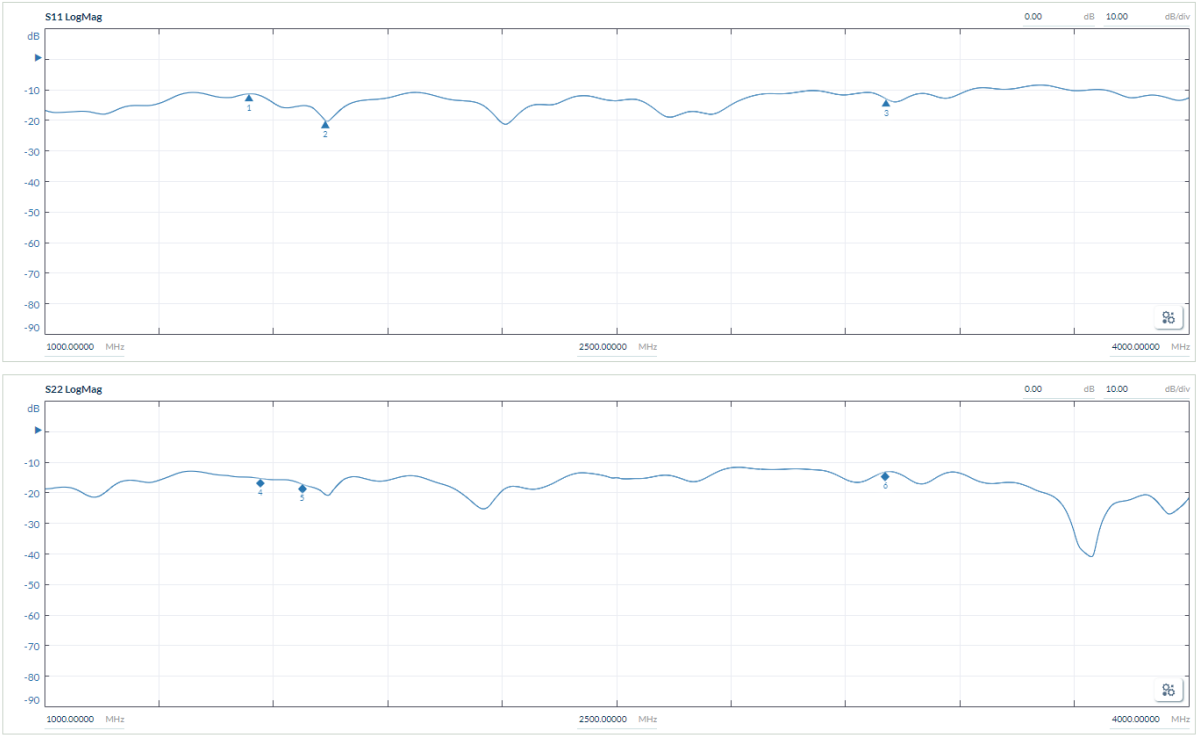

Figure 6.10: For 10 μm gap width and 550 μm inner diameter.

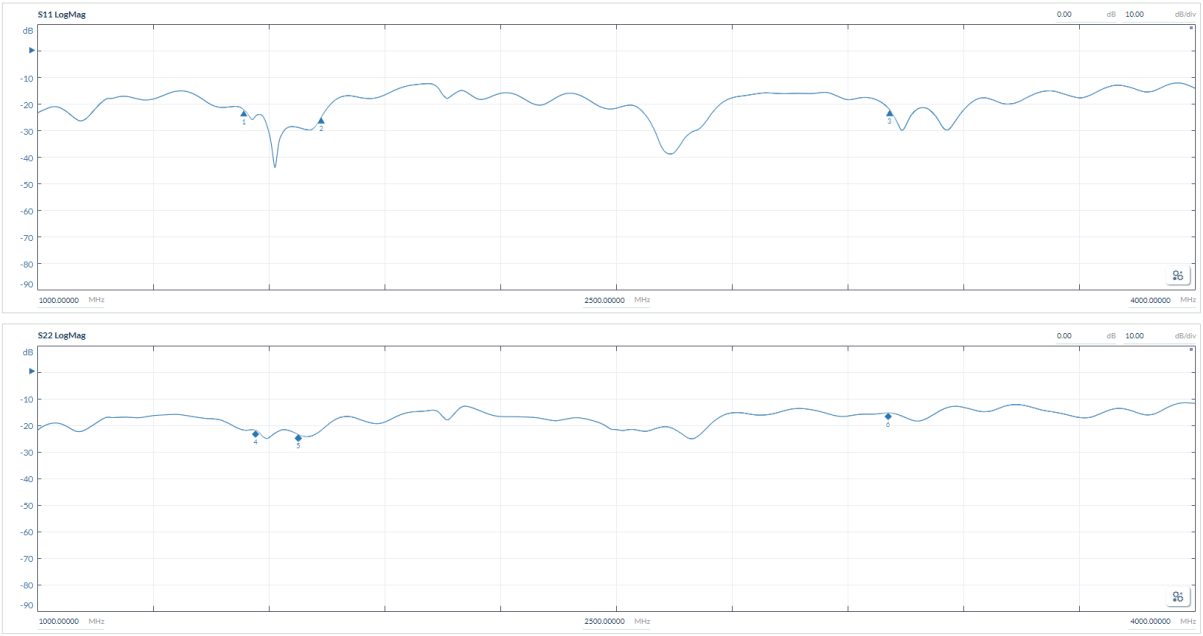

Figure 6.11: For 10 μm gap width and 500 μm inner diameter.

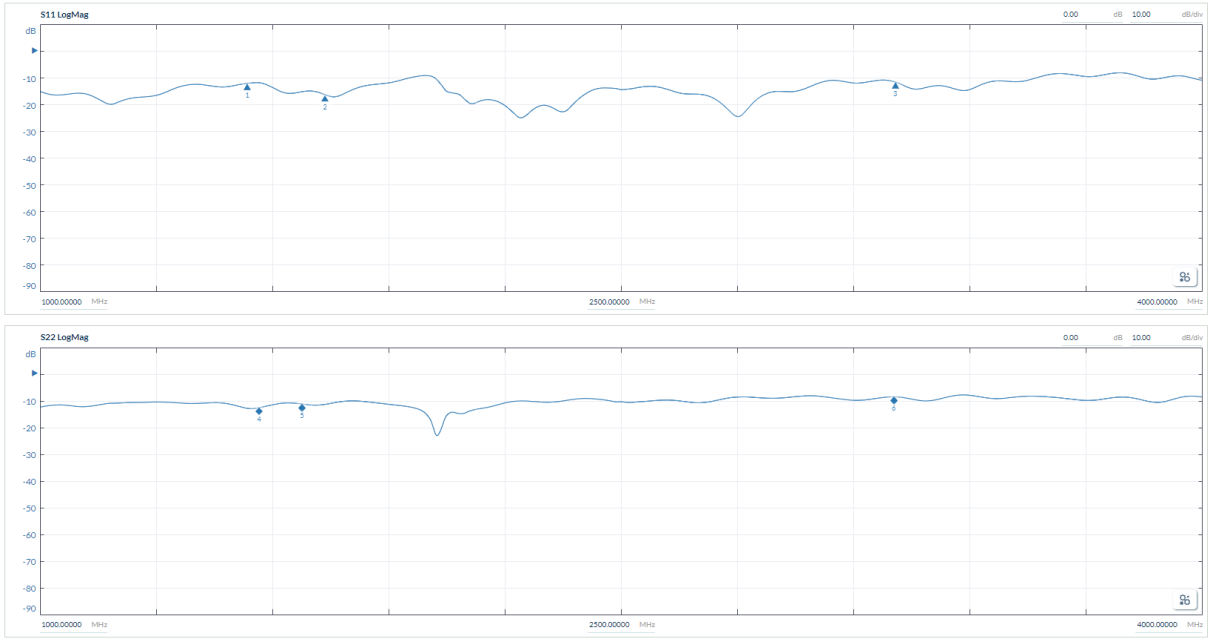

Figure 6.12: For 10 μm gap width and 700 μm inner diameter.

III Temperature sensitive fluorescence device

Due to complex circumstances, a 10.3 x 10.3 mm^2 silicon wafer was used as a platform to elevate the antenna to the correct height for the electrical connection, as shown in Fig. 6.13. When an ODMR

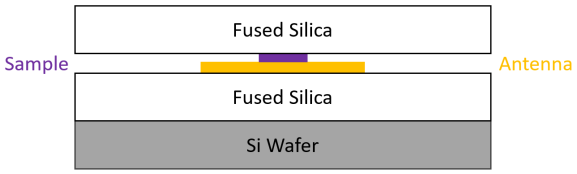

Figure 6.13: The structure that lead to a temperature sensitive fluorescence.

experiment on this sample is initiated (without the lock-in amplifier, only with APD and NIDAQ), the fluorescence change quite a lot independently of the microwave signal. After further examination, a strong correlation between the temperature ~30 cm above the sample and the fluorescence at the APD is observed, see Fig. 6.14. The reason of this observation is the silicon wafer below. The wafer is polished

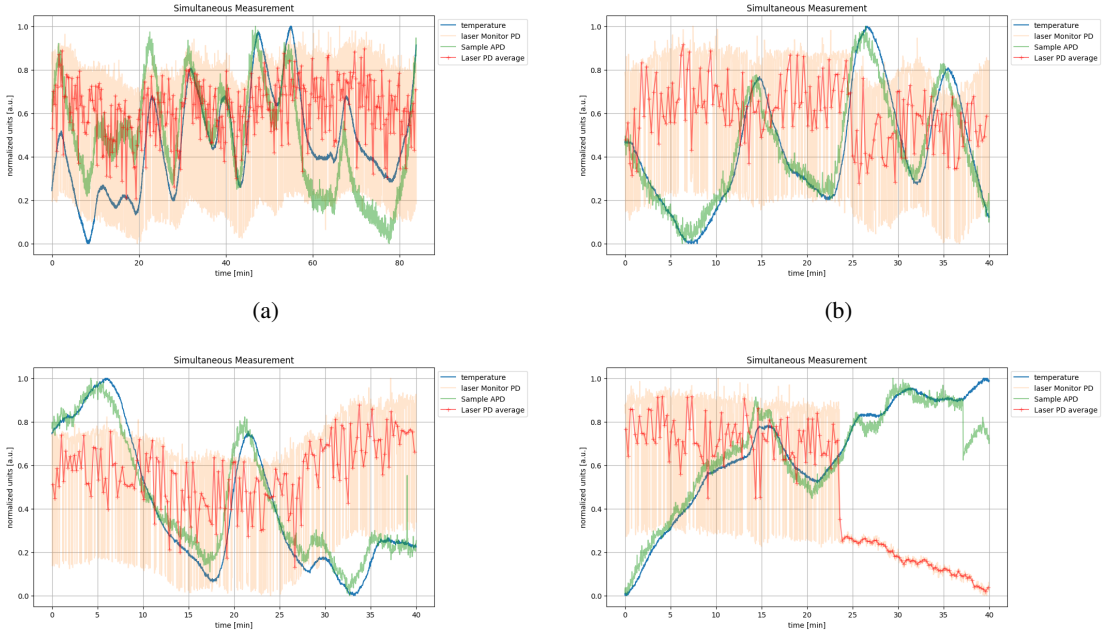

Figure 6.14: The data measured of correlation between the temperature and fluorescence of the sample. The data is normalized such that the minimum is 0 and the maximum is 1, by following relation: $x_{\text{norm}} = \frac{x - \min(x)}{\max(x) - \min(x)}$.

and highly reflective. The silicon wafer and the fused silica make a standing optical wave, similar to a cavity, that excited the sample. But, when the temperature changes, thermal expansion takes place, leading to a change in the distance between the reflective layers. Thus, this induces a change in the fluorescence that can be traced back to the temperature fluctuations. If this device calibrated correctly it can be used as nanoscale temperature sensor that can be applied in medicine and biology.

IV Fits for the Zeeman effect

Table 1: The fit data for the $|T_x\rangle \leftrightarrow |T_z\rangle$ resonance shift due to magnetic field.

B [mT]	A_0 [mV]	f_0 [MHz]	$\Gamma_0/2$ [MHz]	A_1 [mV]	f_1 [MHz]	$\Gamma_1/2$ [MHz]	S_0 [mV]
0.89(20)	12.5(1)	1451.07(1)	1.07(2)	-	-	-	0.4(3)
1.5(2)	8.1(7)	1451.35(2)	0.65(5)	7.2(6)	1452.43(9)	1.33(5)	0.02(3)
2.2(2)	8.4(7)	1452.79(5)	0.94(8)	5.7(6)	1454.37(16)	1.60(12)	0.04(4)
3.3(2)	6.8(4)	1455.84(5)	1.25(10)	4.9(4)	1458.33(20)	2.48(18)	0.15(5)
4.9(2)	5.5(2)	1462.92(5)	2.32(10)	3.2(1)	1468.85(21)	4.65(30)	0.36(5)
6.1(2)	5.2(1)	1470.03(4)	3.03(8)	2.62(5)	1479.69(14)	5.61(27)	0.37(4)
6.7(2)	4.63(5)	1475.16(4)	3.53(8)	2.25(4)	1487.28(13)	6.29(25)	0.33(3)
7.5(2)	4.34(3)	1481.10(3)	4.07(6)	2.19(3)	1496.17(9)	7.55(20)	0.53(4)
8.4(2)	3.69(3)	1490.38(4)	4.23(7)	1.57(3)	1508.64(13)	7.11(26)	0.16(2)
9.4(2)	3.00(3)	1502.09(5)	5.22(9)	1.34(3)	1524.82(14)	8.46(30)	0.20(2)
10.6(2)	2.38(3)	1517.63(7)	6.21(16)	1.09(3)	1545.11(19)	8.74(44)	0.15(3)
12.0(2)	1.60(2)	1539.07(9)	6.43(16)	0.71(2)	1571.09(23)	8.23(42)	0.02(1)
13.6(2)	1.06(2)	1567.30(15)	7.46(28)	0.44(2)	1606.36(44)	10.73(85)	0.04(1)
15.5(2)	5.40(2)	1606.03(32)	8.55(54)	0.30(2)	1652.25(55)	7.24(90)	0.09(1)
17.9(2)	2.42(2)	1657.35(73)	8.68(123)	0.12(2)	1710.59(159)	10.27(277)	0.105(8)

Table 2: The fit data for the $|T_y\rangle \leftrightarrow |T_z\rangle$ resonance shift due to magnetic field.

B [mT]	A_0 [mV]	f_0 [MHz]	$\Gamma_0/2$ [MHz]	A_1 [mV]	f_1 [MHz]	$\Gamma_1/2$ [MHz]	S_0 [mV]
0.89(20)	2.61(3)	1342.89(4)	4.43(10)	-	-	-	−0.01(2)
1.5(2)	1.6(2)	1344.07(11)	2.72(33)	1.24(26)	1342.16(42)	6.63(61)	−0.04(3)
2.2(2)	0.9(3)	1346.16(20)	2.17(60)	1.1(3)	1343.67(44)	4.82(23)	0.03(3)
3.3(2)	2.36(9)	1347.07(10)	6.22(29)	-	-	-	−0.25(14)
4.9(2)	1.4(1)	1355.00(28)	6.31(47)	0.77(8)	1345.68(72)	7.65(90)	−0.18(5)
6.1(2)	1.13(2)	1359.76(16)	6.25(26)	0.52(2)	1347.08(35)	6.34(55)	0.02(1)
6.7(2)	1.01(3)	1364.80(20)	6.20(36)	0.51(2)	1349.44(62)	9.37(99)	−0.01(1)
7.5(2)	0.95(2)	1368.69(18)	8.52(39)	0.45(2)	1347.98(34)	6.62(63)	−0.04(2)
8.4(2)	0.25(2)	1349.54(69)	9.1(12)	0.76(2)	1375.43(20)	7.35(37)	0.06(1)
9.4(2)	0.68(2)	1382.57(19)	7.49(36)	0.27(2)	1351.43(40)	5.52(70)	0.07(1)
10.6(2)	0.52(2)	1392.97(24)	6.72(41)	0.16(2)	1351.52(64)	4.5(10)	0.10(1)
12.0(2)	0.45(2)	1405.47(23)	5.46(37)	0.07(2)	1359.1(11)	3.2(17)	0.11(1)
13.6(2)	0.3(1)	1423.22(34)	4.75(55)	-	-	-	0.11(1)
15.5(2)	0.25(5)	1446.99(18)	0.84(25)	-	-	-	0.12(1)
17.9(2)	-	-	-	-	-	-	-

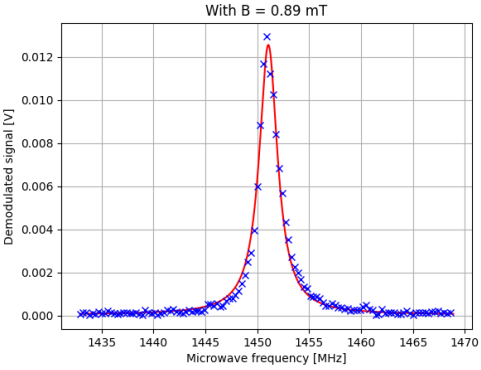
With B = 0.89 mT
Demodulated signal [V]
Microwave frequency [MHz]

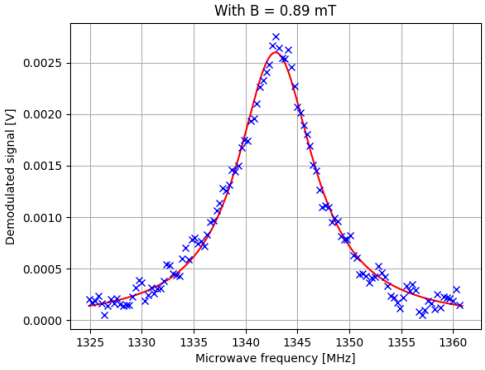
With B = 0.89 mT
Demodulated signal [V]
Microwave frequency [MHz]

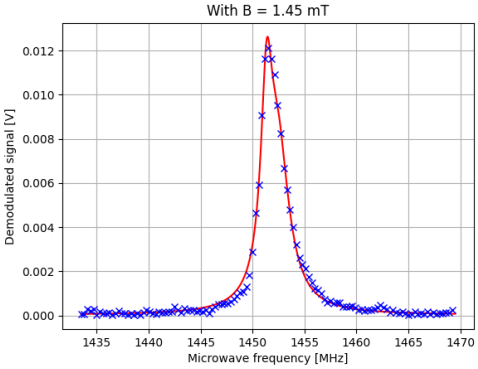
With B = 1.45 mT
Demodulated signal [V]
Microwave frequency [MHz]

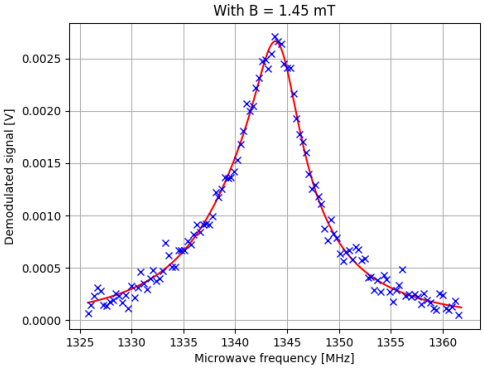
With B = 1.45 mT
Demodulated signal [V]
Microwave frequency [MHz]

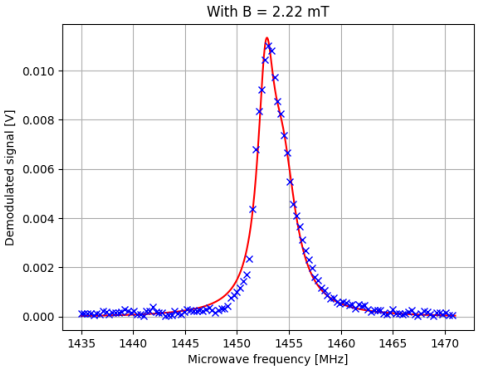
With B = 2.22 mT
Demodulated signal [V]
Microwave frequency [MHz]

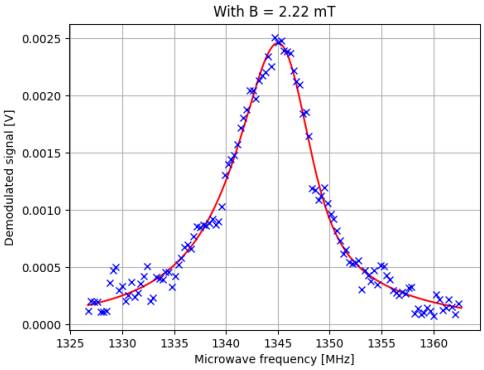
With B = 2.22 mT
Demodulated signal [V]
Microwave frequency [MHz]

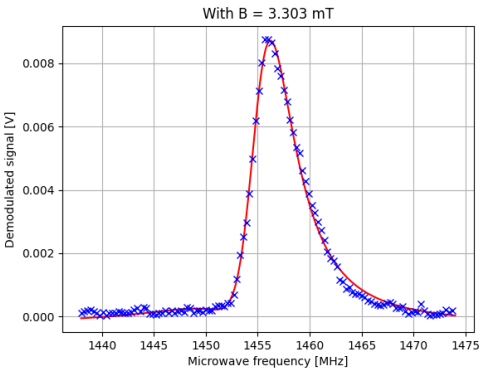
With B = 3.303 mT
Demodulated signal [V]
Microwave frequency [MHz]

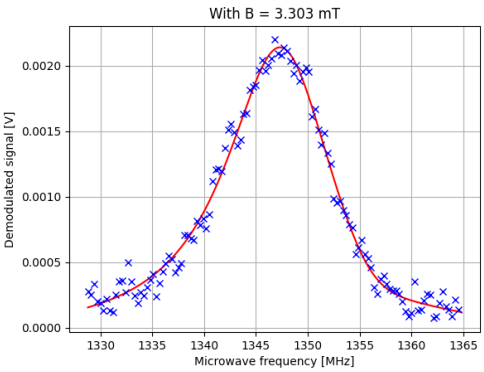
With B = 3.303 mT
Demodulated signal [V]
Microwave frequency [MHz]

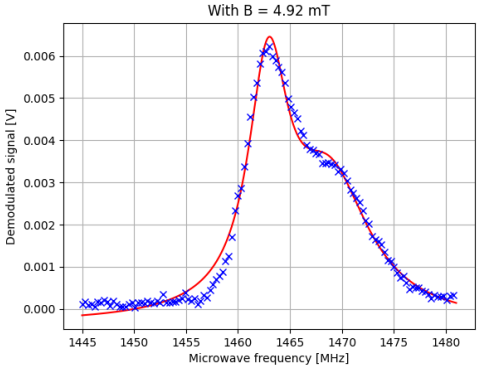
With B = 4.92 mT
Demodulated signal [V]
Microwave frequency [MHz]

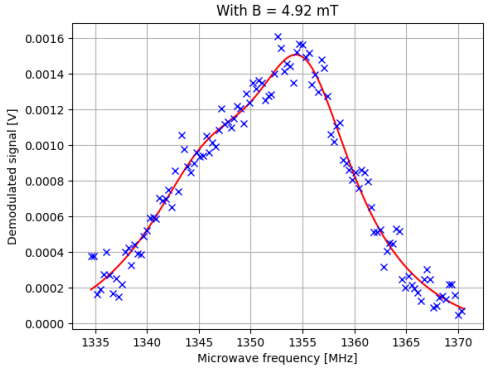
With B = 4.92 mT
Demodulated signal [V]
Microwave frequency [MHz]

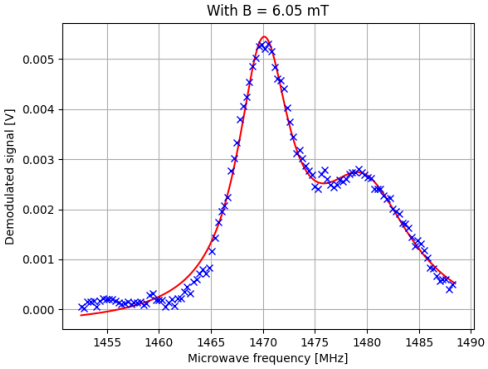
With B = 6.05 mT
Demodulated signal [V]
Microwave frequency [MHz]

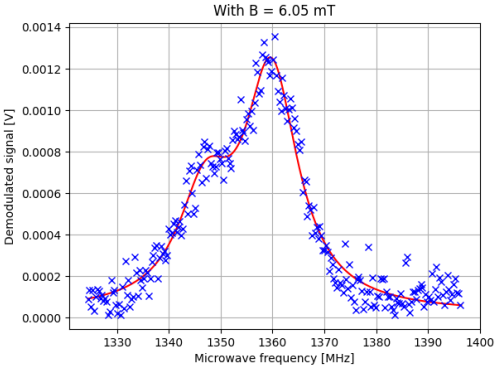
With B = 6.05 mT
Demodulated signal [V]
Microwave frequency [MHz]

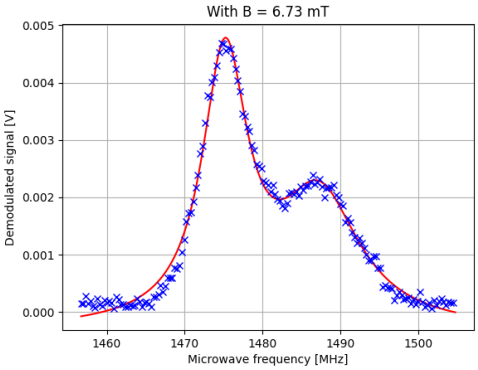
With B = 6.73 mT
Demodulated signal [V]
Microwave frequency [MHz]

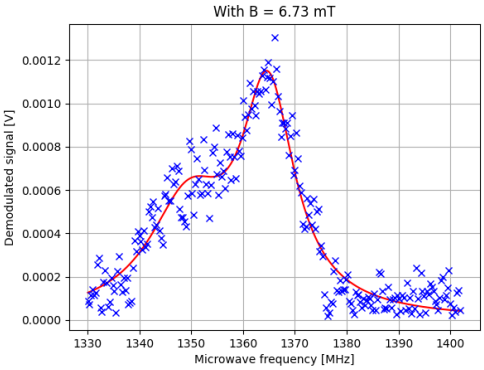
With B = 6.73 mT
Demodulated signal [V]
Microwave frequency [MHz]

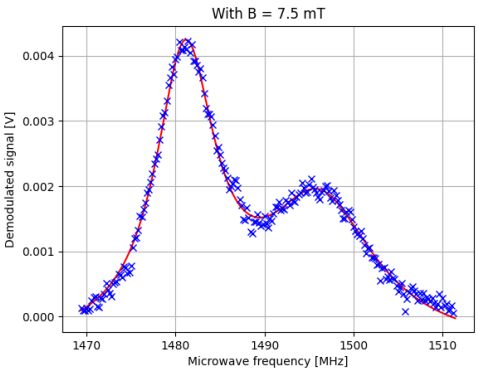
With B = 7.5 mT
Demodulated signal [V]
Microwave frequency [MHz]

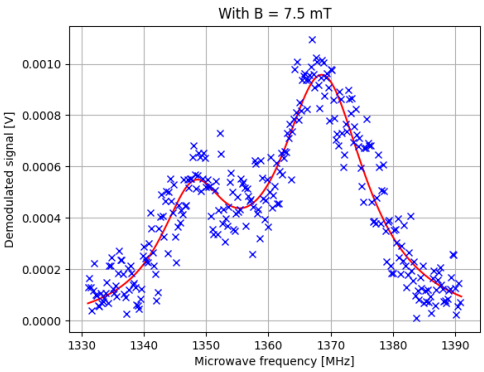
With B = 7.5 mT
Demodulated signal [V]
Microwave frequency [MHz]

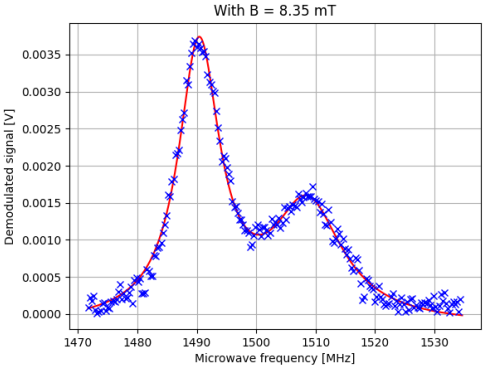
With B = 8.35 mT
Demodulated signal [V]
Microwave frequency [MHz]

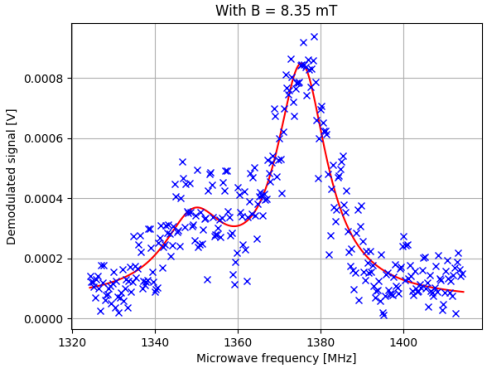
With B = 8.35 mT
Demodulated signal [V]
Microwave frequency [MHz]

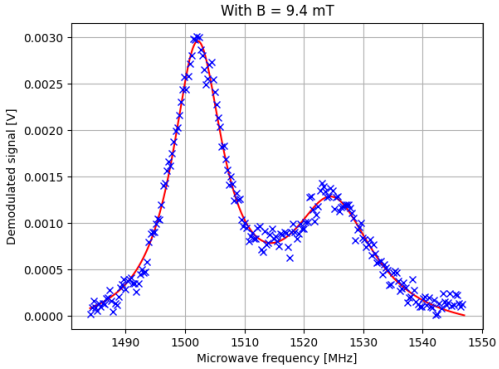
With B = 9.4 mT
Demodulated signal [V]
Microwave frequency [MHz]

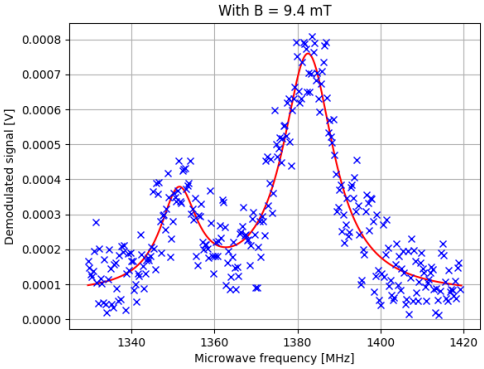
With B = 9.4 mT
Demodulated signal [V]
Microwave frequency [MHz]

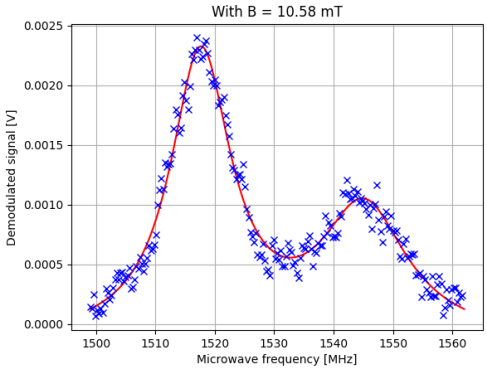
With B = 10.58 mT
Demodulated signal [V]
Microwave frequency [MHz]

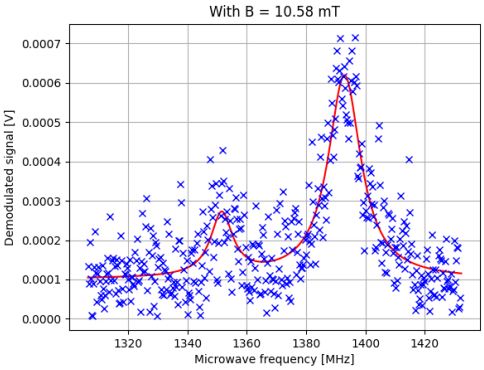
With B = 10.58 mT
Demodulated signal [V]
Microwave frequency [MHz]

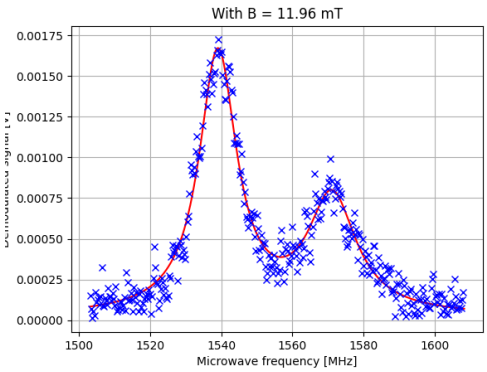
With B = 11.96 mT
Microwave frequency [MHz]

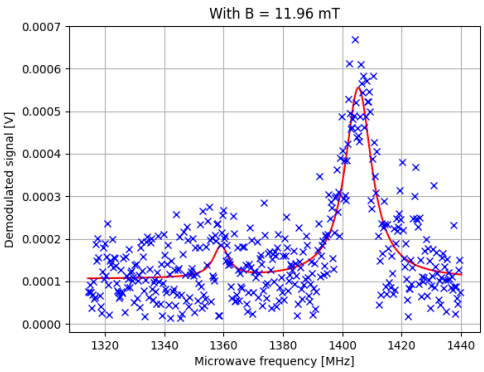
With B = 11.96 mT
Demodulated signal [V]
Microwave frequency [MHz]

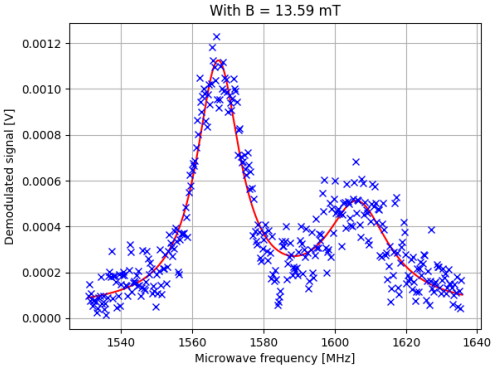
With B = 13.59 mT
Demodulated signal [V]
Microwave frequency [MHz]

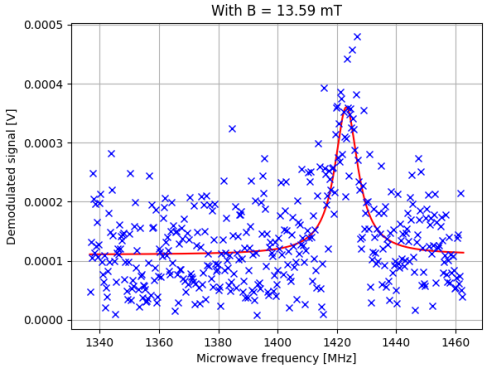
With B = 13.59 mT
Demodulated signal [V]
Microwave frequency [MHz]

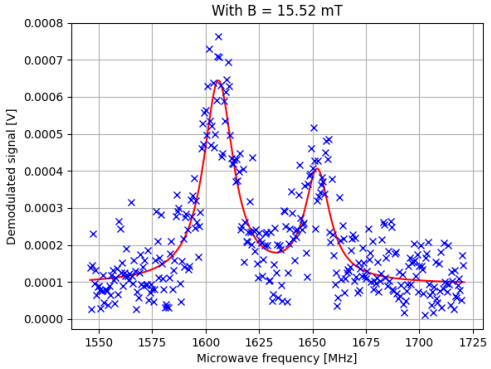
With B = 15.52 mT
Demodulated signal [V]
Microwave frequency [MHz]

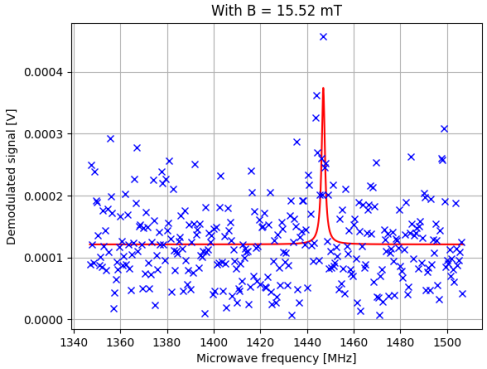
With B = 15.52 mT
Demodulated signal [V]
Microwave frequency [MHz]

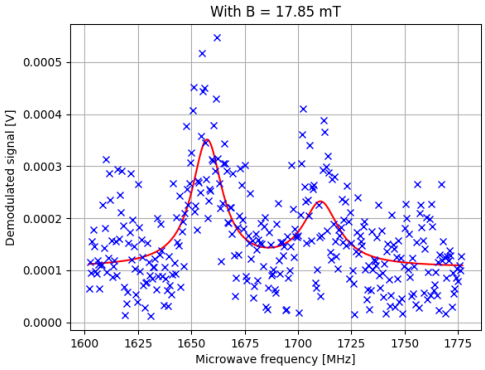
With B = 17.85 mT
Demodulated signal [V]
Microwave frequency [MHz]

References

[1] P. W. Shor, *Polynomial-Time Algorithms for Prime Factorization and Discrete Logarithms on a Quantum Computer*. SIAM J.Sci.Statist.Comput. 26 1484, 1997.

[2] N. Sekiguchi *et al.*, *Diamond quantum magnetometer with dc sensitivity of < 10 pT $Hz^{-1/2}$ toward measurement of biomagnetic field*. Phys. Rev. Applied 21, 064010, 2024.

[3] I. M. Georgescu *et al.*, *Quantum simulation*. Rev. Mod. Phys. 86, 153, 2014.

[4] D. Lachance-Quirion *et al.*, *Hybrid quantum systems based on magnonics*. Appl. Phys. Express 12 070101, 2019.

[5] L. Henriet *et al.*, *Quantum computing with neutral atoms*. Quantum 4, 327, 2020.

[6] H. Haeffner *et al.*, *Quantum computing with trapped ions*. Phys. Rep. 469, 155-203, 2008.

[7] M. Kjaergaard *et al.*, *Superconducting Qubits: Current State of Play*. Annual Reviews of Condensed Matter Physics 11, 369-395, 2020.

[8] H. Wu, *Room-Temperature Quantum Devices Based on Pentacene's Photo-Excited Triplet State in p-Terphenyl*. Imperial College London Department of Materials, 2020.

[9] B. Gurlek *et al.*, *Small but large: Single organic molecules as hybrid platforms for quantum technologies*. Phys. Rev. Research 7, 021001, 2025.

[10] A. L. Kwiram, *Optical detection of paramagnetic resonance in phosphorescent triplet states*. Chem. Phys. Letters 1(7): 272-275, 1967. DOI: doi.org/10.1016/0009-2614(67)80017-4.

[11] J. Schmidt *et al.*, *Optical detection of zero-field transitions in phosphorescent triplet states*. Chem. Phys. Letters 2(8): 640-642, 1968. DOI: doi.org/10.1016/0009-2614(63)80039-1.

[12] J. Wrachtrup *et al.*, *Optical detection of magnetic resonance in a single molecule*. Nature 363, 244–245, 1993.

[13] J. Köhler, *Magnetic resonance of a single molecular spin*. Physics Reports 310 261-339, 1999.

[14] A. Mena *et al.*, *Room-Temperature Optically Detected Coherent Control of Molecular Spins*. Phys. Rev. Lett. 133, 120801, 2024.

[15] H. Singh *et al.*, *Room-temperature quantum sensing with photoexcited triplet electrons in organic crystals*. Phys. Rev. Research 7, 013192, 2025. DOI: https://doi.org/10.1103/PhysRevResearch.7.013192.

[16] J. L. Skinner, *Theory of Pure Dephasing in Crystals*. Annu. Rev. Phys. Chem. 39, 463, 1988.

[17] M. Schwoerer *et al.*, *Organic Molecular Solids*. Wiley, 2007, ISBN: 978-3-527-40540-4.

[18] B. Valeur, *Molecular Fluorescence Principles and Applications*. Wiley, 2001, ISBN: 3-527-29919-X.

[19] R. Brown *et al.*, *Kinetics of optically detected magnetic resonance of single molecules*. J. Chem. Phys. 100, 7182–7191, 1994.

[20] P. Walla *et al.*, *Perylene in biphenyl and anthracene crystals: An example of the influence of the host on single-molecule signals*. Chem. Phys. 233(1):117-125, 1998. DOI: doi.org/10.1016/S0301-0104(98)00159-1.

[21] T. Lin, *Novel Pulsed Electron Paramagnetic Resonance Techniques for the Studies of Structure and Dynamics of Photo-excited Triplet State of Organic Molecules: A Professional Journey*. J. Chin. Chem. Soc., 65 (2):163–188, 2018.

[22] M. Oxborrow *et al.*, *Room-temperature solid-state maser*. Nature, 488(7411):353, 2012.

[23] M. Iinuma *et al.*, *Proton polarization with p-terphenyl crystal by integrated solid effect on photoexcited triplet state*. J. Magn. Reson., 175(2):235–241, 2005.

[24] J. D. Breeze *et al.*, *Room temperature cavity quantum electrodynamics with strongly coupled Dicke states triplet state*. npj Quantum Inf., 3(1):1–5, 2017.

[25] W. van Dorp *et al.*, *The lowest triplet state of free base porphin*. Molecular Physics, 30(6), 1701–1721, 2006. DOI: doi.org/10.1080/00268977500103231.

[26] A. C. J. Brouwer *et al.*, ^{13}C *isotope effects for pentacene in p-terphenyl: High-resolution spectroscopy and single-spin detection*. J. Chem. Phys. 105, 2212–2222, 1996.

[27] A. Dréau1 *et al.*, *Avoiding power broadening in optically detected magnetic resonance of single NV defects for enhanced dc magnetic field sensitivity*. Phys. Rev. B 84, 195204, 2011.

[28] C. A. Balanis, *Antenna Theory: Analysis and Design*. Wiley, 1997, ISBN: 0-471-59268-4.

[29] D. M. Pozar, *Microwave Engineering*. Wiley, 2012, ISBN: 978-0-470-63155-3.

[30] O. R. Opaluch *et al.*, *Optimized Planar Microwave Antenna for Nitrogen Vacancy Center Based Sensing Applications*. Nanomaterials, 11(8), 2108. DOI: https://doi.org/10.3390/nano11082108.

[31] C. Koch *et al.*, *Photolithography: Basics of microstructuring*. MicroChmeicals, 2020.

[32] UC Davis CNM2. "Lift-off processes with photoresists." (2014), [Online]. Available: https://research.engineering.ucdavis.edu/cnm2/wp-content/uploads/sites/11/2014/07/lift_off_photoresist.pdf (visited on 08/09/2025).

[33] NIOSH. "P-terphenyl." (2019), [Online]. Available: https://www.cdc.gov/niosh/npg/npgd0593.html (visited on 08/19/2025).

[34] M. Schwoerer *et al.*, *Crystals: Growth, Properties and Applications*. Springer, 1980, ISBN: 978-3-642-67766-3.

[35] Falk Maniera Siebert. "Bachelor thesis: Sample preparation for quantum optical experiments." (2025).

[36] Zurich Instruments AG. "Mfli user manual: Signal processing basics." (2024), [Online]. Available: https://docs.zhinst.com/mfli_user_manual/signal_processing_basics.html (visited on 08/19/2025).

[37] Red Pitaya. "Stemlab 125-14." (2025), [Online]. Available: https://redpitaya.com/stemlab-125-14/ (visited on 08/24/2025).

[38] NI. "Usb-6003." (2025), [Online]. Available: https://www.ni.com/de-de/shop/model/usb-6003.html (visited on 08/24/2025).

[39] Teledyne Vision Solutions. "Prime bsi." (2025), [Online]. Available: https://www.teledynevisionsolutions.com/de-de/products/prime-bsi/?vertical=tvs-photometrics&segment=tvs (visited on 08/24/2025).

[40] L. Sellies *et al.*, *Single-molecule electron spin resonance by means of atomic force microscopy*. Nature volume 624, pages 64–68, 2023.

[41] P. F. Bernath, *Spectra of Atoms and Molecules*. Oxford University Press, 1995, ISBN: 0-19-507598-6.

[42] A. J. Maser, *Few-photon coherent nonlinear optics with a single molecule*. Erlangen, FAU University Press, 2017.

[43] A. Singh *et al.*, *Error Propagation*. Reson 26, 853–861, 2021.

[44] C. T. Fancher *et al.*, *Microwave ac Zeeman force for ultracold atoms*. Phys. Rev. A 97, 043430, 2018.

[45] Y. Yan *et al.*, *Bloch-Siegert shift of the Rabi model*. Phys. Rev. A 91, 053834, 2015.

[46] L. Rondin *et al.*, *Magnetometry with nitrogen-vacancy defects in diamond*. Rep. Prog. Phys. 77 056503, 2014.

[47] J. M. TAYLOR *et al.*, *High-sensitivity diamond magnetometer with nanoscale resolution*. Nature Physics volume 4, pages 810–816, 2008. DOI: doi:10.1038/nphys1075.